

https://dspace.org/

Optical spectroscopy studies of ion bombarded gallium arsenide and vanadium carbide thin films

Jakata, Kudakwashe

2018

https://hdl.handle.net/10539/25657

Jakata, Kudakwashe (2018) Optical spectroscopy studies of ion bombarded gallium arsenide and vanadium carbide thin films, University of the Witwatersrand, Johannesburg, https://hdl.handle.net/10539/25657

Downloaded from a DSpace repository. https://dspace.org/

Optical spectroscopy studies of ion bombarded Gallium Arsenide and Vanadium Carbide thin films

Kudakwashe Jakata

A thesis submitted to the Faculty of Science, University of the Witwatersrand, and Johannesburg in fulfilment of the requirements for the degree of

Doctor of Philosophy

Johannesburg, 2018

Declaration

I declare that this thesis is my own, unaided work. It is being submitted for the degree of Doctor of Philosophy in the University of the Witwatersrand, Johannesburg. It has not been submitted previously for any degree or examination in any other university.

_____ Signature of candidate

4th of June 2018

Acknowledgements

I thank God in the words of Isaiah chapter 12: 4 – 5.

I am thankful to my supervisors, Prof J. D. Comins and Prof D. M. Wamwangi for their guidance. I am also grateful to Prof A. G Every for guidance with the theory and computational simulations, Dr R. M. Erasmus for assistance with the Raman experiments and the theory and Dr S. R. Naidoo for assistance with ion implantation experiments. I am also thankful to Dr M. Madhuku at iThemba LABS, Gauteng and Dr E. Njoroge at the University of Pretoria for assistance with Rutherford backscattering experiments.

I thank members of our research group Dr B.A. Mathe, Dr C. Sumanya and Mr M. Vhareta.

I am also grateful to the staff in the mechanical workshop whose assistance helped us to keep the equipment in our labs running: Mr J. Augustine, Mr L. Mafemba, Mr D. Mckenna, Mr V. Govender, Mr T. Mashoene and Mr A. Carpede.

Parinonyura ramangwana rinezvaro

Seri kwemadokero, hakuna muchenjeri

Seri kwemadokero, hakuna anoziva

(*O. Mtukudzi*)

Abstract

This thesis gives a report on two projects involving the use of the optical techniques of surface Brillouin scattering and Raman spectroscopy to study thin layered materials. In the first case, the thin layered material is formed from ion bombardment of a semiconductor which results in an amorphous layer on a single crystal substrate. The second case involved the study of the elastic properties of vanadium carbide deposited by RF magnetron sputtering on silicon carbide and silicon substrates.

There have been a number of reports on the recrystallization of ion implanted GaAs in which it has been noted that it is not a single step process as observed in Ge and Si. These studies have used ion channelling and Raman spectroscopy techniques to establish that the nature of the damaged gallium arsenide layer depends on the implantation conditions such as substrate temperature, implantation ion energy, and fluence. In the present work, the investigation of the recrystallization of ion implanted GaAs using the two optical spectroscopic techniques of surface Brillouin scattering (SBS) and Raman spectroscopy has been carried out for the first time.

Single crystals of (100) gallium arsenide were implanted with 100 keV argon ions at liquid nitrogen temperature using ion fluences of 2×10^{14} ions/cm^2 and 1×10^{15} ions/cm^2 on samples denoted A and B respectively. Additionally, sample C was also implanted with 100 keV argon ions but at an elevated temperature of 50 ^{o}C. Raman spectroscopy and SBS measurements are in good agreement for samples A and B showing recrystallization below 300 ^{o}C in both cases. Raman measurements on sample A, implanted at the lowest fluence, showed that before annealing was carried out a completely amorphous layer was not achieved. In the early stages of isochronal annealing on both samples A and B, the transverse optical peak is observed to have higher intensity compared to the longitudinal optical peak. At higher annealing temperatures, the longitudinal peak attains higher intensity.

Changes in the Rayleigh surface acoustic wave frequency from SBS measurements on Sample C during isochronal annealing are observed from 100 ^{o}C and saturation is obtained at about 450 ^{o}C. The Raman results show that recrystallization commences above 450 ^{o}C and saturates at about 600 ^{o}C implying complete recrystallization of the overlayer.

Vanadium carbide is a refractory material known for its high hardness, corrosion resistance, high melting point, and high electrical conductivity. There have been a number of studies on

the properties of vanadium carbides of different compositions and structures but to the best of the author's knowledge, there has never been a study on the elastic properties of the thin deposited films. Thin films of vanadium carbide have been grown using RF magnetron sputtering with varying thicknesses on SiC and Si substrates. Different deposition times were used in order to have films with varying thicknesses. X-ray reflectometry, X-ray diffraction, Rutherford backscattering, and atomic force microscopy, have been used to determine the film characteristics such as thickness, roughness, density, and stoichiometry. Surface Brillouin scattering was then carried out. The SBS results were used together with a least squares fitting approach to determine the elastic constants of the VC films computationally. A Green's function approach was used to verify the results of the fitting procedure.

Contents

1	**Introduction**	**1**
1.1	Ion implanted gallium arsenide	1
1.2	Thin films of vanadium carbide	4
1.3	Structure of this thesis	6
2	**Surface Brillouin and Raman scattering**	**7**
2.1	Theory of surface Brillouin scattering	7
2.2	SBS experimental arrangement	12
2.3	Raman scattering theory	16
2.4	Raman scattering experimental aspects	18
2.5	Summary	20
3	**Isochronal annealing of argon ion bombarded GaAs**	**21**
3.1	Sample preparation	21
3.2	Samples A and B – Low temperature and low fluence Ar^+- ion bombardment	22
3.3	Sample C - High temperature and fluence argon ion bombardment	33
3.3.1	Surface Brillouin scattering (SBS) studies	34
3.3.2	Raman scattering studies	37
3.4	Summary	41
4	**Deposition and characterization of VC thin films on 6H-SiC and Si**	**43**
4.1	Deposition of VC thin films by RF magnetron sputtering	44
4.2	X-ray reflectometry measurements	46
4.3	Structure determination by X-ray diffraction	52
4.4	Rutherford backscattering measurements	53
4.5	Atomic force microscopy	57
4.6	Summary	60

5 Surface Brillouin scattering on thin films of VC/SiC and VC/Si 61

5.1 Voigt, Reuss and Hill methods for determining elastic stiffnesses 62

5.2 Surface Brillouin scattering measurements on VC/Si 64

5.3 Surface Brillouin scattering measurements on VC/SiC 68

5.4 Summary 73

6 Discussion and conclusions 74

6.1 Ion implanted GaAs 74

6.2 Thin films of VC/Si and VC/6H-SiC 76

6.3 Future work 77

References 78

List of Figures

2.1	Laser light of wavevector $\boldsymbol{k_i}$, incident on a sample surface at an angle θ, and the backscattered light of wavevector $\boldsymbol{k_s}$.	8
2.2	Illustration of the partial wave solutions for a film and substrate.	9
2.3	A schematic diagram of the equipment used for surface Brillouin scattering measurements	13
2.4	A schematic diagram of the double shutter system incorporated in the interferometer (After the JRS Fabry-Pérot interferometer manual).	13
2.5	A schematic view of the (3+3) pass arrangement of the tandem Fabry-Pérot interferometer (Mock et al., 1987)	15
2.6	A schematic illustration of the Raman scattering process showing (I) Stokes, (II) anti-Stokes and (III) Rayleigh scattering.	17
2.7	A schematic illustration of the Raman spectrograph showing the path of the beam (Jobin-Yvon T64000 Raman spectrograph manual).	19
3.1	SRIM calculations showing the range of argon ions bombarded into GaAs at 100 keV.	22
3.2	SBS spectrum as measured at room temperature of a crystalline sample of GaAs showing the various features, namely the Rayleigh SAW peak, Lamb shoulder and the longitudinal dip. Peaks in the range of ±5 GHz are instrumental artefacts.	23
3.3	Rayleigh SAW velocity dispersion on c-GaAs as measured at room temperature by SBS. The [100] direction occurs in the troughs of the sinusoidal curve.	24
3.4	Sample A (Fluence of 2×10^{14} ions/cm^2) and Sample B (Fluence of 1×10^{15} ions/cm^2) and as measured at room temperature by SBS.	24
3.5	The respective anti-Stokes Rayleigh SAW peaks from surface Brillouin scattering measurements on crystalline GaAs, sample A (Fluence of 2×10^{14} ions/cm^2) and sample B (Fluence of 1×10^{15} ions/cm^2) as measured at room temperature by SBS.	25
3.6	Isochronal annealing	26

3.7 The surface Brillouin scattering measurements on sample A (Fluence of 2 × 10^{14} ions/cm^2) as measured at room temperature after anneal steps showing both Stokes and the anti-Stokes peaks. 26

3.8 A zoomed in view of the Rayleigh SAW anti-Stokes peaks in figure 3.7 for sample A (Fluence of 2 × 10^{14} ions/cm^2) showing the change in frequency with annealing temperature. 27

3.9 The SBS spectra from surface Brillouin scattering measurements on sample B (Fluence of 1 × 10^{15} ions/cm^2) as measured at room temperature after anneal steps showing the Stokes and anti-Stokes peaks. 27

3.10 A zoomed in view of the Rayleigh SAW anti-Stokes peaks from surface Brillouin scattering measurements on sample B (Fluence of 1 × 10^{15} ions/cm^2) from figure 3.9. 28

3.11 The frequency shifts of the respective anti-Stokes Rayleigh SAW peaks as a function of the isochronal annealing temperature on the implanted GaAs samples A (Fluence of 2 × 10^{14} ions/cm^2) and B (Fluence of 1 × 10^{15} ions/cm^2) measured at room temperature. 28

3.12 Measured Raman spectra of the crystalline GaAs sample, samples samples A (Fluence of 2 × 10^{14}) and B (Fluence of 1 × 10^{15} ions/cm^2). 29

3.13 Raman spectra collected on sample A (Fluence of 2 × 10^{14} ions/cm^2) during isochronal annealing. 30

3.14 Raman spectra intensities as measured at room temperature on sample A (Fluence of 2 × 10^{14} ions/cm^2) after each anneal step. 31

3.15 Raman spectra collected on sample B (Fluence of 1 × 10^{15} ions/cm^2) during isochronal annealing. 32

3.16 Raman spectra intensities after each anneal step as a function of the isochronal annealing temperature on the implanted GaAs sample B (Fluence of 1 × 10^{15} ions/cm^2) and measured at room temperature. 33

3.17 SBS spectra measured at room temperature on a sample of c-GaAs (Black spectrum) and of sample A after implantation (red spectrum) showing the Stokes and anti-Stokes peaks. 34

3.18 Rayleigh SAW velocities measured at room temperature sample C after implantation whilst varying the azimuthal angle. 35

3.19 Rayleigh SAW frequency shifts measured at room temperature on sample C after each anneal step as measured at room temperature showing the Stokes and anti-Stokes peaks. 35

3.20 A zoomed in view of the Rayleigh SAW anti-Stokes peaks from surface Brillouin scattering measurements on sample C from figure 3.19. 36

3.21	Rayleigh SAW frequency shifts measured at room temperature on sample C after each anneal.	36
3.22	Sezawa mode frequency shifts measured at room temperature on sample C after each anneal.	37
3.23	Raman spectra of c-GaAs at room temperature before ion bombardment (black spectrum) and after bombarding with argon ions showing the broad amorphous peak obtained (red spectrum) as measured at room temperature.	38
3.24(a)	Raman spectra measured at room temperature on sample C of a-GaAs/c-GaAs after each anneal step. The LO and TO peaks are observed at 258.8 cm^{-1} and 283.7 cm^{-1} on full recrystallization of the amorphous layer.	39
3.24(b)	Raman spectra measured at room temperature on sample C of a-GaAs/c-GaAs after each anneal step. The LO and TO peaks are observed at 258.8 cm^{-1} and 283.7 cm^{-1} on full recrystallization of the amorphous layer.	40
3.25	Raman spectra intensities as measured at room temperature on sample C of a-GaAs/c-GaAs after each anneal step.	41
4.1	Schematic of RF magnetron deposition of thin films.	44
4.2	Schematic depiction of the energetic bombardment effects on surfaces and growing films (from (Mattox, 1989)).	45
4.3	Example of typical XRR spectra showing the fringes obtained (Chason and Mayer, 1997).	48
4.4	XRR pattern using LEPTOS (blue) and measured spectra (red) for VC thin film deposited for 2.5 minutes on a Si substrate. The model has assumed the properties of a layer stack of VC/SiO_2/Si in that order.	49
4.5	XRR pattern comprising of the simulated (blue) and measured curve (red) for VC thin film deposited for 5 minutes on a Si substrate.	50
4.6	Plot of film thickness obtained from XRR against deposition time for VC thin films grown for 2.5, 5 and 7.5 minutes on a Si substrate. The linearity of the curve permits the extrapolation of film thickness produced at longer deposition times.	51
4.7	Plot of X-ray diffraction spectra obtained from the 171.4 nm thin film of VC deposited on Si.	52
4.8	IBM geometry with incident angle α, exit angle β and scattering angle θ (After Mayer, 2003).	53
4.9	Plot of RBS spectrum obtained from VC thin film deposited on Si at 100 W for 5 minutes and the fitted curve (red).	55

4.10 Plot of RBS spectra obtained from VC thin film deposited on Si at 100 W for 15 minutes and the fitted curve (red). 56

4.11 Plot of RBS spectra obtained from VC thin film deposited on Si at 100 W for 25 minutes and the fitted curve (red). 57

4.12 AFM measurement on VC deposited on SiC at 100 W for 20 minutes with a root mean square roughness of 1.6 nm. 58

4.13 AFM measurement on VC deposited on SiC at 100 W for 60 minutes with a mean roughness of 1.9 nm. 59

5.1 Anti-Stokes SBS spectra of VC/Si thin films of varying thickness deposited on Si substrates obtained using a 514.5 nm wavelength laser at a 71° angle of incidence. The spectra show an intense Rayleigh peak and a limited number of Sezawa waves. Peaks in the range of 0 to 5 GHz arise from the elastically scattered light and the instrumental shutter system. 66

5.2 Dispersion curves from the SBS spectra shown in Figure 5.1 of VC/Si thin films of varying thickness on Si substrates obtained at a 71° angle of incidence. 67

5.3 Anti-Stokes SBS spectra of VC thin films deposited on 6H-SiC substrates of varying thickness obtained using a 514.5 nm wavelength laser at a 71° angle of incidence. The spectra show an intense Rayleigh peak and an increasing number of Sezawa waves. Peaks in the range of 0 to 5 GHz arise from the elastically scattered light and the instrumental shutter system. 69

5.4 Dispersion curves from the SBS spectra shown in Figure 5.4 of VC thin films of varying thickness on 6H-SiC substrates obtained at a 71° angle of incidence. 70

5.5 Anti-Stokes SBS spectra of VC thin films deposited on 6H-SiC substrates of varying thickness obtained using a 514.5 nm wavelength laser at varying angles of incidence. The results show a substantial number of Sezawa waves. Peaks in the range of 0 to 5 GHz arise from the elastically scattered light and the instrumental shutter system. 71

5.6 Dispersion curves from the SBS spectra of VC thin films deposited on 6H-SiC substrates for data points of films measured at 71° angle of incidence (squares) and those films in which the angle of incidence was varied (triangles). The dotted lines represent the dispersion curves obtained using the elastic stiffnesses after the fitting procedure. 72

List of Tables

4.1	Parameters obtained from X-ray reflectometry measurements and simulations performed using LEPTOS on VC/Si deposited at 100 W using RF sputtering.	50
4.2	Film thicknesses and deposition times of VC/Si determined from XRR measurements.	51
4.3	Surface roughnesses for VC films deposited on SiC using tapping mode AFM measurements.	59
5.1	Calculated values of the product of film thickness and the surface phonon wave-vector $k_{\|\|}d$ for VC/Si for each layer thickness and deposition time.	65
5.2	Calculated values of the product of film thickness and the surface phonon wave-vector $k_{\|\|}d$ for VC/SiC.	68

Chapter 1: Introduction

In this work we present the use of two distinct optical techniques (surface Brillouin scattering and Raman spectroscopy) to investigate the properties of isotropic thin films created by ion-implantation and Radio Frequency magnetron sputtering respectively. In the first project, the isochronal annealing of argon ion implanted GaAs was investigated to determine the nature of the recrystallization process of the damaged layer using surface Brillouin scattering (SBS) and Raman spectroscopy. The second project investigated the elastic properties of RF magnetron sputtered vanadium carbide thin films. The optimization of the thin films has been carefully carried out by characterization using a variety of techniques to establish the stoichiometry and structural properties.

1.1 Ion implanted gallium arsenide

GaAs is a III-V direct band gap semiconductor that has been widely used for opto-electronic applications. It has a zinc blende crystal structure of space group T^2_d- F-43m and a lattice constant 5.65Å, with the Ga and As atoms being 4 fold coordinated through covalent bonding.

Ion implantation remains the widely used tool to tailor the electronic properties of semiconductors. However its application in materials leads to structural transitions and in some instances to damage of the crystal order in the material. It is thus important to understand the recrystallization of semiconductor materials subjected to dopants introduced by ion implantation as these materials need to achieve the conduction characteristics required for particular electronic components. A comprehensive review on the interaction of ion beams with materials has been given by Williams, 1986.

Suitable ion implants result in a thin amorphous layer of the semiconductor embedded on a crystalline substrate. Annealing processes are used to regain the former crystalline structure of the implanted layer. The mechanisms of recrystallization can either lead to the formation of homo-epitaxial or polycrystalline layers on the substrate. Recrystallization studies on ion implanted amorphized layers of silicon and germanium have been previously found to exhibit a single stage epitaxial process which allows for the determination of the regrowth kinetics (Gamo et al., 1977). However in the case of GaAs a similar single stage process does not take place except for a very restricted range of implantation conditions (low doses, light ions and low temperature of implantation) (Desnica-Frankovic, 1999). Instead the recrystallization

process takes place in several stages and over a wide range of temperature. The amorphization and recrystallization of GaAs has received considerable attention and a summary of the major findings is given below.

There have also been reports on the nature of damage and the emerging defects caused by ion implantation. Studies of GaAs implanted at low doses by B^+, Ar^+ and Zn^+-ions using Rutherford backscattering and transmission measurements have shown the presence of point defects and point defect complexes in the damaged layer (Wendler and Wesch, 1993). The same studies also adduce that the lattice atoms were preferentially displaced at a distance from the axis of implanted GaAs layers for low damage. The response of the damage layer to the kinetics and energetic of the annealing process has provided a diversity of results. The studies by Wendler and Wesch, 1993 on the annealing of absorbing defects after implanting the sample and maintaining the temperature at 300 K, led a decrease between 15-20% after long annealing times of 1000 hrs. These observations disagree with those reported by Sharma et al., 1989, who reported higher percentages of defect healing for short annealing times. The above results highlight the sensitivity of the different types of damage layers with different techniques. High resolution transmission electron microscopy (TEM) studies on the damage caused by individual ion cascades during implantation has shown that the size of the amorphous zones are highly dependent on the energy density within the cascades (Bench et al., 1991). At implantation temperatures below 50 K, the defect concentration was observed to be a function of the deposited energy density whereas at elevated temperatures there are annealing processes which result in a modified defect distribution (Wesch et al., 1989). It was also noted in the same report that the damaged layer of GaAs may have antisite defects and vacancies depending on the implantation temperature.

The recrystallization process in semiconductors such as germanium and silicon has been found to exhibit a single step epitaxial process which allows for the determination of the regrowth kinetics (Gamo et al., 1977). However, the nature of the amorphous layer obtained in GaAs depends on the preparation conditions and thus the subsequent recrystallization of gallium arsenide is not a single process implying a possibly different recrystallization mechanism. The recrystallization of argon-ion implanted GaAs using SBS and Raman spectroscopy provides insight on the structural and elastic stiffness changes during isochronal annealing. This is a subject of investigation in the present thesis.

The transformation from crystalline to the amorphous phase in GaAs during ion implantation has been studied using Rutherford backscattering, Brillouin and Raman spectroscopy (Sharma et al,1989). A 43 % fractional change in the Rayleigh velocity was attributed to the disorder induced by ion implantation. The numerous studies on recrystallization after ion implantation of semiconductors have steered research interests on the configuration of the amorphous layers. Intensive discussions in the literature point to the prevalence of medium and short range order in the amorphous layers produced under varied implant conditions. There have also been a number of studies reporting on the nature of amorphous GaAs obtained after implantation. One such study examined the optical evidence that ion implanted GaAs consists of micro-crystals of GaAs and amorphous GaAs (Zallen, 1992). Studies on single crystal GaAs implanted by Be^{+} - ions at 45 keV and at room temperature using Raman scattering measurements have shown that low fluences lead to a mixture of the crystalline and amorphous phases (Holtz et al, 1988).

Epitaxial regrowth of the amorphous layer has been observed for implantation doses of $3 \times 10^{13}\ cm^{-2}$ and $5 \times 10^{13}\ cm^{-2}$ (Williams and Austin, 1980b). This was done using Rutherford backscattering and ion channelling when investigating the recrystallization of GaAs implanted with 100 keV Ar^{+} - ions at doses ranging from 10^{13} to $3 \times 10^{14}\ cm^{-2}$ at liquid nitrogen temperatures. The above studies at low temperature extend similar work to those of Williams and Austin 1980a with implantation at room and elevated temperatures. Thus self-healing of the damaged layer can take place over a wide range of temperature.

Initial implant conditions, particularly implant temperatures, have been shown to affect the subsequent annealing results (Williams and Austin, 1980a, 1980b). As discussed by Desnica-Franković, 1999, while room temperature implantation in GaAs creates partial recrystallization, requiring annealing temperatures above 600 ^{o}C for the removal of residual damage, appropriate control of implant conditions can achieve regrowth at substantially lower temperatures. It was thus concluded by Ivanda et al.,1995, that the varying implantation conditions could lead to the formation of an amorphous phase having two components, namely a continuous random network and a non-random boson peak whose proportions depend on the nature of disorder.

An analysis of the Raman longitudinal phonon (LO) lineshapes obtained from GaAs implanted with 270 keV As^{+}-ions at a number of fluences up to $3.2 \times 10^{14}\ cm^{-2}$, was also carried out using the spatial correlation model (Tiong et al.,1984). These measurements were carried out

at liquid nitrogen temperatures and it was possible to relate features such as the broadening, asymmetry and the shift of the LO mode to the size of undamaged microcrystals. The spatial correlation model was also used to investigate GaAs implanted with 100 keV $^{30}Si^{+}$-ions (Desnica et al., 1997; Desnica-Frankovic, 1999). The effect of the implantation dose on the fraction of amorphous to crystalline material was investigated and a boson peak in the Raman spectra was observed.

Desnica-Franković, 1999, compared the temperature dependence of GaAs implanted by Si^{+} ions at a dose of $1 \times 10^{16}\ cm^{-2}$ at room temperature using the Raman spectroscopy. In this work the implants were annealed between 20 to 800 ^{o}C for 30 minutes. These established the presence of three broad Raman bands associated with the optical phonons in the GaAs implants after annealing below 120 ^{o}C, (Nakamura and Katoda, 1982; Wagner and Fritzsche, 1988). A background signal with lower wavenumbers had properties of a boson peak (Desnica et al., 1997; Ivanda et al.,1995). For temperatures near 160 ^{o}C the amorphous features are less prominent and a broad band emerges with two peaks at 287 and 265 cm^{-1}. The first peak is related to a crystalline longitudinal optical phonon (LO) mode while the 265 cm^{-1} corresponds to the transverse optical (TO) phonon mode. The TO peak is more intense than the LO peak showing that a relatively larger portion of the recrystallized region is randomly oriented. Above 500 ^{o}C the LO phonon mode becomes dominant indicating that the recrystallized fraction starts to follow the (100) orientation of the substrate.

In the present thesis, ion implanted GaAs has been studied using SBS and Raman spectroscopy. Ion bombardment was carried out with low fluence and at liquid nitrogen temperatures and then with high fluence and temperatures in excess of the room temperature. To the best of the writer's knowledge this is the first time surface Brillouin scattering has been to study the recrystallization of a-GaAs together with Raman spectroscopy which as discussed above gives information on the structural changes.

1.2 Thin films of vanadium carbide

There have been a number of studies on the structure of bulk vanadium carbide. Most of the studies have shown the strong dependence of the crystal structure on the fraction of carbon atoms in the bulk. It is not possible to obtain stoichiometric cubic $VC_{1.00}$ under equilibrium conditions. However, a cubic phase has been observed for VC_x with $0.86 \leq x \leq 0.89$ (Lipatnikov et al., 1997). For $0.66 \leq x \leq 0.88$ (V_6C_5) , a monoclinic symmetry was observed for space group C2 (Billingham et al.,1972) whereas trigonal symmetry was observed for space group P3

(Venables et al.,1968). The thermodynamic transitions for order-disorder of VC_x at certain values of x were investigated by Emmons and Williams, 1983.

Vanadium carbide has a high hardness (24.39 ±0.18 GPa) (Aghaie-Khafri and Fazlalipour, 2008) and melting point (T_M = 2 810 ^oC) and these unique combination of properties make it useful for industrial applications such as thin protective coatings in cutting tools.

A report on the thin film deposition of vanadium carbide using RF magnetron sputtering showed that the carbon concentration depends on the working gas pressure (Liao et al., 2005). It was also shown that the thin film could be used as a field emitter. Pulsed laser deposition (PLD) was used to grow thin films of VC on a silicon substrate in another investigation (Teghil et al., 2009). Scanning electron microscopy (SEM) showed that the nano-sized particles were formed consistent with reports on carbides deposited using the same technique (Teghil et al., 2006; Teghil et al, 2007). The films were also found to have a stoichiometry of $VC_{0.48}$ and to be amorphous.

Fluorescence-yield near edge X-ray absorption spectroscopy (FYNES), electron energy-loss spectroscopy and Auger electron spectroscopy (AES) were used to characterize thin films of VC on a vanadium (110) surface (Chen et al.,1995). The films were prepared by exposing a (100) surface of bulk vanadium to ethylene or 1,3 butadiene. It was shown that there is clustering of vanadium carbide films from 600 K to 800 K followed by diffusion of carbon atoms into the bulk.

More recently vanadium carbide coatings have been used as bonding layers to diverse cutting and heavy duty tools. Their application in this respect has reduced costs and increased savings accrued from improved tool tribological performance and life expectancy. In fact the implementation of vanadium carbide as a thin coated film on stainless steel has seen an increase in tool life by 5 to 30 times compared to uncoated tools. The increased performance has been attributed to increase in surface hardness of the coated product with reduced coefficient of friction. The utility of VC thin coatings in industrial applications necessitates the determination of the mechanical properties of these films under various structural phases. The elastic properties of materials provide essential information towards the design of materials with better mechanical properties. To this end, surface Brillouin scattering studies have been carried out to determine the elastic properties of bulk vanadium carbide (Zhang, 1998). A range of carbon to vanadium ratios was investigated and it was found that the Rayleigh surface acoustic wave

decreases with a reduction of the carbon concentration on the (100) and (110) surfaces. The elastic constants were also found to decrease with a reduction in the carbon to vanadium ratio.

A theoretical approach using density functional theory combined with the Debye quasi-harmonic approximation on a number of different bulk vanadium carbide stoichiometries was also carried out by Chong et al., 2014b. It was found that there was a large variation of the elastic constants.

This thesis focusses on the elastic properties of VC thin films grown on Si and SiC substrates using RF magnetron sputtering. X-ray reflectometry (XRR), X-ray diffraction (XRD), Rutherford backscattering spectrometry (RBS) and atomic force microscopy (AFM) were then subsequently used to determine the properties of the films such as the density, roughness, stoichiometry and film thickness. These values are required as input into the simulations which make use of a Green's function approach and a least squares fitting in order to extract the elastic constants from the surface Brillouin scattering experiments. The roughness gives an indication on the quality of the surface of the films, where a high roughness increases the noise in the SBS measurements. This is the first time that elastic constants of VC thin films have been extracted using the SBS technique.

1.3 Structure of this thesis

Chapter 2 gives a summary of the theoretical and experimental discussions of surface Brillouin scattering and Raman spectroscopy.

Chapter 3 describes the isochronal annealing studies of argon-ion implanted GaAs at liquid nitrogen temperature at low fluences and at elevated temperature at high fluence.

The deposition of vanadium carbide thin films on Si and SiC substrates is discussed in chapter 4 including the work done using several techniques such as X-ray reflectometry, Rutherford backscattering spectroscopy, atomic force microscopy, and X-ray diffraction to determine parameters such as density, film thicknesses and growth rates, surface roughness and stoichiometry.

Surface Brillouin scattering experiments on the VC thin films are described in chapter 5 and the extraction of the elastic stiffnesses. A summary of the thesis is provided in the concluding chapter 6, together with suggestions regarding additional studies.

Chapter 2: Surface Brillouin and Raman Scattering

Surface Brillouin scattering (SBS) has been used as the major experimental method to study both the annealing behaviour of ion bombarded gallium arsenide (GaAs) and the elastic properties of thin supported films. Raman spectroscopy has been used in conjunction with SBS to investigate the annealing behaviour of GaAs. Both are non-contact and non-destructive laser based techniques. The present sections give a summary of the theoretical aspects of these techniques.

2.1 Theory of surface Brillouin scattering

SBS is a technique which utilises the scattering of laser light to probe the velocity of the near surface acoustic waves of materials. There have been a number of comprehensive theoretical and experimental reports on this topic including those by Marvin et al., 1980, Bortolani at al., 1983, Beghi et al., 2012 and Comins, 2001.

From the spectra obtained from SBS experiments, several modes can be observed such as the Raleigh Surface Acoustic, Sezawa, pseudo-Sezawa and transverse and longitudinal surface acoustics waves. This information is then used as input data in a least squares fitting program to determine the elastic constants of the material.

The discussion in this section follows closely the approach by Zhang et al., 1996, and Beghi et al., 2012. In a surface Brillouin scattering experiment, a laser beam is incident on the sample in a backscattering arrangement which results in a frequency shift in the scattered light caused by the acoustic waves propagating near the surface of the sample. The scattered light is collected and the frequency shift is measured using a Fabry-Pérot interferometer. In transparent materials, the scattering occurs mainly due to bulk acoustic waves via the elasto-optic scattering mechanism while in the opaque materials which were investigated in the present work, the scattering is mainly due to the surface ripple mechanism (Marvin et al.,1980; Bortolani et al.,1983). There are additional contributions to scattering in thin films that arise

from the interface and substrate. By considering the backscattering geometry shown in figure 2.1 below, where laser light is incident on a sample surface at an angle θ, there will be inelastic scattering of this incident beam by the surface propagating phonons with a wave-vector parallel to the surface, $\boldsymbol{k}_{||}$.

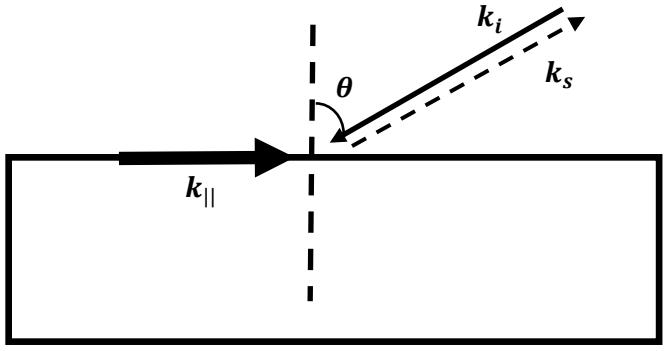

Figure 2.1.Laser light of wave-vector $\boldsymbol{k_i}$, incident on a sample surface at an angle θ, and the backscattered light of wave-vector $\boldsymbol{k_s}$.

A consideration of momentum conservation yields the expression,

$$\boldsymbol{k}_{||} = 2\boldsymbol{k_i} \sin\theta, \tag{2.1}$$

while the phonon velocity is given by,

$$V = \frac{\omega}{\boldsymbol{k}_{||}} \quad . \tag{2.2}$$

The scattering cross section for the surface ripple mechanism is given by the expression,

$$\frac{d^2\sigma}{d\Omega d\omega} = \frac{AT}{\omega} \text{Im}\, G_{33}(\boldsymbol{k}_{||}, \omega), \tag{2.3}$$

where $\text{Im}\, G_{33}(\boldsymbol{k}_{||}, \omega)$ is the imaginary part of the Fourier domain surface Green's function for force and displacement normal to the surface. A is related to the optical properties of the sample, scattering geometry, frequency and polarization of the incident light (Beghi et al., 2012).

The surface acoustic waves propagating in a layered sample are described by the wave equation,

$$\rho \frac{\partial^2 u_i}{\partial t^2} = C_{ijkl} \frac{\partial^2 u_k}{\partial x_j x_l}, \quad x_3 > 0, \tag{2.4}$$

where ρ is the density, C_{ijkl} is the fourth rank elastic modulus tensor and u_i are the particle displacement components in the layer and substrate. A solution to equation 2.4 is required which is a superposition of outgoing plane waves with amplitudes proportional to a concentrated point force, **F = (F$_j$)** which acts at the origin on the otherwise free surface of the half-space,

$$u_i(\boldsymbol{x}, t) = \int_{-\infty}^{\infty} \frac{d^2 k_{||}}{(2\pi)^2} \int_{-\infty}^{\infty} \frac{d\omega}{2\pi} \sum_{n=1}^{3} A_j^{(n)} F_j U_i^{(n)} exp\left\{ i\left(\boldsymbol{k}_{||}.x_{||} + k_3^{(n)} x_3 - \omega t \right) \right\}.$$

For each value of $k_{||}$ and ω, the equations of motion admit six plane wave solutions where the third component $k_3^{(n)}$ of **k** is a real or complex root of the characteristic sextic equation,

$$D(\boldsymbol{k}, \omega) = \left| C_{ijkl} k_j k_l - \rho \omega^2 \delta_{ik} \right| = 0. \tag{2.5}$$

All six partial waves are used for the opaque film (n = 1, 2, 3, 4, 5, 6), while there are three solutions (n = 7, 8, 9) used in the substrate because they diminish as they move away from the interface, i.e. $\mathrm{Im}\left(k_3^{(n)}\right) > 0$ as illustrated in figure 2.2.

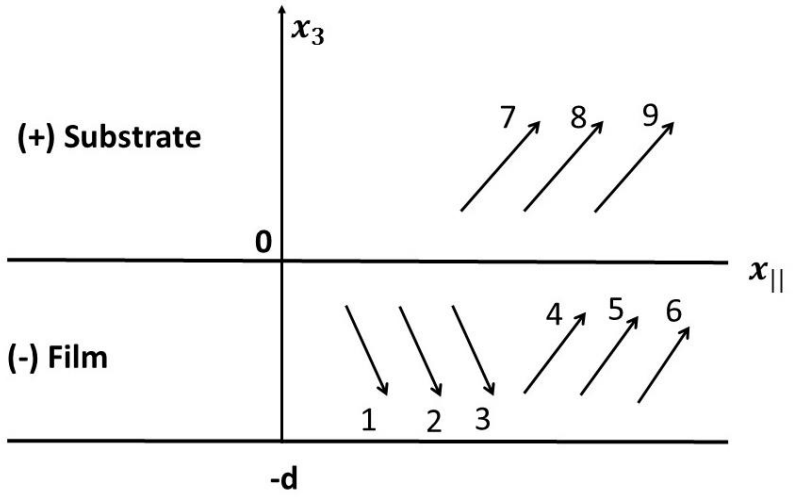

Figure 2.2. Illustration of the partial wave solutions for a film and substrate.

$\tilde{G}_{33}\left(\boldsymbol{k}_{||}, \omega\right)$ is calculated by considering the response to a δ-function force acting on the surface of the film. The displacement field in the substrate is given by,

$$u_i^+(\boldsymbol{x},t) = \int_{-\infty}^{\infty} \frac{d^2k_{||}}{(2\pi)^2} \int_{-\infty}^{\infty} \frac{d\omega}{2\pi} \sum_{n=7}^{9} A_j^{(n)} F_j U_i^{(n)} exp\left\{i\left(\boldsymbol{k}_{||}.x_{||} + k_3^{(n)} x_3 - \omega t\right)\right\}, \qquad 2.6$$

and in the film it is given by,

$$u_i^-(\boldsymbol{x},t) = \int_{-\infty}^{\infty} \frac{d^2k_{||}}{(2\pi)^2} \int_{-\infty}^{\infty} \frac{d\omega}{2\pi} \sum_{n=1}^{6} A_j^{(n)} F_j U_i^{(n)} exp\left\{i\left(\boldsymbol{k}_{||}.x_{||} + k_3^{(n)} x_3 - \omega t\right)\right\}. \qquad 2.7$$

The external force acting on the surface of the film is taken up by traction forces exerted by the film on this surface,

$$\sigma_{j3}^-\left(\boldsymbol{x}_{||}, x_3 = -h, t\right) = -\int_{-\infty}^{\infty} \frac{d^2k_{||}}{(2\pi)^2} \int_{-\infty}^{\infty} \frac{d\omega}{2\pi} \sum_{n=1}^{6} \frac{d\omega}{2\pi} F_j \delta_{jl} exp\{i\left(\boldsymbol{k}_{||}.x_{||} - \omega t\right)\}. \qquad 2.8$$

From the stress-strain relationship for the film and equation 2.8 it follows that the surface tractions are given by,

$$\sigma_{l3}^-\left(\boldsymbol{x}_{||}, x_3 = -h, t\right) = -\int_{-\infty}^{\infty} \frac{d^2k_{||}}{(2\pi)^2} \int_{-\infty}^{\infty} \frac{d\omega}{2\pi} i\omega \sum_{n=1}^{6} A_j^{(n)} F_j B_l^{(n)} exp\{i\left(\boldsymbol{k}_{||}.x_{||} - \omega t\right)\}, \qquad 2.9$$

where,

$$B_l^{(n)} = \sum_{pq} C_{lpq}^- U_p^{(n)} k_q^{(n)} exp\left\{-ik_3^{(n)} h\right\}/\omega \,, n = 1,2,3,4,5,6\,. \qquad 2.10$$

If equations 2.7, 2.8 and 2.9 are compared then three equations are obtained for the partial wave amplitudes $A_j^{(n)}$,

$$\sum_{n=1}^{6} B_l^{(n)} A_j^{(n)} = \frac{i\delta_{jl}}{\omega}, l = 1,2,3. \qquad 2.11$$

Three equations are obtained for the continuity of stress at the interface,

$$\sigma_{j3}^+\left(\boldsymbol{x}_{||}, x_3 = 0_+, t\right) - \sigma_{j3}^-\left(\boldsymbol{x}_{||}, x_3 = 0_-, t\right) = 0 \qquad 2.12$$

which gives,

$$\sum_{n=1}^{9} B_l^{(n)} A_j^{(n)} = 0, l = 4,5,6. \quad 2.13$$

where

$$B_l^{(n)} = \sum_{pq} C_{3l-3pq}^{+} U_p^{(n)} k_q^{(n)} / \omega \, , n = 7,8,9 \; l = 4,5,6 \quad 2.14$$

and

$$B_l^{(n)} = -\sum_{pq} C_{3l-3pq}^{-} U_p^{(n)} k_q^{(n)} / \omega \, , n = 1,2,3,4,5,6 \;\; l = 4,5,6. \quad 2.15$$

There are three expressions for the partial wave amplitudes from the continuity of the displacement field at the boundary,

$$u_i^{+}(\boldsymbol{x}_{||}, x_3 = 0_{+}, t) - u_i^{-}(\boldsymbol{x}_{||}, x_3 = 0_{-}, t) = 0 \quad 2.16$$

and this gives,

$$\sum_{n=1}^{9} B_l^{(n)} A_j^{(n)} = 0, l = 7,8,9. \quad 2.17$$

where

$$B_l^{(n)} = U_{l-6}^{(n)}, l = \; 7,8,9, n = 7,8,9 \quad 2.18$$

and

$$B_l^{(n)} = -U_{l-6}^{(n)}, l = \; 7,8,9, n = 1,2,3,4,5,6,7,8,9. \quad 2.19$$

The solution of the equations 2.11, 2.14 and 2.18 is,

$$A_j^{(n)} = \frac{i}{\omega} (B^{-1})_j^{(n)}, j = 1,2,3. \quad 2.20$$

The displacement Green's function $G_{33}(\boldsymbol{x}, t)$ at the surface is then obtained from equation 2.7 and is given by,

$$G_{33}(\boldsymbol{x}_{||}, x_3 = -h, t) = \int_{-\infty}^{\infty} \frac{d^2 k_{||}}{(2\pi)^2} \times$$

$$\int_{-\infty}^{\infty} \frac{d\omega}{2\pi} \left\{ \sum_{n=1}^{6} \frac{i}{\omega} (B^{-1})_3^{(n)} U_l^{(n)} exp\left(-k_3^{(n)} h\right) \right\} exp\{i(\boldsymbol{k}_{||}.\boldsymbol{x}_{||} - \omega t)\}, \qquad 2.21$$

2.2 Experimental arrangement

A Coherent Innova 300 series laser was used to produce the SBS spectra reported in this thesis. The lasers has a ceramic tube containing argon gas. An electric discharge excites the neutral atoms into an ionised state from which the atoms will decay into the 4p energy level. The relatively long lifetime of the 4p level atoms establishes a population inversion. The 4p atoms ultimately decay to the 4s level. The transition from the 4p level to the 4s level can be facilitated by stimulation with a photon of equivalent energy which results in the emission of a monochromatic and coherent beam of light, i.e. laser light.

The laser was used in TEM00 mode which provides a Gaussian beam. It was fitted with an etalon to prevent mode-hopping and a Brewster window to insure a vertically polarised beam. The argon-ion laser emits several wavelength lines with the highest intensity being obtained for the 514 nm, 488 nm and the 457 nm.

Figure 2.3 shows the surface Brillouin scattering experimental arrangement. The argon-ion laser emits a 514.5 nm wavelength beam which is split into two beams by a beam splitter. Of the two, the reference beam is directed towards the shutter whilst the other passes through an acousto-optic modulator (AOM) which is used to adjust the intensity of light falling on the sample. After passing through the AOM, the beam is directed by a mirror, guided through a pin-hole on an elliptical mirror and then focused onto the sample by a lens, OL1. The scattered light is collected by the same lens, OL1, then directed towards lens OL2 which has got a focal point at the entrance pinhole to the interferometer. The walking mirrors direct the light into the interferometer pinhole.

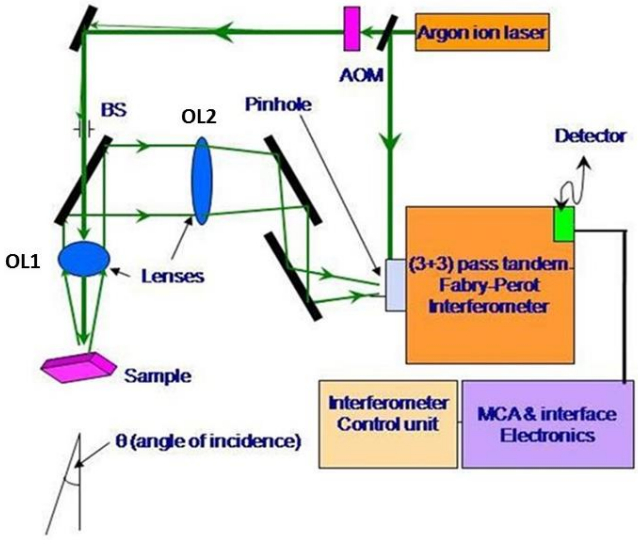

Figure 2.3. A schematic diagram of the equipment used for surface Brillouin scattering measurements.

A double shutter system is installed just after the entrance pinhole to the interferometer as shown in figure 2.4 below.

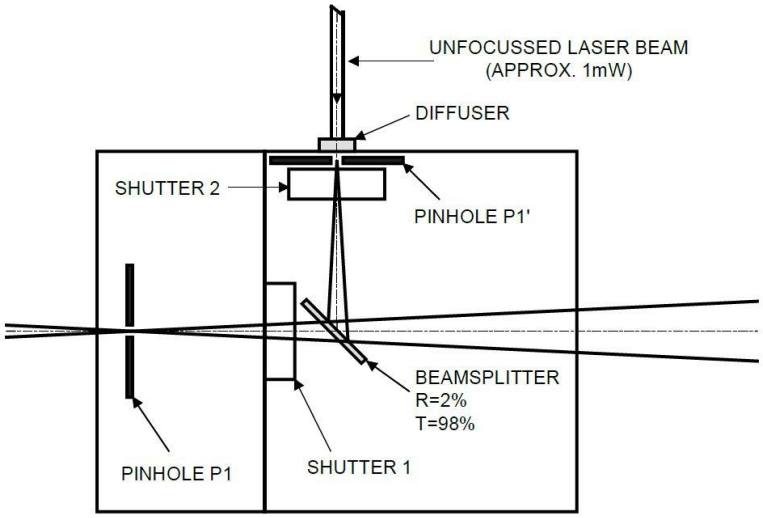

Figure 2.4. A schematic diagram of the double shutter system incorporated in the interferometer (After the JRS Fabry-Pérot interferometer manual).

Following the JRS Fabry-Pérot interferometer manual, when the intensity of the elastically scattered light is too high, the control unit closes shutter 1 while scanning through the elastic peak. The reference beam then enters through the secondary pinhole for stabilisation with shutter 2 open. Alternatively, if the extra light signal from the secondary pinhole disturbs the

measurement, then shutter 2 is opened for a cycle of 16 stabilization scans while a signal from the multi-channel analyser is gated off. During the next 16 scans shutter 2 is closed and the experimental signal is recorded. The cycle repeats. The shutter specifications are an open or close time of 2.5 ms, and maximum timing jitter of 0.5 ms.

A comprehensive discussion of the design of the JRS Fabry-Pérot interferometer (FPI) used in the SBS measurements reported here is given in the US patent by Sandercock, 1980. A brief outline is given here closely following this report and the one by Mock et al., 1987. Figure 2.5. shows a schematic view of the tandem Fabry-Pérot interferometer.

The Fabry-Pérot interferometer has two sets of mirrors each of which are mounted parallel to each other with a variable spacing, FP1 and FP2 in figure 2.5. Transmission of the light falling on the interferometer for a distance L_1 between each set of parallel mirrors is determined by the expression,

$$T = \frac{\gamma_0}{1 + \frac{4F^2}{\pi^2} sin^2 \frac{2\pi L_1}{\lambda}}\ , \qquad 2.22$$

where F is the finesse which related to the mirror reflectivity and flatness and γ_0 is the maximum possible transmission. From equation 2.22, the peak transmission is obtained for wavelengths satisfying the equation,

$$L_1 = n\left(\frac{\lambda}{2}\right), \qquad 2.23$$

where n is an integer. The free spectral range (FSR) is the distance between successive transmitted wavelengths and is related to the finesse and resolution $\gamma\lambda$. In the Sandercock type FPI used for the SBS measurements, the FSR is increased by making use of the two sets of parallel mirrors with the second set having a spacing L_2. The interferometer has $L_2/L_1 = 0.95$ which means that the adjacent transmission peaks coincide after 20 times the FSR of the first set of parallel mirrors.

The tandem Fabry-Pérot interferometer can attain a high contrast ~ 10^{12} (Mock et al.,1987). This is possible when stray reflections have been eliminated from falling on the mirrors, detector and the two interferometers. A schematic of the (3+3) passes of the laser light through the FP1 and FP2 is shown in figure 2.5 below. Scattered light from the sample is directed onto FP1 by mirror M1 then the deflection mirror directs it to FP2 where it has undergone 2 passes.

Total internal reflection at two faces of corner cube 2 then direct the light back through FP2, and now because it is laterally shifted, the light passes through FP1 and reaches corner cube1 and it has now passed 4 times. From corner cube 1 it makes 2 more passes and is then directed towards the detector by mirror M2.

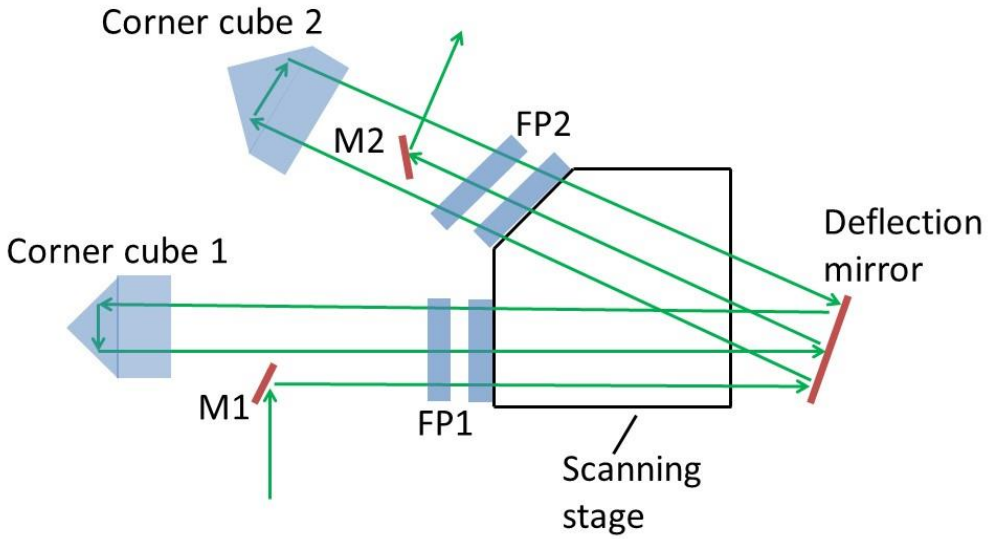

Figure 2.5. A schematic view of the (3+3) pass arrangement of the tandem Fabry-Pérot interferometer (Mock et al., 1987).

An SBS measurement is typically performed for several hours depending on whether the sample provides a weak or strong scattered light signal. Thermal and mechanical stability have to be maintained throughout the measurement. This is achieved by electronic circuits which make use of piezoelectric transducers and feedback loops which make corrections for mirror spacing and parallelism. The interferometer is isolated from vibrations and from sounds which can excite resonances. This is achieved by mounting all components of the interferometer on an optical bench on dynamic isolation mounts provided by JRS Scientific Instruments, Vibration Isolation System MOD-2.

A detector collects the light that has been scattered from the sample and passed through the FPI. The detector used is an avalanche diode detector manufactured by EG & G Optoelectronics and it has a dark count of 1 per second. An RS232 interfacing cable is used to pass data from the detector to a computer based multichannel analyser (MCA) to record the spectra. The multichannel analyser makes use of a software called GHOST v. 6.00 which was supplied by JRS Scientific Instruments. GHOST has functions for curve-fitting and data analysis which were not used as the data was analysed using ORIGIN LAB v.8 software.

2.3 Raman scattering theory

When laser light is incident on a sample with a frequency, ν, Tyndall, Rayleigh and Raman scattering occur. Tyndall scattering does not result in a frequency change of the scattered light and can be attributed to macromolecular particles in the sample. Some of the light is elastically scattered without a change in frequency and this is called Rayleigh scattering. Raman scattering occurs when some of the incident beam is inelastically scattered with a change in frequency. The interaction of the laser light with the sample induces vibrations which are referred to as transverse modes when they are in a direction which is perpendicular to the incident radiation and longitudinal if they are along the same direction. When the frequencies of these vibrations have low energies and frequencies, they fall within the acoustic ranges. In this case, they are called longitudinal acoustic (LA) and transverse acoustic (TA) modes. Higher energy vibrations are referred to as optic modes and called longitudinal optic (LO) and transverse optic (TO) modes (Smith and Dent, 2013). There have been a number of theoretical and experimental reports on the Raman effect (Hayes, 1975; Bauer and Richter, 1996) and the following is a brief summary.

The quantum approach describing the Raman effect is as follows: (Chalmers and Griffiths, 2002). Suppose a crystal is in a vibrational state *b*, see figure 2.5(a), and then absorbs a photon with energy $h\nu_i$ which raises the system to an intermediate higher energy state. This intermediate state has a very small lifetime of ~10^{-14} seconds and the system will emit a photon. If the emitted or scattered photon has less energy than the absorbed photon, i.e., $h\nu_s < h\nu_i$, then it is called a Stokes transition and the residual energy, $h\nu_i - h\nu_s = h\nu_{ab}$, raises the molecule to a higher vibrational state, *a*.

The crystal may, after absorbing a photon, drop back to a lower energy level, *c*, if it was initially in an excited state. This means $h\nu_s > h\nu_i$, and some of the vibrational energy of the crystal is radiated since $h\nu_s - h\nu_i = h\nu_{bc}$, and this is called an anti-Stokes transition. This situation is illustrated in figure 2.5(b). Rayleigh scattering is shown in figure 2.5(c) where the incident photon energy is equal to the scattered photon energy, $h\nu_s = h\nu_i$, but the direction of the emitted photon may not be in the same direction as that of the incident. The differences between the incident and emitted photon frequencies correspond to specific energy levels differences for the material being investigated and so give information on the structure.

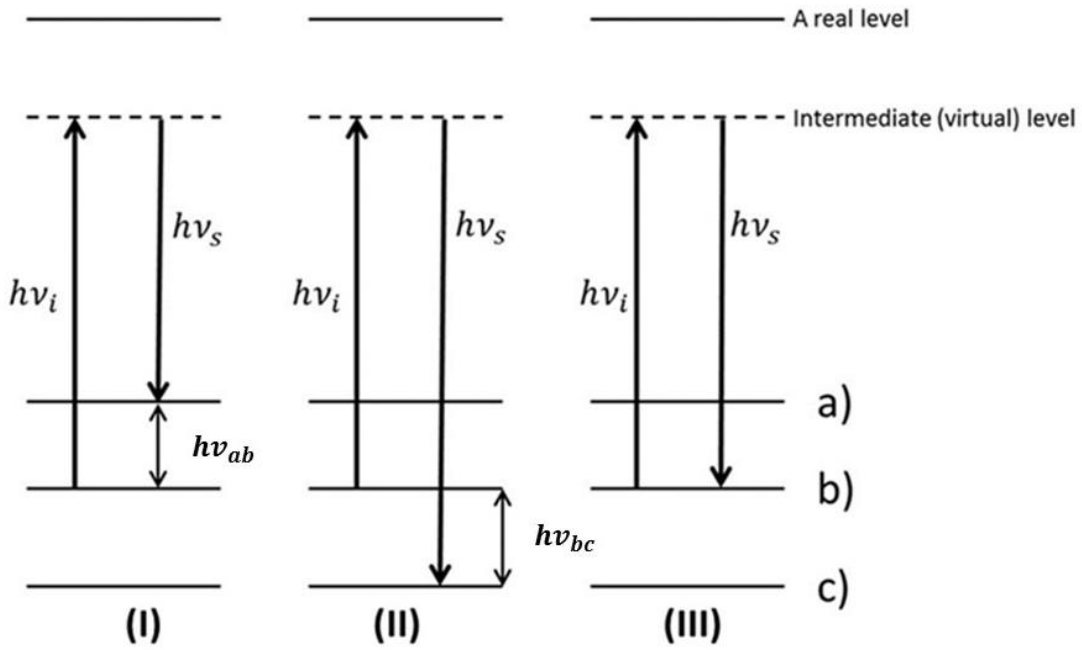

Figure 2.6. A schematic illustration of the Raman scattering process showing (I) Stokes, (II) anti-Stokes and (III) Rayleigh scattering.

In the classical approach to describing the Raman effect, electromagnetic radiation incident on a sample is considered (Bauer and Richter, 1996). The electric field, **E**, will induce an atomic dipole, μ, given by,

$$\mu = \alpha E + \frac{1}{2}\beta EE + \frac{1}{6}\gamma EEE + \cdots$$

which to a first approximation gives,

$$\mu = \alpha E, \qquad 2.24$$

where α is the polarizability of the sample and β is the hyper-polarizability and γ is the second hyper-polarizability. The electric field, **E**, and the polarizability, α, respectively are vectors and α is a tensor. The polarizability is anisotropic such that the induced dipole aligns itself in the direction of the greatest polarizability. So equation 2.24 can be modified with the polarizability tensor, α_{ij}, based on the Cartesian axes *x*, *y* and *z* as follows,

$$\begin{aligned} \mu_x &= \alpha_{xx}E_x + \alpha_{xy}E_y + \alpha_{xz}E_z \\ \mu_y &= \alpha_{yx}E_x + \alpha_{yy}E_y + \alpha_{yz}E_z \\ \mu_z &= \alpha_{zx}E_x + \alpha_{zy}E_y + \alpha_{zz}E_z \end{aligned} \quad . \qquad 2.25$$

It has been shown that the variation of the molecular polarizability with respect to the normal coordinates can be expressed by a Taylor expansion (Bauer & Richter, 1996; Kuzmany, 2010),

$$\alpha_{ij} = (\alpha_{ij})_0 + \sum \left(\frac{\partial \alpha_{ij}}{\partial Q_k}\right) Q_k + \frac{1}{2} \sum \left(\frac{\partial^2 \alpha_{ij}}{\partial Q_k \partial Q_l}\right) Q_k Q_l + \cdots \quad 2.26$$

where $(\alpha_{ij})_0$ is the equilibrium value of the polarizability tensor α and Q_k is the kth normal coordinate associated with vibrations of wavenumber v_k (Bauer and Richter, 1996). If small vibrations are considered close to the equilibrium position then equation 2.26 can be written as,

$$\alpha_k = \alpha_0 + \left(\frac{\partial \alpha}{\partial Q_k}\right)_0 Q_k \quad 2.27$$

The time dependence of Q_k is then obtained by considering harmonic vibrations of the molecule and is given by,

$$Q_k = Q_{k0} \cos 2\pi v_0 t \quad 2.28$$

with Q_{k0} as the normal coordinate amplitude. The variation of the electric field vector **E** when light with a frequency v_0 is incident on a sample is given by,

$$E = E_0 \cos 2\pi v_0 t \, . \quad 2.29$$

It then follows that,

$$\mu = E\alpha_0 + \left(\frac{\partial \alpha}{\partial Q_k}\right)_0 E_0 Q_{k0} \cos 2\pi v_0 t \cos 2\pi v_k t$$

$$= E\alpha_0 + \left(\frac{\partial \alpha}{\partial Q_k}\right)_0 Q_{k0} E_0 [\cos 2\pi (v_0 - v_k)\, t + \cos 2\pi (v_0 + v_k)]. \quad 2.30$$

Equation 2.30 is obtained by combining equations 2.24, 2.27, 2.28 and 2.29 and shows that the linear induced dipole has three distinct frequency components. The first term describes the Rayleigh scattered light, the second term represents the Stokes Raman process and the third term represents the anti-Stokes Raman process.

2.3 Raman scattering experimental aspects

The following discussion of the experimental aspects of Raman spectroscopy closely follows the description by Bauer and Richter, 1996. Lasers provide the most convenient and efficient light source for Raman spectroscopy measurements. In our case, the 514.5 nm wavelength laser

light from a Coherent Innova 300 series argon-ion laser was used. A schematic diagram of the Jobin-Yvon T64000 Raman spectrograph used to collect Raman spectra is shown in figure 2.6.

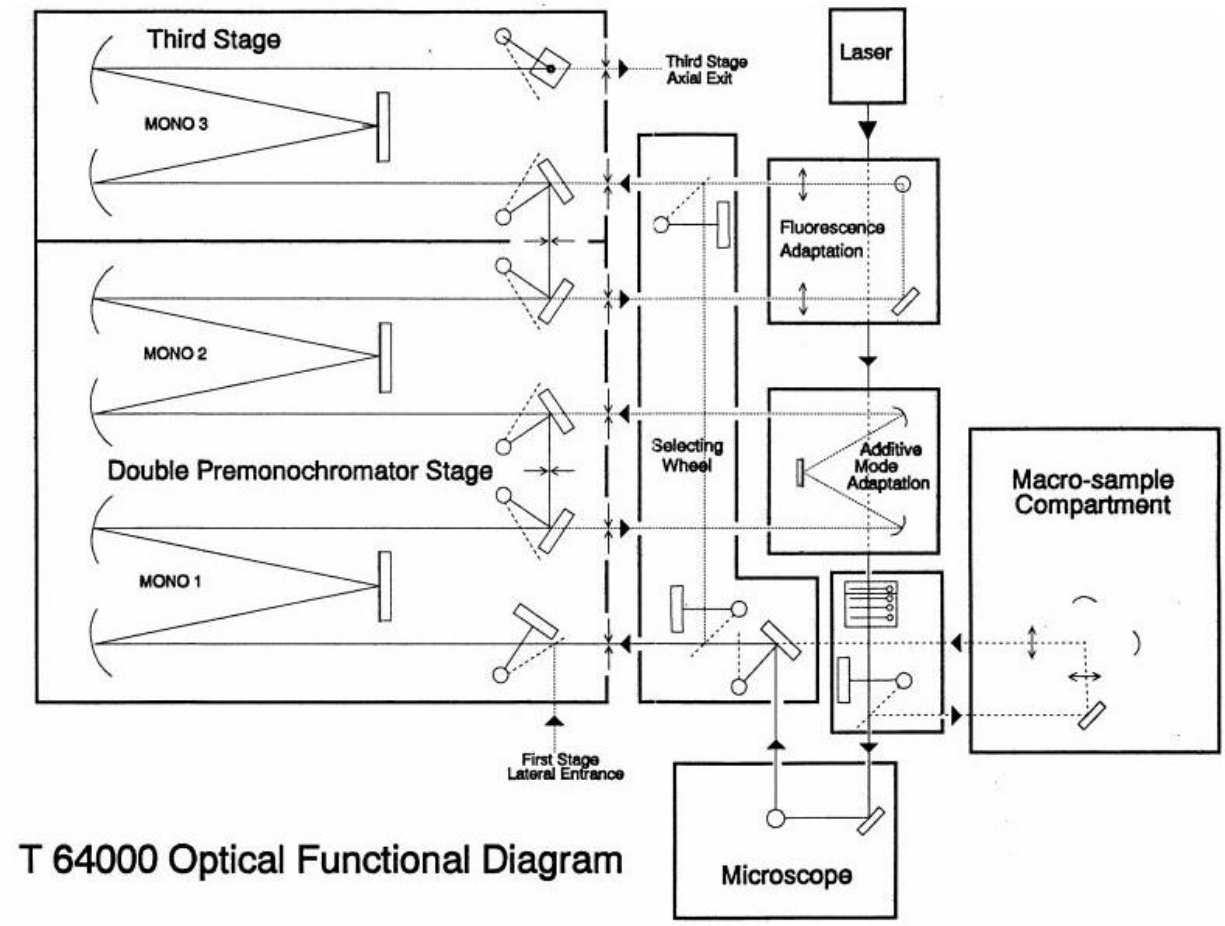

Figure 2.7. A schematic illustration of the Raman spectrograph showing the path of the beam (Jobin-Yvon T64000 Raman spectrograph manual).

The laser light is focused onto the sample using an Olympus BX40 microscope attached to the spectrograph whilst a narrow band pass filter is used to select the wavelength that enters the microscope. The light scattered from the sample is analysed in either the single spectrograph mode, or in triple subtractive mode or in triple additive mode. A monochromator with high contrast is used to analyse the scattered light and in some cases, a double or triple monochromator separates the Raman light from the Rayleigh scattered light (Bauer and Richter, 1996).

In the single spectrograph mode, the scattered light passes through a holographic notch filter which suppresses the elastically scattered component whilst allowing the Raman scattered light to pass through. After transmission through the notch filter, the Raman scattered light then falls

on a grating where it is dispersed and then detected by a charged coupled device (CCD) where a spectrum is produced. In triple subtractive mode, two pre-monochromators disperse the scattered light and then recombines it before it is re-dispersed by the spectrograph. It has a lower throughput than the single spectrograph mode but is efficient in removing stray light from the laser excitation line which allows for analysis at low wavenumbers.

For the triple additive mode, the three monochromators act as dispersers which gives a narrow range of wavelengths spread across the detector and so gives higher resolution.

The detector used is a multichannel charged coupled device (CCD). It produces a photoelectron current proportional to the intensity of the scattered radiation falling on the detector. The CCD has to be cooled to liquid nitrogen temperatures for optimum performance. The single spectrograph mode is useful when high throughput and short analysis time are required.

2.3 Summary

An overview of the theoretical and experimental aspects of the surface Brillouin scattering and Raman spectroscopy techniques used in the present studies has been given. They are both non-contact and non-destructive laser based techniques.

Surface Brillouin scattering occurs when there is a Doppler shift in the frequency of laser light that is scattered from a sample due to thermally excited surface acoustic waves. This shift is measured using a tandem Fabry-Pérot interferometer which has a contrast of ~ 10^{12}. It makes use of two sets of parallel mirrors which are mounted accurately parallel to each other and where the spacing between the mirrors determines the wavelength of the scattered light that may be transmitted. The frequency shifts obtained from these measurements are related to the velocity of the surface acoustic waves which is also related to the elastic stiffnesses of the sample being analysed.

The Raman scattering technique makes use of laser light which when incident on a sample, there is a component of elastically scattered light resulting from the Rayleigh effect. There is also a component of inelastically scattered light emanating from the Raman effect. The Raman spectra of a sample shows the scattered frequencies which are related to the actual energy states in the sample. This information can be used to determine the structure of the material.

Chapter 3: Isochronal annealing of argon ion bombarded GaAs

A major part of the present chapter concerns the results of the bombardment of GaAs single crystals (c-GaAs) with argon ions thus forming a thin layer of amorphous GaAs on a crystalline GaAs substrate (a-GaAs/c-GaAs). A summary of the elastic constants of GaAs obtained using theoretical approaches such as the dipole model, shell model, *ab initio* lattice dynamics and continuum elasticity theory has been presented by Jakata and Every, 2008. The values of the elastic constants for the (100) oriented crystalline gallium arsenide are $C_{11} = 120$ GPa, $C_{44} = 58$ GPa, and $C_{12} = 57.6$ GPa . These elastic constants are expected to be modified in the damaged layer after ion implantation. The c-GaAs wafers were obtained from the Physics Department at the University of Pretoria (Professor F.D. Auret) with (100) orientation with dimensions of 4×3 mm^2. These samples were subsequently subjected to high temperature annealing during which the recrystallization processes were studied by Raman scattering and surface Brillouin scattering (SBS).

3.1 Sample preparation

Ion bombardment is a well-established technique that can be used to change a material from the crystalline phase to an amorphous phase (Williams, 1986; Desnica et al., 1997; Desnica-Francovic, 1999). It involves the acceleration of a beam of charged particles onto a material. This can result in sputtering, atomic mixing, damage or implantation (Williams 1986). Atomic displacements result from collisions between the incident ions and the atoms that make up a material. The recoil of the atoms then results in their nearest neighbours being dislodged from their lattice positions causing a damage cascade. In the present experiments ion bombardments of the respective samples were carried out at iThemba Laboratory for Accelerator Based Sciences, Gauteng.

Three samples were prepared using a single crystal wafer of gallium arsenide with (100) orientation. These were placed at an angle of 7° off axis to prevent channelling and the ion beam diameter was significantly larger than the surface area of the samples. Sample A was bombarded with a fluence of 2×10^{14} ions/cm^2 while sample B was bombarded with a fluence of 1×10^{15} ions/cm^2. This was done at an energy of 100 keV and an ion beam current of ~0.2

μA while keeping both samples A and B at liquid nitrogen temperature. Sample C was bombarded at a temperature of approximately 50°C due to ions heating the target whilst using a scanned beam which reduces the thickness of the amorphous layer (Williams and Austin, 1980a). A fluence of 5 ×10^{16} ions/cm^2, energy of 100 keV and an ion beam current of about 2.5 μA were used for the argon-ion bombardment in sample C. Ion bombardment produces a thin amorphous layer of GaAs above a crystalline GaAs (c-GaAs) substrate. It is expected that the thickness of the damaged layer is the same for all samples because they have been irradiated at 100 keV and from the SRIM calculations in figure 3.1, a damaged layer of about 140 nm is obtained. However, for the samples implanted at low fluence, there will be less damage but the liquid nitrogen temperatures reduce the degree of self-annealing occurring during bombardment. Whereas, for sample C implanted at a much higher fluence and current density, there is more damage but also possible self-annealing due to the high temperature (Haynes and Holland, 1991; Robinson *et al*, 1994). Therefore, the SRIM simulations only show the damage depth obtainable by dose and energy without the effects of temperature.

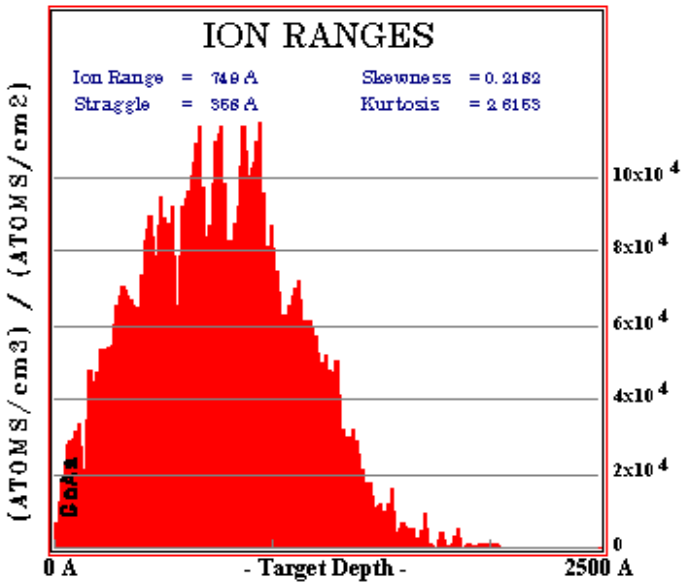

Figure 3.1: SRIM calculations showing the range of argon ions bombarded into GaAs at 100 keV and fluence of 5 ×10^{16} ions/cm^2.

3.2 Samples A and B - Low temperature and low fluence argon ion bombardment

As discussed in section 3.1, sample A was bombarded with a fluence of 2 × 10^{14} ions/cm^2 and sample B with a fluence of 1 × 10^{15} ions/cm^2 both with energy 100 keV and at liquid nitrogen

temperature. An amorphous layer was formed in each case as shown by measurements which follow in this chapter.

Surface Brillouin scattering studies

Surface Brillouin scattering is a laser based technique that can be used to probe the surface acoustic waves propagating on a material dependent on the difference in elasticity of the upper layer and the lower layer. A summary of the experimental and theoretical aspects of this technique have been highlighted in chapter 2 of this thesis. The power of the laser beam incident on the sample was less than 100 mW and an angle of incidence of 71° was used for all experiments. An SBS spectrum obtained on a crystalline sample of GaAs is shown in figure 3.2. The Stokes and anti-Stokes Rayleigh surface acoustic waves (SAW) modes, the broad central peak which is due to the elastically scattered light as well as the Lamb shoulder and the longitudinal dip are illustrated.

In an SBS measurement, the position of the Rayleigh peak varies with the anisotropy of the material being investigated. A measurement of this variation in frequency is shown in figure 3.3 for a (100) oriented crystalline GaAs sample illustrating the variation of the Brillouin acoustic wave velocity with respect to the direction of propagation of the Rayleigh SAW.

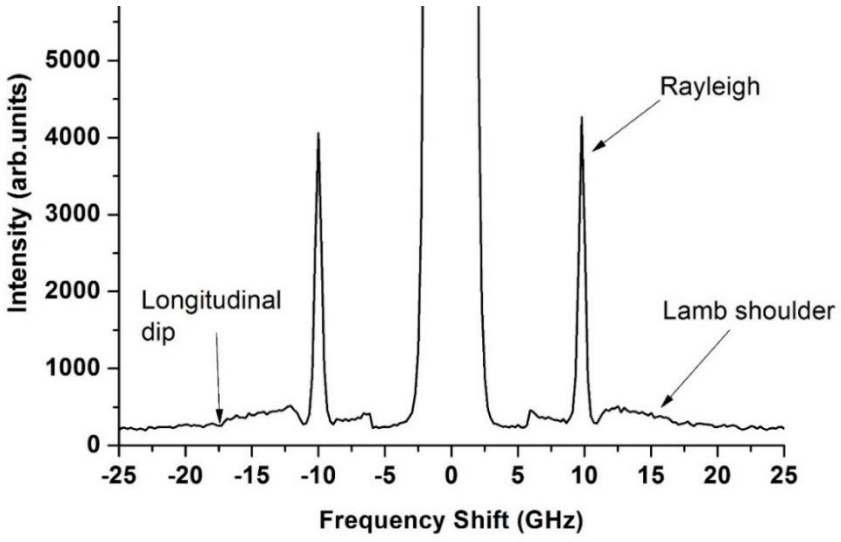

Figure 3.2: SBS spectrum as measured at room temperature of a crystalline sample of GaAs showing the various features, namely the Rayleigh SAW peak, Lamb shoulder and the longitudinal dip. Peaks in the range of ± 5 GHz are instrumental artefacts.

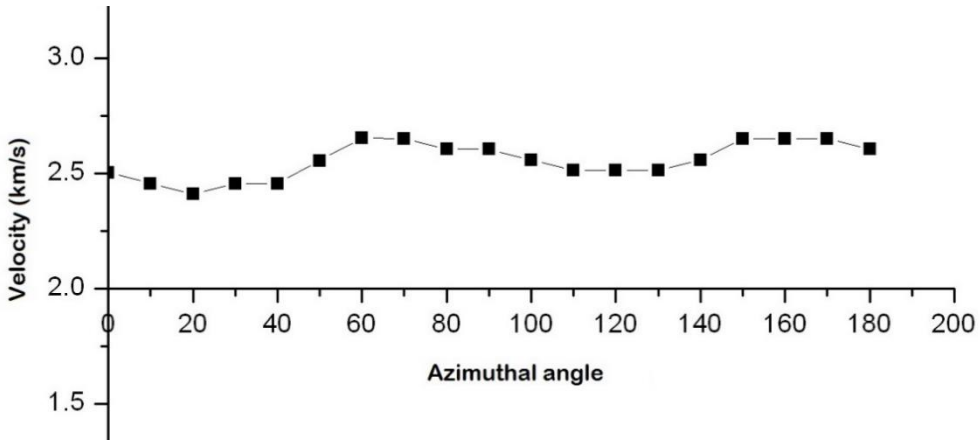

Figure 3.3: Rayleigh SAW velocity dispersion on c-GaAs as measured at room temperature by SBS. The [100] direction occurs in the troughs of the sinusoidal curve.

Surface Brillouin scattering frequency dispersion measurements collected on samples A and B after implantation indicate a high degree of isotropy as shown in figure 3.4. The velocity of the Rayleigh SAW of sample A which was implanted at a lower fluence is higher than that of sample B implanted at a higher fluence as illustrated in figures 3.4 and 3.5. This suggests that sample A implanted at the lower ion fluence has become more disordered in the implanted layer compared to sample B. These Brillouin scattering results show that sample A is elastically harder than sample B. The Rayleigh SAW peak for sample A is at 7.9 GHz whilst that for sample B is at 8.5 GHz, as shown in figure 3.5. Comparing the above results with the Rayleigh SAW peaks of the crystalline gallium arsenide sample shows that ion implantation leads to an (elastically soft overlayer on (100) GaAs). These measurements were conducted at room temperature.

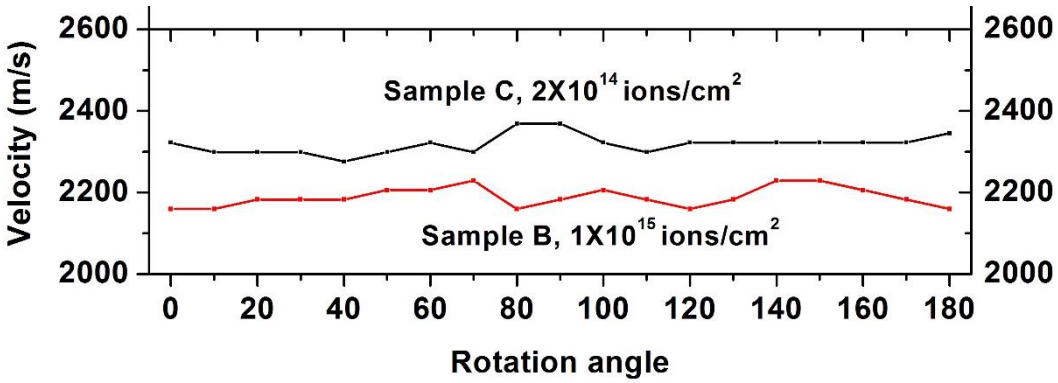

Figure 3.4: Dispersion curves for Sample A (Fluence of 2×10^{14} ions/cm^2) and Sample B (Fluence of 1×10^{15} ions/cm$^{2)}$ as measured at room temperature by SBS.

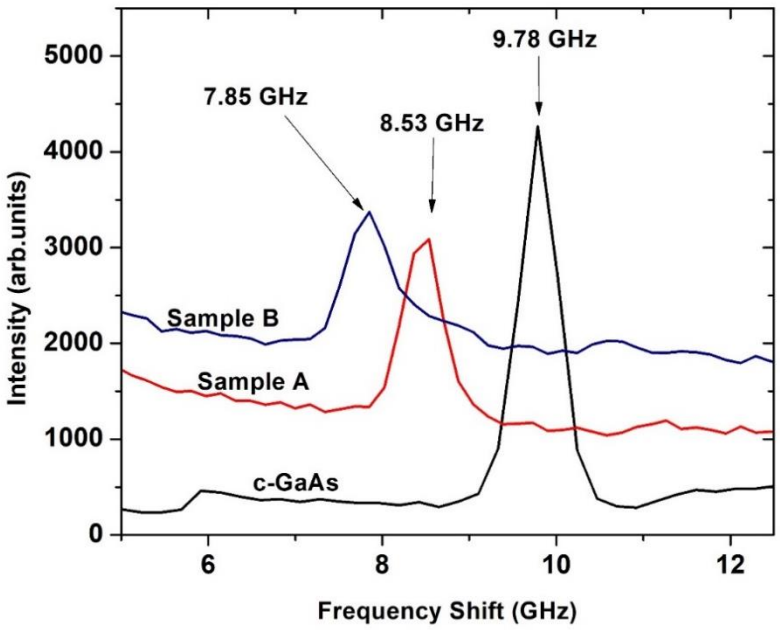

Figure 3.5: The respective anti-Stokes Rayleigh SAW peaks from surface Brillouin scattering measurements on crystalline GaAs, sample A (Fluence of 2×10^{14} ions/cm^2) and sample B (Fluence of 1×10^{15} ions/cm^2) as measured at room temperature by SBS.

Isochronal annealing was then carried out on samples A (Fluence of 2×10^{14} ions/cm^2) and B (Fluence of 1×10^{15} ions/cm^2) whilst performing Raman and SBS measurements as indicated by Figure 3.6. A Linkam heating stage was used to bring each sample to the required anneal temperature, with room temperature being the initial base temperature. Heating in a sequence of anneal temperatures was carried out at a rate of 10° C per minute after which the sample was kept at the annealing temperature for 20 minutes then cooled down to room temperature at 10° C per minute. After each anneal step, Raman and SBS spectra were acquired at room temperature before heating up to the next annealing temperature. It was expected that recrystallization would be achieved below 300° C for the samples A and B implanted at low fluence and liquid nitrogen temperature based on reports by Williams and Austin, 1980. This information led to the use of smaller temperature incremental steps. Argon ion lasers were used for both the SBS and Raman experiments. The SBS peak intensities vary as seen in figures 3.7 - 3.10 because of different acquisition times resulting from limited measurement duration. However, this has no effect on the peak positions.

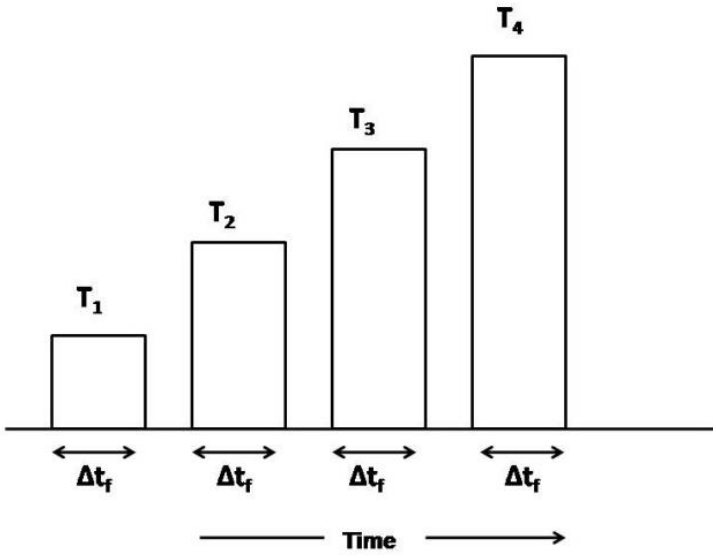

Figure 3.6: Isochronal annealing.

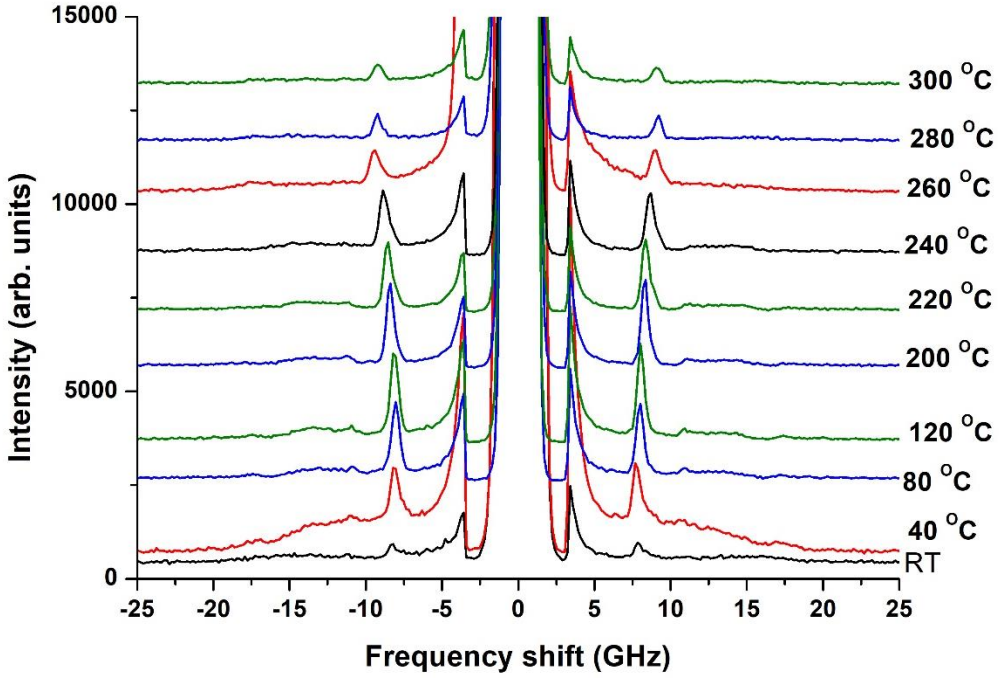

Figure 3.7: The surface Brillouin scattering measurements on sample A (Fluence of 2×10^{14} ions/cm^2) as measured at room temperature after anneal steps showing both Stokes and the anti-Stokes peaks.

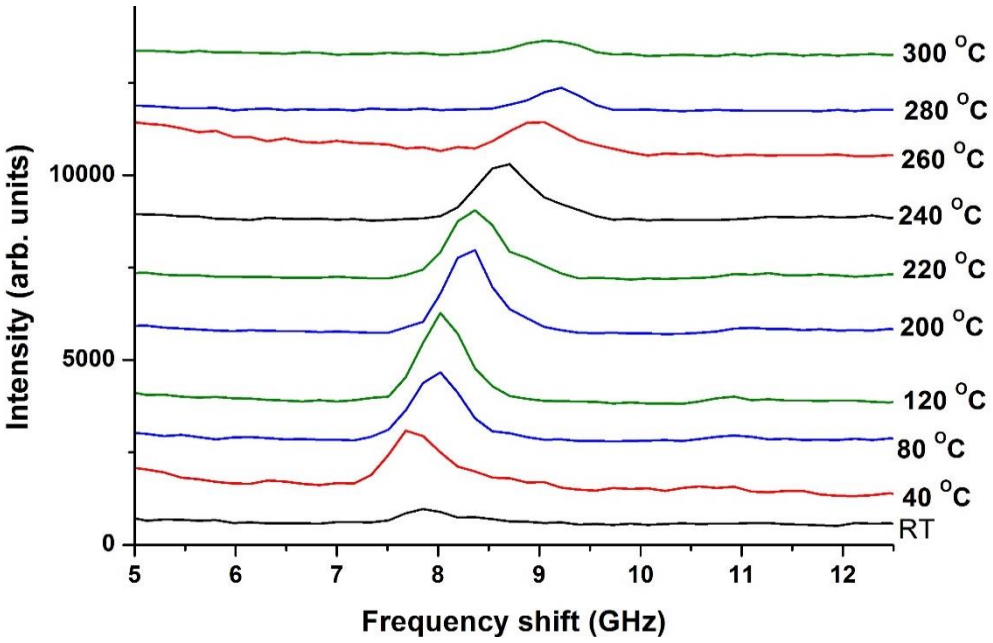

Figure 3.8: A zoomed in view of the Rayleigh SAW anti-Stokes peaks in figure 3.7 for sample A (Fluence of 2×10^{14} ions/cm^2) showing the change in frequency with annealing temperature.

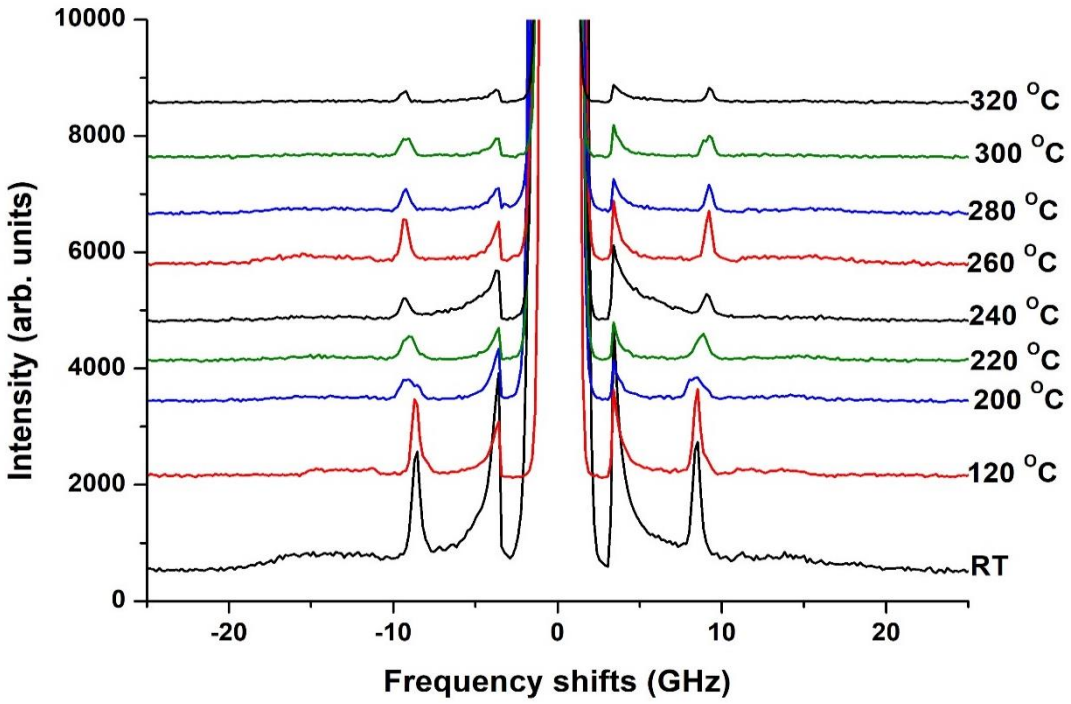

Figure 3.9: The SBS spectra from surface Brillouin scattering measurements on sample B (Fluence of 1×10^{15} ions/cm^2) as measured at room temperature after anneal steps showing the Stokes and anti-Stokes peaks.

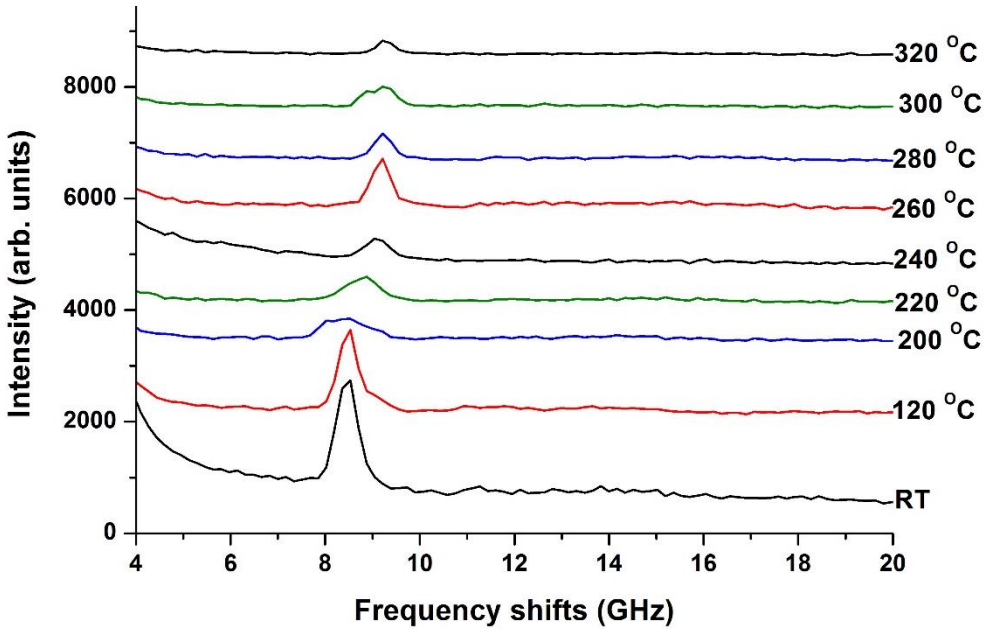

Figure 3.10: A zoomed in view of the Rayleigh SAW anti-Stokes peaks from surface Brillouin scattering measurements on sample B (Fluence of 1×10^{15} ions/cm^2) from figure 3.9.

The SBS results from samples A and B shown in figures 3.8 and 3.10 indicate the positions of the anti-Stokes Rayleigh SAW peaks after some of the anneal steps. It is seen that the frequency shifts obtained after annealing are increased with increasing annealing temperature.

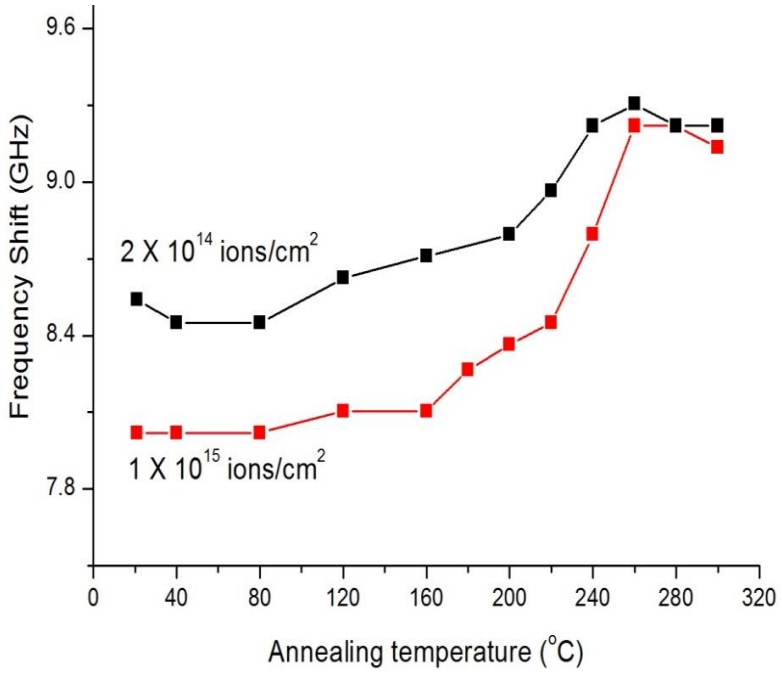

Figure 3.11: The frequency shifts of the respective anti-Stokes Rayleigh SAW peaks as a function of the isochronal annealing temperature on the implanted GaAs samples A (Fluence of 2×10^{14} ions/cm^2) and B (Fluence of 1×10^{15} ions/cm^2) measured at room temperature.

Figure 3.11 shows the positions of the Rayleigh SAW peaks for both samples A and B where in both cases the stiffening of the elastic constants as shown by the changes in the frequency shift of the Rayleigh SAW begin at around 120 ^{o}C. In both cases, they attain a maximum at 260 ^{o}C. It is also evident that there was more damage after implantation in sample A compared to sample A and this is also shown in figures 3.4 and 3.5.

Raman scattering studies

The Raman spectra measured on samples A and B implanted at low fluence and liquid nitrogen temperature were collected using a Jobin-Yvon LabRAM HR spectrograph with an Olympus BX41 microscope. A 600 lines/mm grating was used in single spectrograph mode. For sample C, the Raman scattering experiments were carried out using a Jobin-Yvon T64000 spectrograph. The Raman spectra were excited using the 514.5 nm laser wavelength of a Coherent argon-ion laser in all cases.

Raman experiments also confirm the structural changes in the near surface layer on the samples after ion bombardment as shown in figure 3.12. A sharp Raman peak was obtained for c-GaAs at 289 cm^{-1}. Sample A, implanted at the lower fluence shows a broadened feature with a shoulder at 280 cm^{-1}. The shoulder may be the contribution from the undamaged (100) fraction of the sample whilst the broad feature represents the LO at the X and L points, TO at the Γ , X and L points and LA from the X and L points which are typically observed in amorphised semiconductors. Sample B has a broad peak at 250 cm^{-1} and no shoulder, showing that the bombarded layer is completely amorphous.

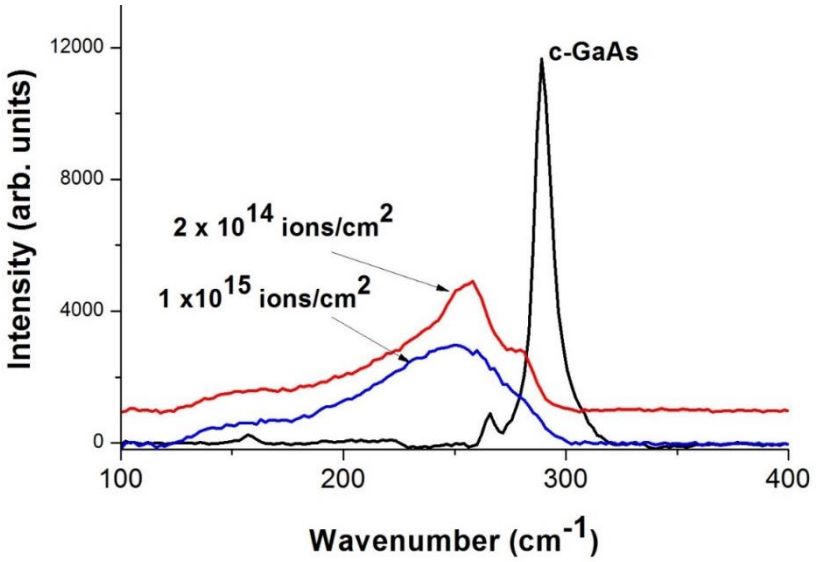

Figure 3.12: Measured Raman spectra of the crystalline GaAs sample (c-GaAs), samples A (Fluence of 2 × 10^{14}) and B (Fluence of 1 × 10^{15} ions/cm^{2}).

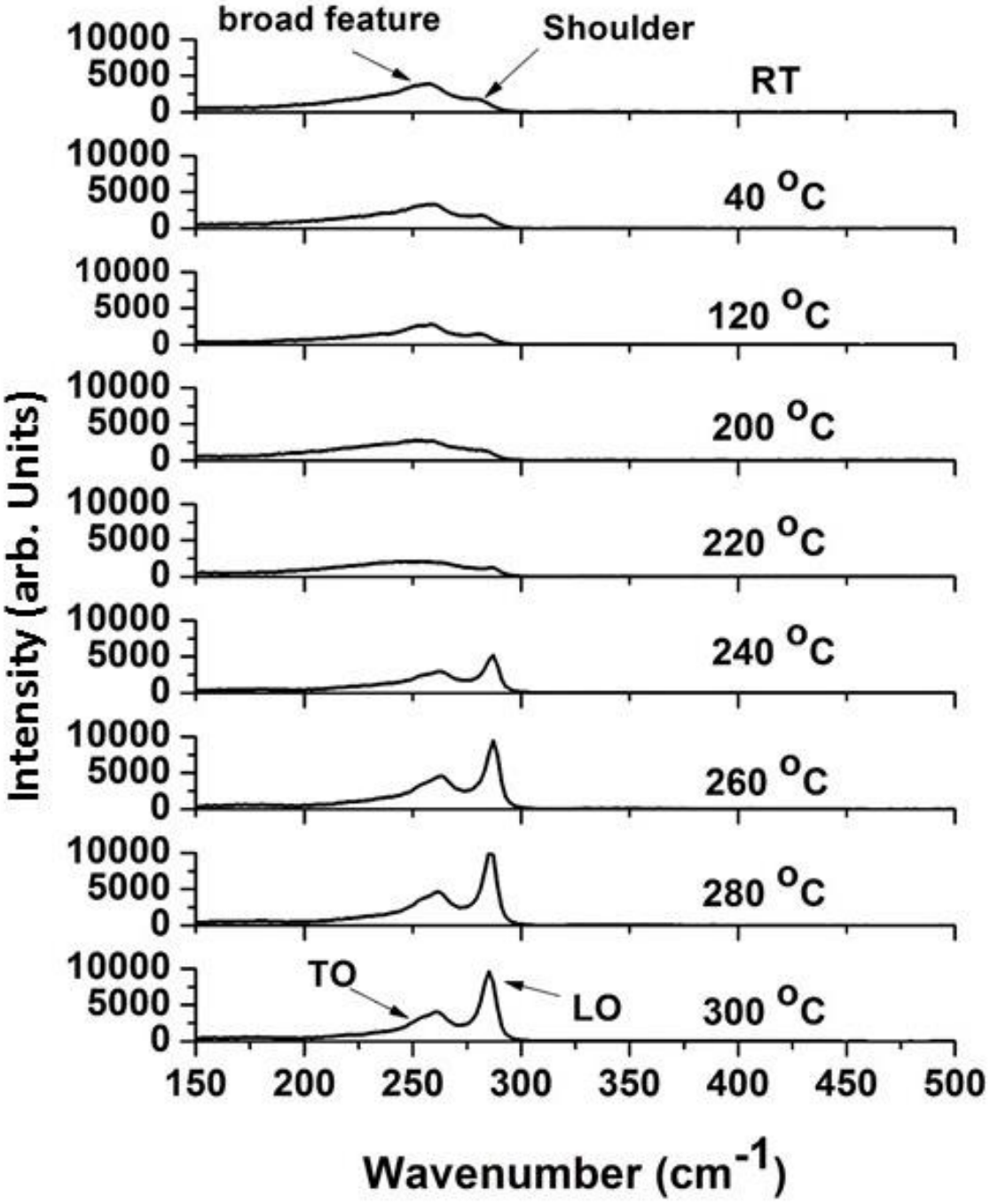

Figure 3.13: Raman spectra collected on sample A (Fluence of 2×10^{14} ions/cm^2) during isochronal annealing. The LO and TO peaks are observed at 260 cm^{-1} and 285 cm^{-1} on full recrystallization of the amorphous layer.

The Raman measurements obtained during isochronal annealing on sample A (Fluence of 2×10^{14} ions/cm^2) are shown in 3.13 and 3.14. A sharp LO peak with a higher intensity is obtained after annealing at 240 ^{o}C together with a sharp TO peak with lower intensity. This further

confirms that a larger proportion of the recrystallized region has a (100) orientation. On recrystallization the LO peak is obtained at a Raman shift of 285 cm^{-1} and the TO peak at 260 cm^{-1}. These results are in good agreement with the SBS results shown in figure 3.11 where the Rayleigh SAW attains a maximum frequency shift at 240 ^{o}C.

A plot of the Raman spectra peak intensities obtained from sample A are shown in figure 3.14. It is seen that a semi-amorphous region exists in the range from room temperature to 220 ^{0}C. Subsequently the TO and LO modes become dominant and correspond to the SBS results as shown by the changes in the frequency shift of the Rayleigh SAW in fig 3.11.

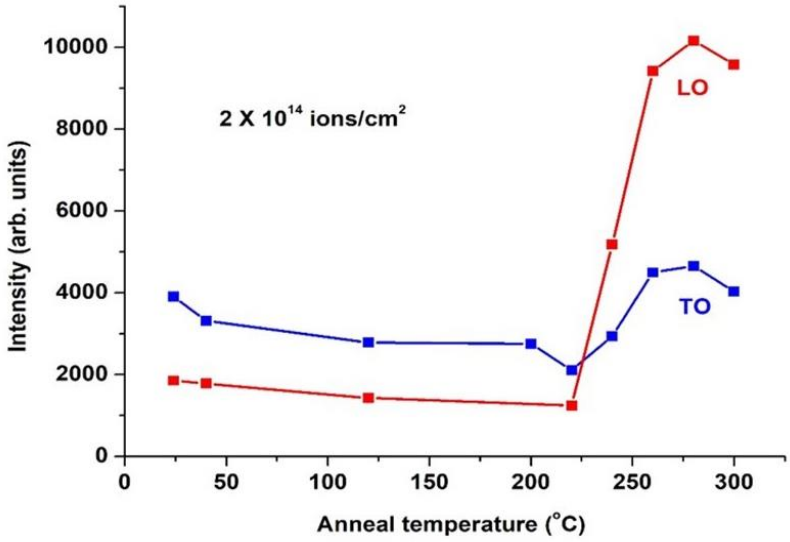

Figure 3.14: Raman spectra intensities as measured at room temperature on sample A (Fluence of 2×10^{14} ions/cm^2) after each anneal step.

A boson peak which can be observed in amorphous semiconductor materials with a maximum below 100 cm^{-1} and decreases slowly to ~1000 cm^{-1} (Desnica at al., 1997; Ivanda et al., 1994; Ivanda et al., 1995) cannot be observed in the measured Raman spectra for which the cut-off is at 100 cm^{-1}. However, it is probably superimposed in the amorphous signal at higher wavenumbers.

The Raman measurements obtained during isochronal annealing of sample B are shown in figure 3.15.

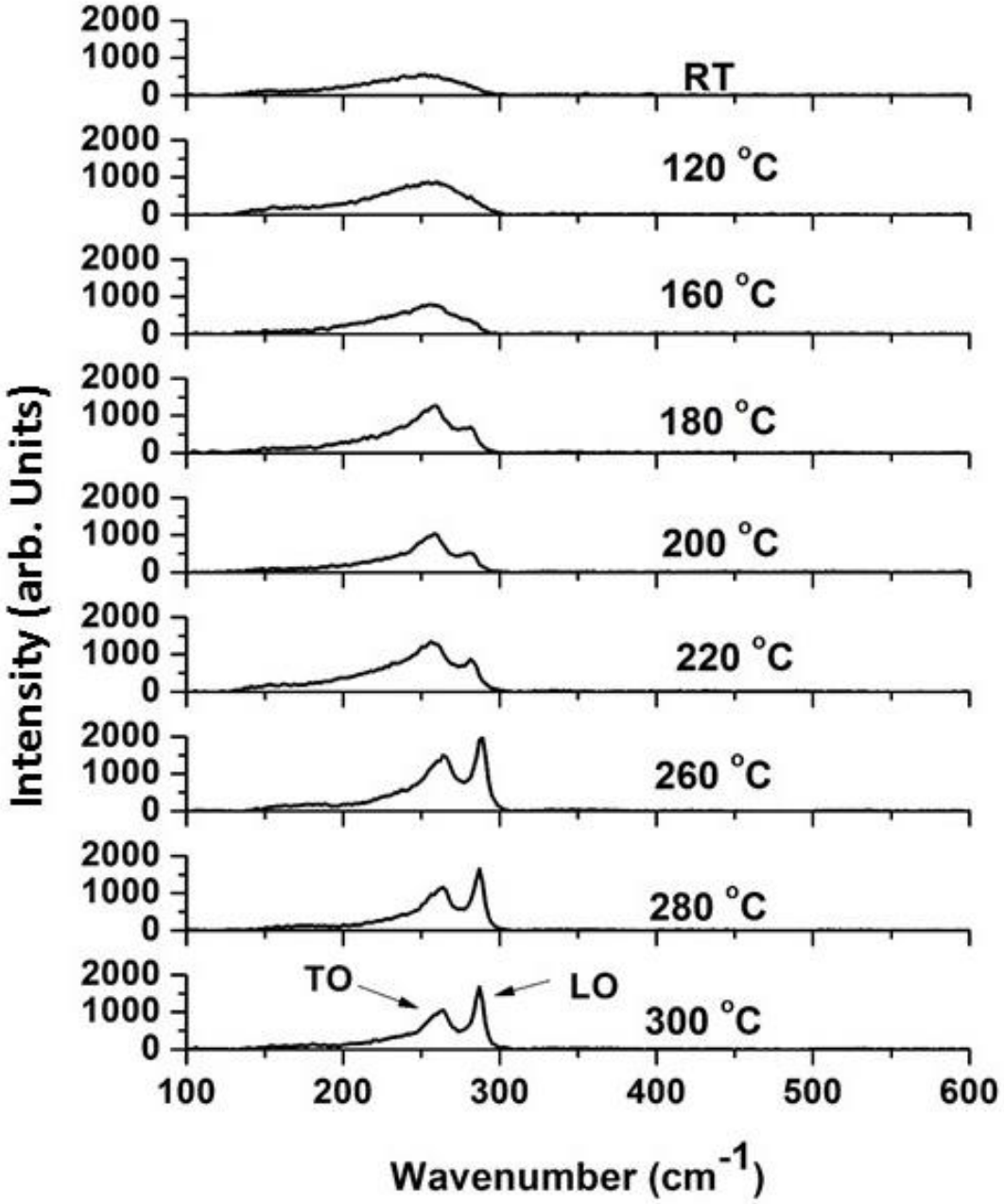

Figure 3.15. Raman spectra collected on sample B (Fluence of 1×10^{15} ions/cm^2) during isochronal annealing. The LO and TO peaks are observed at 264 cm^{-1} and 287 cm^{-1} on full recrystallization of the amorphous layer.

It can be seen from these measurements that the broad peak obtained for amorphous gallium arsenide at room temperature is obtained for anneals up to 160 ^{o}C. However, at an annealing temperature of 180 ^{o}C, two peaks attributed to the LO and TO modes are obtained. The LO peak has a lower intensity compared to the TO peak which shows that a larger fraction of the recrystallized GaAs does not have (100) orientation. This remains the case for anneal steps up

to 220 ^{o}C. After annealing at 240 ^{o}C, sharper LO and TO peaks are obtained with the LO peak having a much higher intensity. This shows that there is a larger fraction of the recrystallized material having (100) orientation. Full recrystallization is achieved at 300 ^{o}C where two sharp peaks are obtained showing that the bombarded layer had become polycrystalline. These results are highlighted in figure 3.16 which shows the Raman peak intensities after each anneal step with the anneal temperature. It can be seen from this plot that recrystallization occurs at 260 ^{o}C which is consistent with observations made with SBS for sample B in figure 3.11.

It is seen that an amorphous region exists during the temperature range from room temperature to 160 ^{0}C. Subsequently the TO and LO modes become dominant and correspond to the SBS results as shown by the changes in the frequency shift of the Rayleigh SAW.

A plot of the Raman spectra peak intensities obtained from sample B are shown in figure 3.16. It is seen that a semi-amorphous region exists in the range from room temperature to 200 ^{0}C. Subsequently the TO and LO modes become dominant and correspond to the SBS results as shown by the changes in the frequency shift of the Rayleigh SAW in fig 3.11.

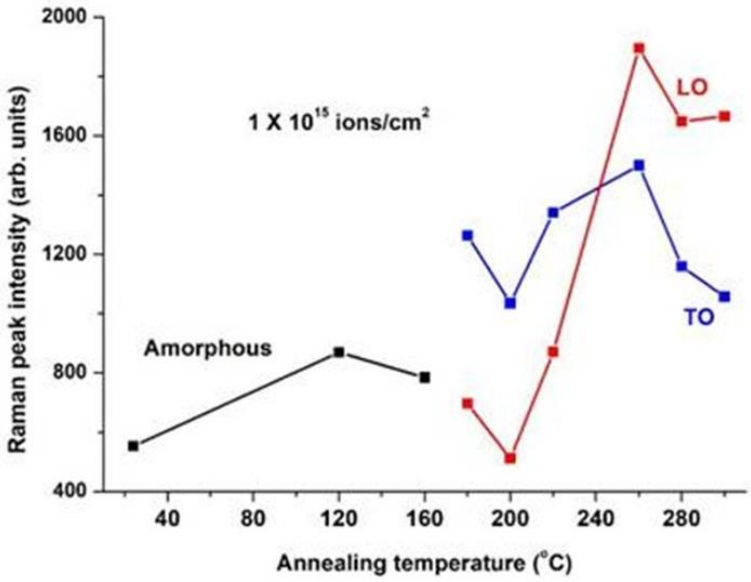

Figure 3.16: Raman spectra intensities after each anneal step as a function of the isochronal annealing temperature on the implanted GaAs sample B (Fluence of 1×10^{15} ions/cm^2) and measured at room temperature.

Similar comments regarding a boson peak as discussed above for sample A apply for sample B.

3.3 Sample C - High temperature and fluence argon ion bombardment

As discussed in section 3.1, sample C was bombarded at a temperature of approximately 50° C with an argon-ion fluence of 5 $\times 10^{16}$ ions/cm^2 and energy of 100 keV. An amorphous layer was formed with a crystalline substrate. More damage is expected in sample C because of the higher ion fluence and the recovery of the crystalline phase takes place above 600° C as reported by Desnics-Franković, 1999. For this reason, the isochronal anneal steps used for sample C are initially of 100° C and then become smaller after annealing at 400° C.

3.3.1 Surface Brillouin scattering (SBS) studies

In SBS measurements carried out after implantation on sample C, an additional peak associated with the Sezawa mode is obtained in the spectrum of the implanted sample. This provides further evidence of the presence of a thin amorphous layer on a crystalline substrate as Sezawa waves are only observed in layered materials depending on the thickness of the film (Zhang et al. 1998) and is shown in figure 3.17.

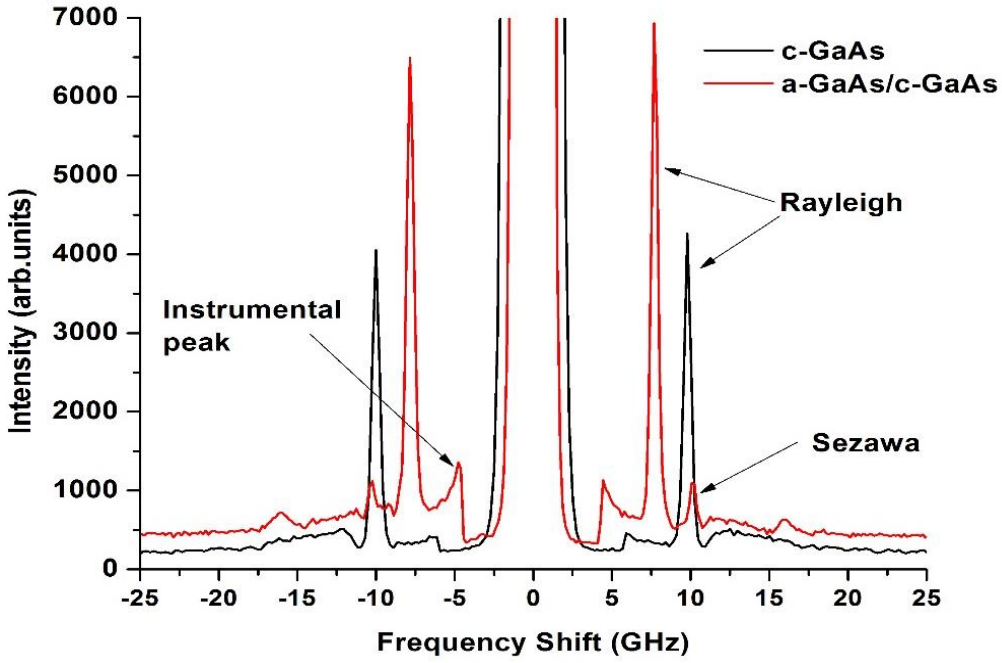

Figure 3.17: SBS spectra measured at room temperature on a sample of c-GaAs (black spectrum) and of sample C after implantation (red spectrum) showing the Stokes and anti-Stokes peaks.

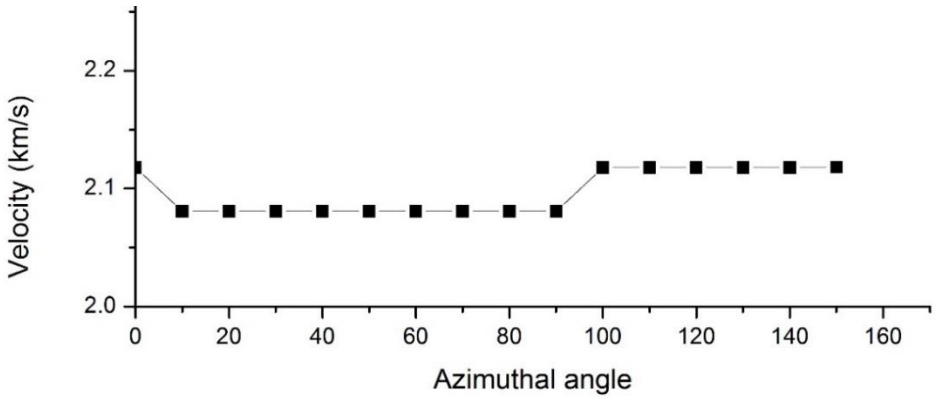

Figure 3.18. Rayleigh SAW velocities measured at room temperature on sample C after implantation whilst varying the azimuthal angle.

To determine the presence of the amorphous layer, the dispersion of the Rayleigh surface acoustic wave velocity as a function of the azimuthal angle was performed on sample C as shown in figure 3.18. It was observed that there were small and non-sinusoidal shifts in velocity between the values 2080 m/s and 2117 m/s, which gives a variation of about 1.8 % and therefore it is concluded that the sample is close to being isotropic. These results can be compared to figure 3.3 which shows the Rayleigh SAW frequency dispersion on an un-implanted anisotropic gallium arsenide sample.

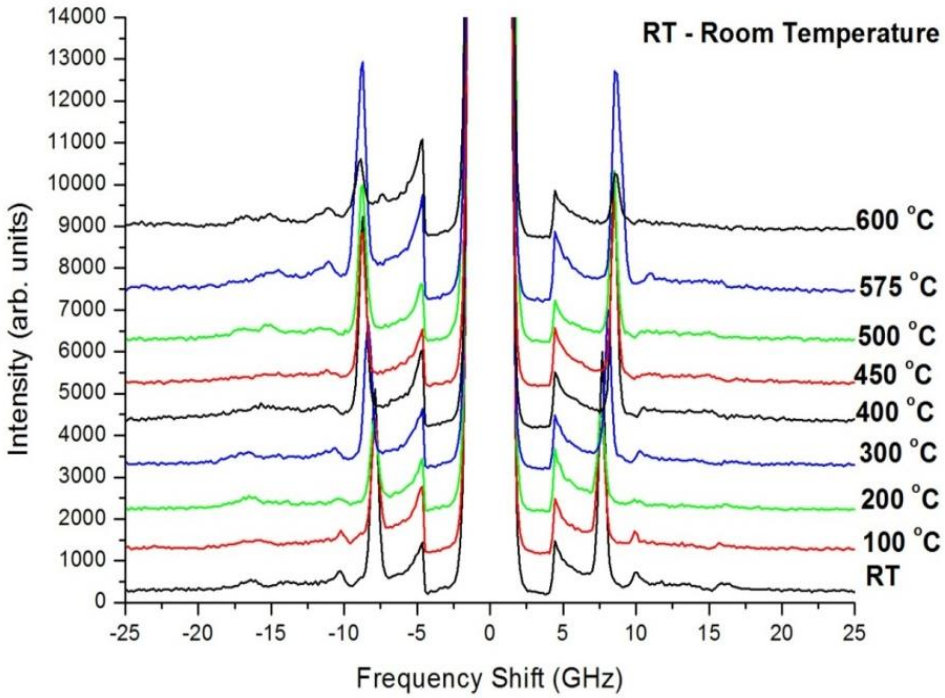

Figure 3.19. Rayleigh SAW frequency shifts measured at room temperature on sample C after each anneal step as measured at room temperature showing the Stokes and anti-Stokes peaks.

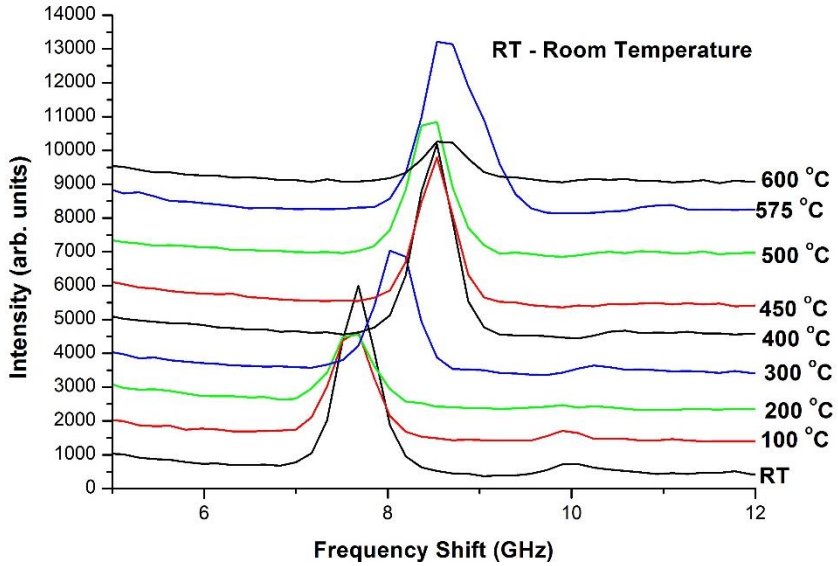

Figure 3.20. A zoomed in view of the Rayleigh SAW anti-Stokes peaks from surface Brillouin scattering measurements on sample C from figure 3.19.

SBS measurements were collected at room temperature after each isochronal annealing step on sample C as shown in figure 3.19 and 3.20 above. It can be seen that the Rayleigh SAW frequency shift starts increasing for anneals above 100 ^{o}C. This is attributed to atomic rearrangements and stiffening of the elastic constants. As mentioned in section 3.2, the intensities of the Rayleigh SAW peak vary because of different acquisition times resulting from limited measurement duration. This does not affect the peak positions.

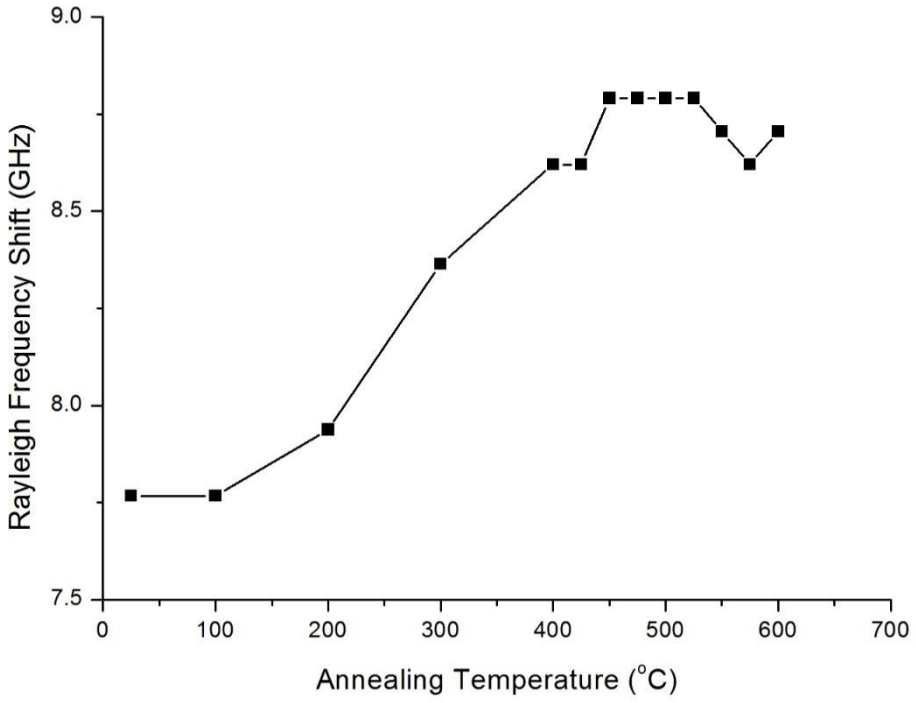

Figure 3.21. Rayleigh SAW frequency shifts measured at room temperature on sample C after each anneal.

A plot of the Rayleigh SAW frequency shifts after each anneal is shown in figure 3.21 above. The initial frequency of 7.8 GHz is obtained for the completely amorphous layer. This increases steadily during the isochronal anneals until the temperature of 450 ^{o}C is attained with a maximum value of 8.8 GHz.

A plot of the frequency shifts of the Sezawa modes is also shown in figure 3.22 below. The same trend in the frequency shifts of these peaks takes place as observed in the Rayleigh SAW peaks. They reach their maximum frequency shift of 11.1 GHz at a temperature of around 450 ^{o}C which is similar to the observation in figure 3.21 for the Rayleigh mode.

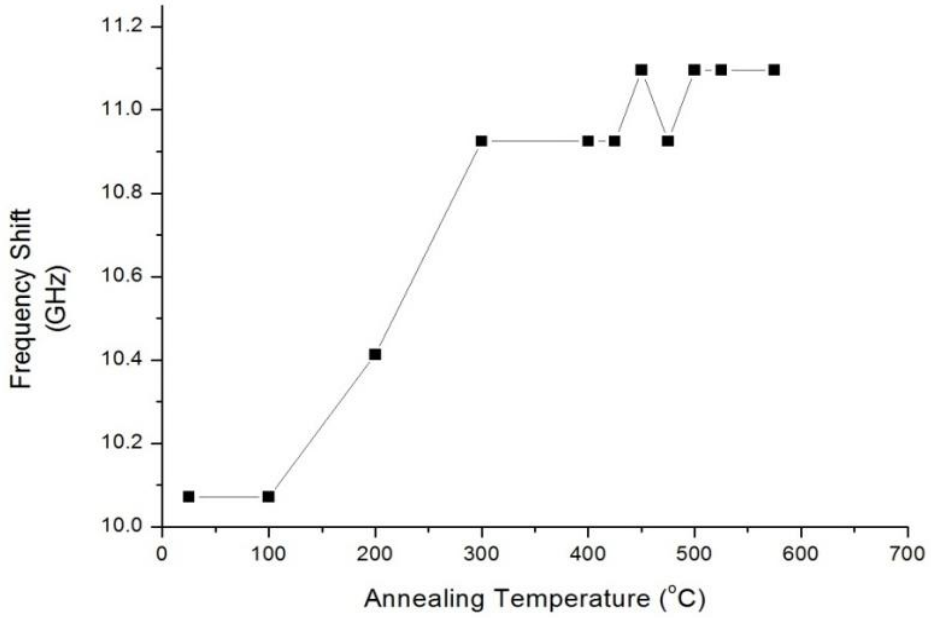

Figure 3.22. Sezawa mode frequency shifts measured at room temperature on sample C after each anneal.

3.3.2 Raman scattering studies

The spectrum of (100) oriented crystalline GaAs before ion bombardment showed the characteristic Raman peak at 293.8 cm^{-1} as seen in figure 3.23. Spectra collected after bombarding with argon ions revealed a broad peak which confirms that the top surface layer of the crystal had become amorphous. These results agree with previous reports on the Raman spectra of c-GaAs and a-GaAs/c-GaAs (Desnica et al., 1997).

Isochronal annealing of the bombarded gallium arsenide sample was then carried out using a procedure similar to that described in section 3.2 for samples A and B.

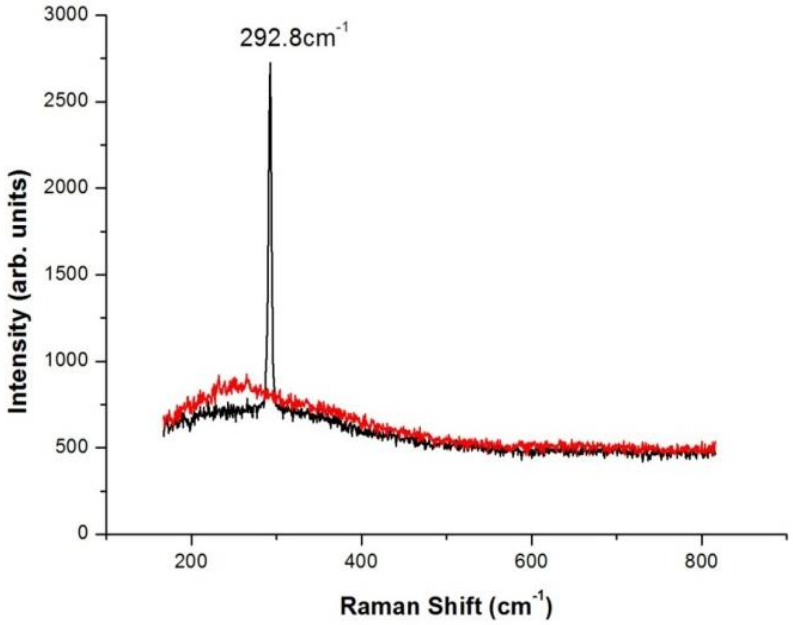

Figure 3.23. Raman spectra of c-GaAs at room temperature before ion bombardment (black spectrum) and after bombarding with argon ions showing the broad amorphous peak obtained (red spectrum) as measured at room temperature.

The Raman measurements obtained after each anneal are shown in figures 3.24a and b. The broad feature that is characteristic of amorphous GaAs is observed in all measurements carried out after each of the anneal steps below 500 ^{o}C. Peaks superimposed on the a-GaAs start to emerge after 525 ^{o}C which shows that structural changes observable by Raman spectroscopy have started. Two well defined peaks are attained at 575 ^{o}C representing the longitudinal optical mode (LO) at 283.0 cm^{-1} and the transverse optical mode (TO) at 260.7 cm^{-1} showing that a polycrystalline layer has been formed from the amorphous layer. At 625 ^{o}C, sharp Raman peaks are obtained showing full recrystallization of the amorphous layer.

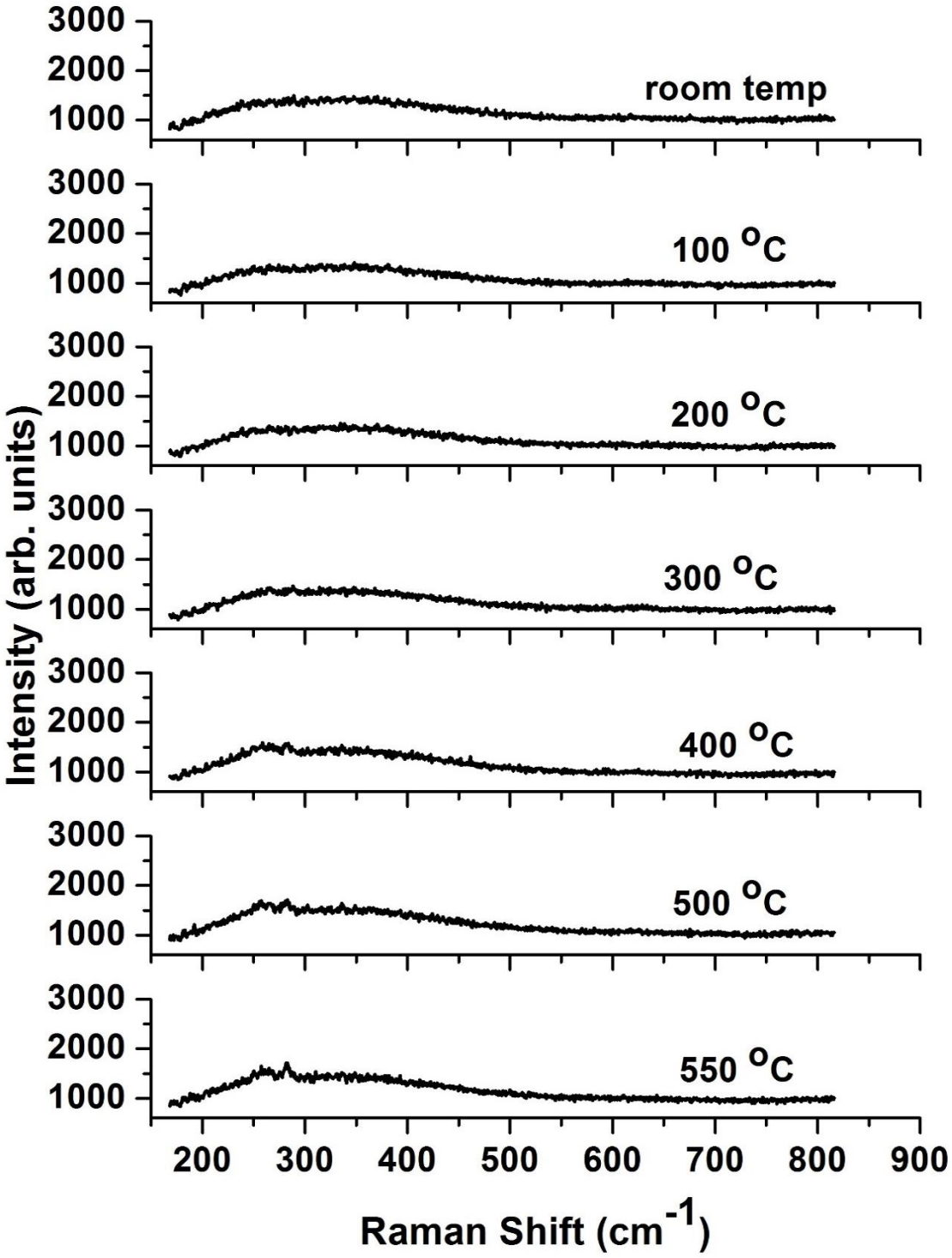

Figure 3.24(a): Raman spectra measured at room temperature on sample C of a-GaAs/c-GaAs after each anneal step. The LO and TO peaks are observed at 258.8 cm^{-1} and 283.7 cm^{-1} on full recrystallization of the amorphous layer.

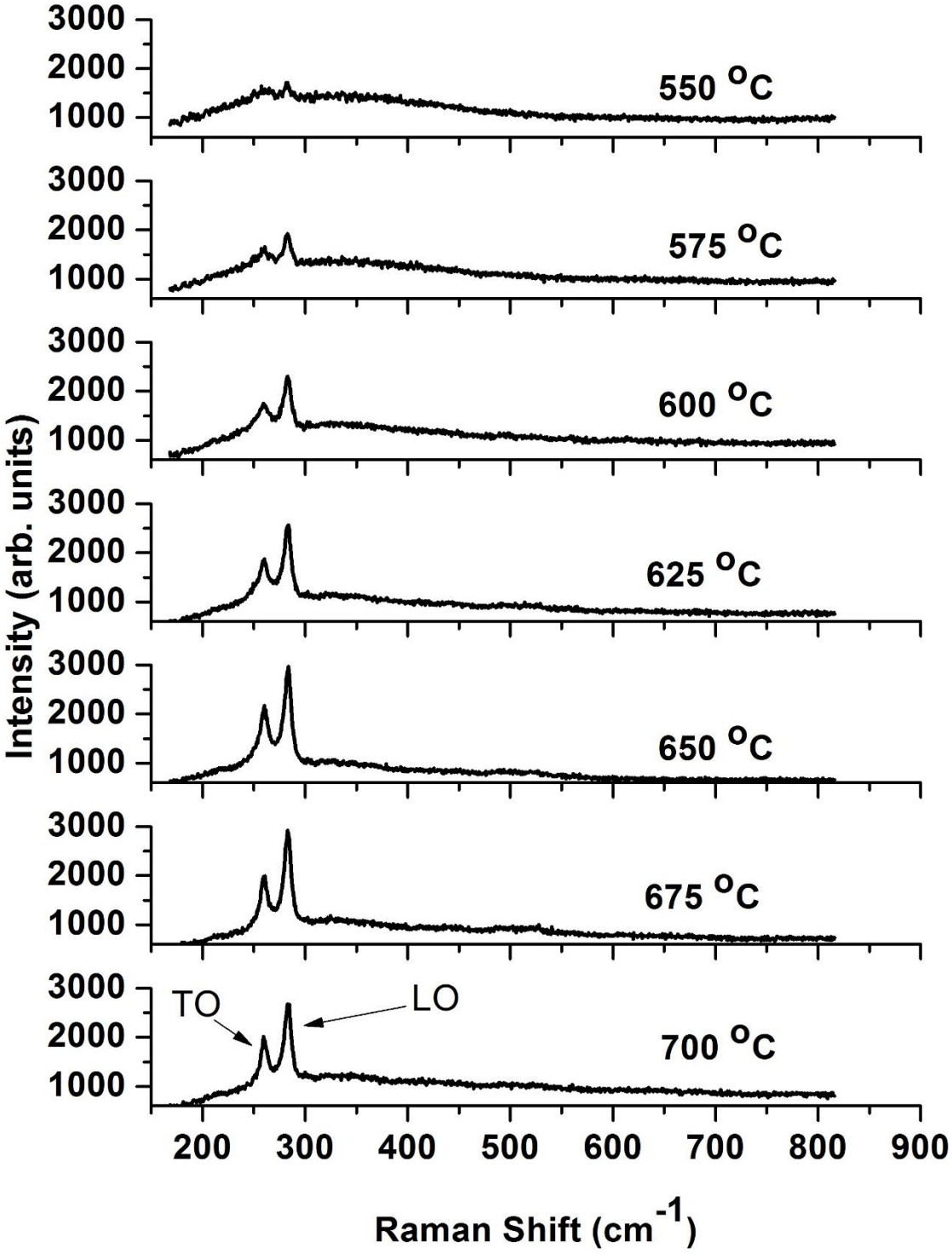

Figure 3.24(b): Raman spectra measured at room temperature on sample C of a-GaAs/c-GaAs after each anneal step. The LO and TO peaks are observed at 258.8 cm^{-1} and 283.7 cm^{-1} on full recrystallization of the amorphous layer.

Changes due to annealing in the Raman spectra have been reported starting a temperature of 160 ^{o}C where two peaks start to emerge corresponding to the LO and TO modes following implantation with Si^{+} at room temperature and at -3 ^{o}C (Desnica-Franković, 1999). By contrast

in the present work in which the implantation was carried out with argon-ions at a temperature of ~50 ^{o}C such changes are observed starting at an annealing temperature of 525 ^{o}C. The LO peak has a higher intensity compared to the TO peak showing that the recrystallized fraction is predominantly (100) oriented

Raman peak intensities after each anneal are shown in figure 3.25. It is observed that there is an amorphous layer extending from the room temperature anneal up to the anneal step at 400 ^{o}C. Subsequently the LO and TO peaks are observed as the change to the crystalline phase begins followed by full recrystallization being achieved near 650 ^{o}C.

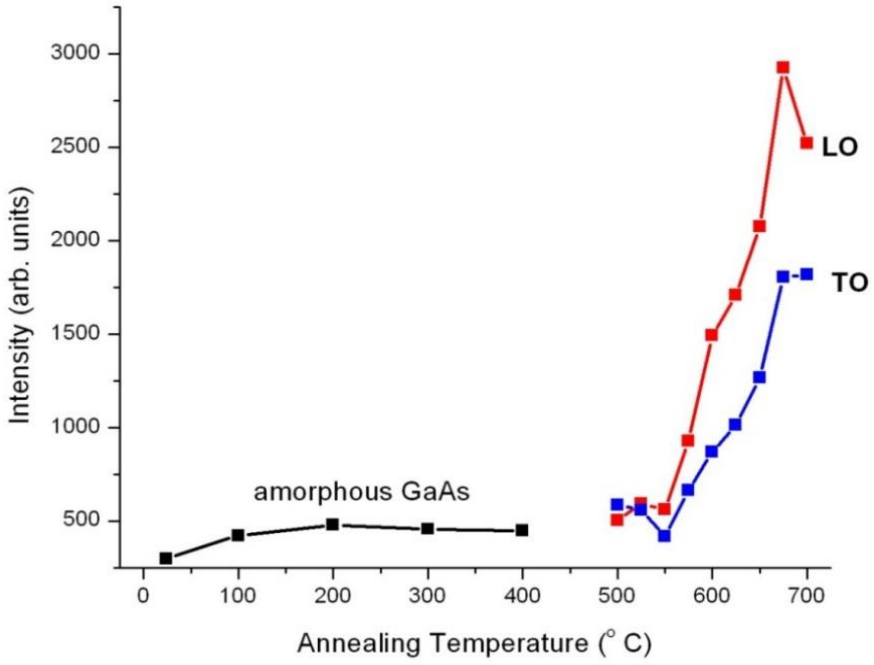

650

Figure 3.25: Raman spectra intensities as measured at room temperature on sample C of a-GaAs/c-GaAs after each anneal step.

3.5 Summary

In the present chapter the argon-ion bombardment of (100) crystalline GaAs resulted in the formation of an amorphous or near amorphous layer of GaAs on top of the undamaged c-GaAs. This is similar to having a thin film which is elastically soft above a substrate which is elastically harder. Surface Brillouin scattering and Raman spectroscopy were used to

investigate the isochronal annealing of the bombarded gallium arsenide under various conditions.

Samples A and B with lower fluences of 2×10^{14} ions/cm^2 and 1×10^{15} ions/cm^2 respectively were bombarded at liquid nitrogen temperature. The changes in the elastic constants as measured by SBS and the recrystallization processes by Raman scattering of these two samples were relatively similar in both forms of measurements. A limited degree of recrystallization begins near 180 ^{o}C for sample B and exhibits a similar degree of recrystallization in the region of 240 ^{o}C as found for sample A. Full recrystallization in both samples A and B was achieved at anneal temperatures near 300 ^{o}C.

In the case of sample C with an argon-ion fluence of 5×10^{16} ions/cm^2 and bombardment temperature near 50 ^{o}C the results are significantly different. In particular the observations made with SBS showed that the Rayleigh mode started shifting to higher frequencies at an annealing temperature just above 100 ^{o}C. This continued until a maximum annealing temperature of 450 ^{o}C. Similar results were obtained from the Sezawa mode frequency shifts

Changes in the Raman spectra obtained during annealing measurements on sample C which was implanted at the elevated temperature near 50 ^{o}C were observed starting from about 550 ^{o}C and continued to 700 ^{o}C. This is in strong contrast to the observations made with the SBS studies on sample C as described immediately above.

Thus the combination of a higher temperature and of an increased fluence of 5×10^{16} ions/cm^2 during the argon ion bombardment of sample C has produced results that are significantly different from those of samples A and B in which low temperature and lower fluences have been used. Not only have the recrystallization temperatures differed significantly in these different conditions, but so do the temperature dependences of the elastic constants. Thus it appears that during the higher temperature and increased fluence of the argon bombardment of sample C there are significant structural changes that are observed by the SBS studies prior to the recrystallization phase observed by the Raman studies. In the cases of samples A and B in which the argon bombardments take place at low temperature and are of lower fluences the structural changes observed by the SBS studies coincide more closely to the recrystallized phase observed by the Raman studies.

Chapter 4: Deposition and characterization of VC thin films on 6H-SiC and Si

Thin films can be deposited on substrates using several techniques. Some of these techniques fall under the umbrella of physical vapour deposition (PVD) while others are of the precursor based chemical vapour deposition (CVD) type. PVD includes evaporation and sputtering techniques, and in this thesis, RF magnetron sputtering has been used to grow the thin films. This is because it provides films with low surface roughness, stable stoichiometry and uniform thickness when compared to pulsed laser deposition (PLD) which was an alternative technique.

Thin film deposition by RF magnetron sputtering is a well-established technique and has received much attention (Irvine and Palmer, 1994; Liao et al., 2005). Deposition of vanadium carbide thin films has been carried by Liao et al., 2005 where they varied the RF power, argon pressure and substrate temperature. They used X-ray diffraction (XRD), Rutherford backscattering (RBS) and X-ray photoelectron spectroscopy (XPS) to determine the structure of the films, electronic structure and composition. Their results show that varying the deposition conditions such as RF power, pressure and substrate temperature causes a variation in the composition. For the three films deposited at an RF power of 100 W and at ambient substrate temperatures, the argon pressures used were 0.5 Pa, 2.0 Pa and 2.5 Pa and these resulted in compositions of $VC_{0.97}$, $VC_{0.90}$, and $VC_{0.84}$ respectively as measured using-RBS

In this chapter the deposition of sub-stoichiometric vanadium carbide thin films on (001) silicon and 6H-silicon carbide substrates is presented. This is followed by a detailed and systematic discussion of the characterisation techniques of X-ray reflectometry (XRR), Rutherford backscattering spectrometry, XRD and atomic force microscopy (AFM) used to determine structural parameters such as the film thicknesses, stoichiometry, and surface roughness. The growth of films on a silicon substrate or on the silicon carbide substrate was done under the same conditions of RF power, pressure and the target to substrate distance. The

stability of the deposition conditions ensures the reproducibility of the results of the characterization techniques on films deposited on either substrate. Aside for the film substrate adhesion it is expected that the film microstructure remains independent of the substrate used.

4.1 Deposition of sub-stoichiometric VC thin films by RF magnetron sputtering

A comprehensive description of RF magnetron sputtering has been given by (Ohring, 1992) and the present description follows this report closely. Using this technique, thin films of vanadium carbide were deposited on (001) silicon and 6H-silicon carbide substrates using RF magnetron sputtering. A schematic of the experimental arrangement is shown in figure 4.1 below.

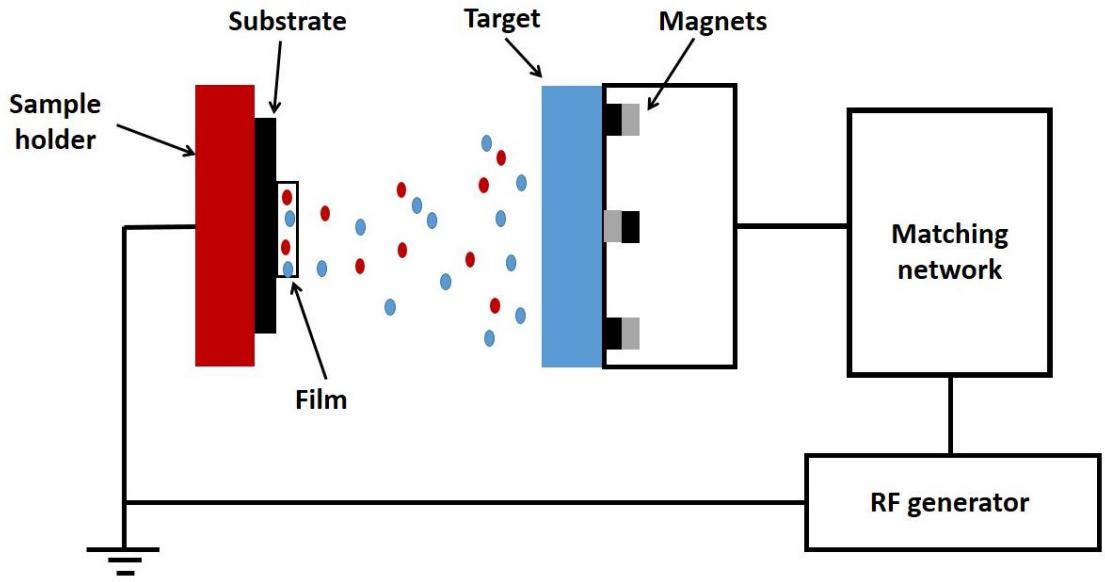

Figure 4.1 Schematic of RF magnetron deposition of thin film.

This was done by placing a target of VC with 99.9 % purity 60 mm away from the substrate on the cathode of the RF supply in a high vacuum chamber where a system of rotary and turbo molecular pumps created a base pressure of the order of 10^{-6} mbar. Argon gas was then introduced in the chamber at a flow-rate of 13 sccm and the RF power increased to ignite a self-sustaining plasma. The Argon ions in the plasma were accelerated to the cathode to collide with the target material through a knock-on effect. This is similar to ion bombardment where a number of processes can occur depending on the mass, flux and energy of the bombarding

ions. Figure 4.2 shows the various effects of ion bombardment on the surface region such as ejection of secondary electrons, sputter ejection of surface atoms by momentum transfer through collision cascades, enhanced surface mobilities of atoms on the surface, creation of lattice defects and re-deposition of ejected atoms or ions after collisions in the gas phase, by ionization and acceleration back to the surface (Mattox, 1989). Secondary electrons accelerate away from the target or cathode and assist in sustaining the plasma in the dc diode plasma configuration (Mattox, 1989).

The species in plasma colliding with the target can be implanted into the target, and if the target is made up of a crystalline material then lattice defects may also arise from collision cascades. Channelling effects can also be observed.

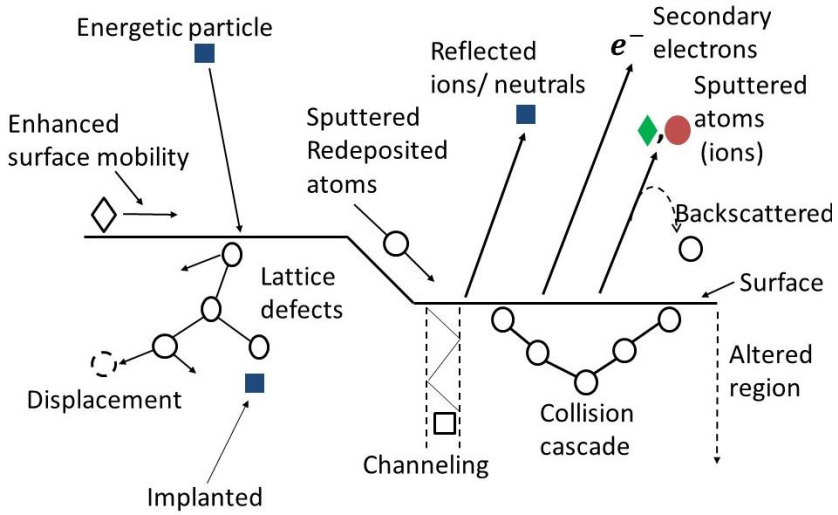

Figure 4.2 Schematic depiction of the energetic bombardment effects on surfaces and growing films (Mattox, 1989).

This transfer of momentum causes the ejection of carbon and vanadium ad-atoms or molecules which will then travel through the plasma and condense as a film onto the substrate. The ionized argon gas is confined to the active zone near the target by a magnetic field of flux density 0.3 T which is introduced by the unbalanced magnets to prevent sputtering from the substrate. However, in order to remove the native oxide layer on the Si substrate before film deposition, the substrates were biased negatively at – 300 V and at a low RF power of ~ 40 W for 5 minutes. This ensures sputter etching of the oxide layer and the substrate surface up to 5μm in depth and enhances film adhesion by changing the surface chemistry, and generating a

microscopically rough surface. It also increases nucleation density by forming nucleation sites and increases the surface mobility of atoms (Mittal,1978; Mattox,1989).

Film deposition was carried out at room temperature at a working gas pressure of 10^{-3} mbar. Seven films of vanadium carbide of varied thicknesses were grown on silicon by changing the deposition time for each sample. The deposition times of the films were 10, 20, 30, 40, 50, 60 and 80 minutes, respectively. The same was done for films grown on the 6H- SiC polymorph. An RF power of 100 W was used in each case. For simplicity in the subsequent sections and chapters the sub-stoichiometric vanadium carbide films ($V_{0.2}C_{0.8}$) will be referred as VC thin films.)

Residual compressive and tensile stresses arise in deposited films. Compressive stresses may emanate from depositions at low pressures using high RF powers due to the recoil implantation of surface atoms (Cuthrell et al., 1988; Thornton et al., 1979). The film may buckle from the surface, peel from the substrate when the residual stresses are sufficiently high (Mattox, 1989).

4.2 X-ray reflectometry measurements

Three extra films of VC were grown on (001) Si substrates at 2.5, 5.0, and 7.5 minutes in order to vary the film thickness and consequently determine the deposition rate. This deposition rate was used to extract the thicknesses of samples deposited for longer periods due to the linearity between film thickness and deposition time over a fixed RF sputter power. This observation holds only for targets without deeper sputter grooves (<5% of target thickness) as in this case the deposition rate is constant in time at fixed deposition power. X-ray reflectivity (XRR) measurements were carried out on the deposited films to determine their density and film thickness. This is a well-established method which allows the determination of film thickness, surface roughness and mass density (Chason and Mayer, 1997; Feranchuk et al., 2003; Krumrey et al., 2004; Yasaka, 2010). These results corroborate those for films deposited on SiC substrates since similar deposition conditions were used.

In XRR, oscillations which are called Kiessig fringes are observed when a reflected beam of X-rays from the surface layer interferes with the one reflected at the interface between the substrate and the film. These oscillation occur at incidence angles greater than the critical angle, θ_c , for total external reflection as the X-rays are able to penetrate the medium. For most

materials, $\theta_c < 0.3^o$. At incidence angles lower than the critical angle for total external reflection, the incident X-rays are totally reflected into air since its refractive index ($n_{air} = 1$ for X-rays) is larger than that of the film (as $n < 1$, for all media in these wavelength regimes). The density is thus directly related to the critical angle by the expression,

$$\theta_c \propto \sqrt{\rho}.$$

The amplitude of the fringes is related to the roughness of the surface or the interface (Gibaud and Hazra, 2000; Colombi et al., 2008). An example of a typical spectrum observed for measurements on thin supported films is shown in figure 4.3 below. The refractive index is given by the expression,

$$n = 1 - \delta - i\beta,$$

where δ is the dispersion and β is the absorption of the material (Gibaud and Hazra, 2000). The electron density is given by the expression,

$$n_e = Z \cdot n_{Atom},$$

where z is the number of electrons per atom.

It can then be shown by considering the relation of these parameters to the electron density, ρ, and the linear absorption coefficient, μ, that, ρ, at grazing incidence is given by the expression,

$$\frac{\theta_c^2}{\rho} = \frac{r_e \lambda^2}{\pi}, \qquad 4.1$$

where θ_c is the critical angle, λ is the wavelength of the X-ray beam and r_e is the classical electron radius, (Gibaud and Hazra, 2000). Film thickness, t, is found from the relation,

$$t = \frac{\lambda}{2\left(\theta_m^2 - \theta_{cL}^2\right)^{1/2}} m, \qquad 4.2$$

where m is the order of diffraction, θ_m is the incidence angle at which the interference maximum of order m occurs, and θ_{cL} is the critical angle of the layer (Colombi et al., 2008).

The discussion of the surface roughness developed here follows closely the approach (Gibaud and Hazra, 2000). A rough surface reduces the reflected intensity of the X-ray beam. The roughness, σ, is given by the expression,

$$\sigma^2 = \langle z(x,y) - \bar{z}^2 \rangle = \int P(z)(z(x,y) - \bar{z}^2)dz,$$

where $P(z)$ are the moments of the distribution in z; $\bar{z}$ is the mean altitude and $z(x,y)$ is the altitude. The introduction of a correlation function $g(X,Y)$ which correlates the two points at different heights on the surface $z(x,y)$ and $z(x' = x + X,\ y' = y + Y)$ and assuming that,

$$\langle z^2(x,y) \rangle = \langle z^2(x',y') \rangle = \sigma^2,$$

leads to,

$$g(X,Y) = 2\sigma^2 - 2\langle z(x,y)z(x',y') \rangle.$$

Surface roughness reduces specular reflectivity by a Debye-Waller factor and when the correlation length of the height fluctuations is not very large then,

$$R^{rough}(q_z) = R^{flat}(q_z)e^{-q_{z,0}q_{z,1}\sigma^2},$$

where $q_{z,0}$ and $q_{z,1}$ are the wavevector transfers in air and in the material.

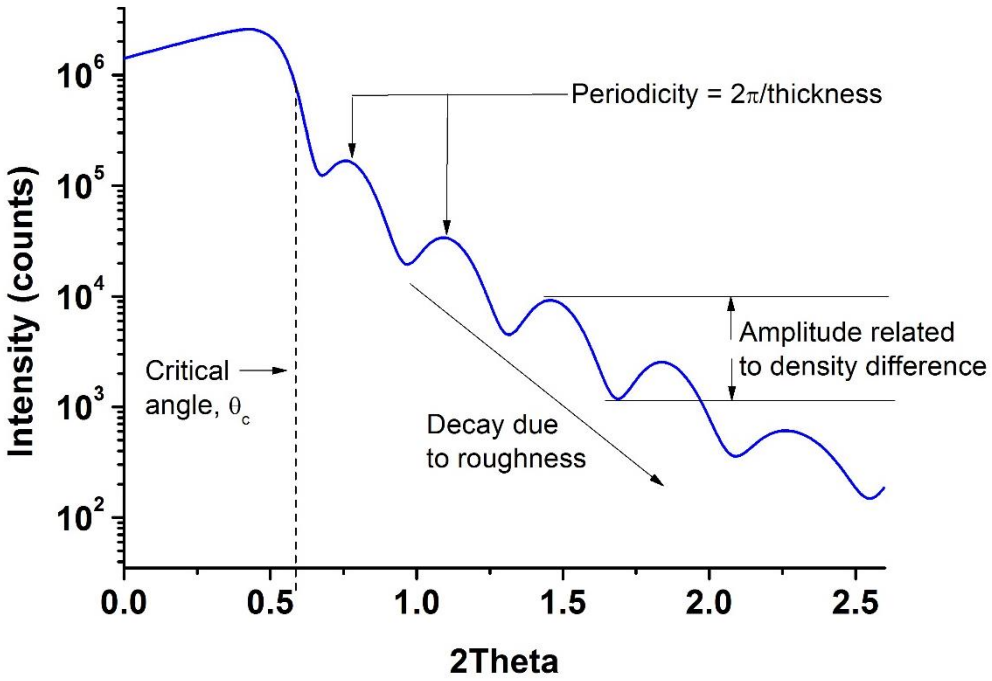

Figure 4.3 Example of typical XRR spectra showing the fringes obtained (Chason and Mayer, 1997).

The experiments were carried out with a Bruker AXS Discover 8 using a Cu-Kα X-ray beam. The spectra obtained from the measurements was fitted using LEPTOS, being proprietary software provided by Bruker, in order to extract the film thickness, electron density and the roughness of the films. The results obtained from the fitting procedure shown in figures 4.4 and 4.5 show that good agreement is obtained between experimental data (raw data) and the simulated curve when a thin layer of SiO_2 sandwiched between the VC film and the substrate is included. This is because these films were not sputter etched during deposition as this would have interfered with the roughness at the substrate-film interface thereby increasing complexity in the observed XRR spectra. The figure also shows that the position of the critical angle for total external reflection by X-rays is nearly the same. However, the periodicity of the oscillations for films deposited for 5 minutes is twice that of those deposited for 2.5 minutes.

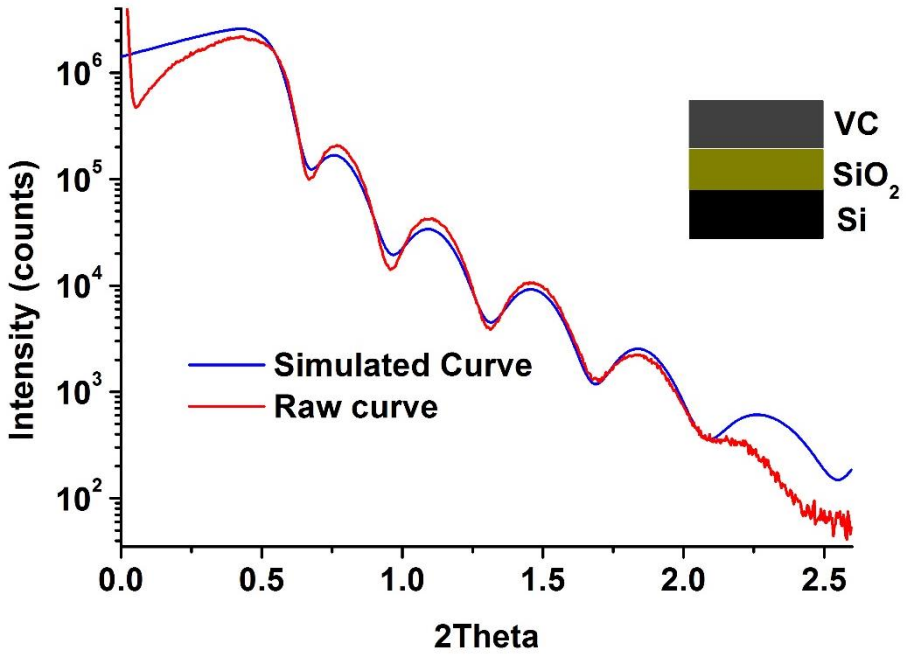

Figure 4.4 XRR pattern using LEPTOS (blue) and measured spectra (red) for VC thin film deposited for 2.5 minutes on a Si substrate. The model has assumed the properties of a layer stack of VC/SiO_2/Si in that order.

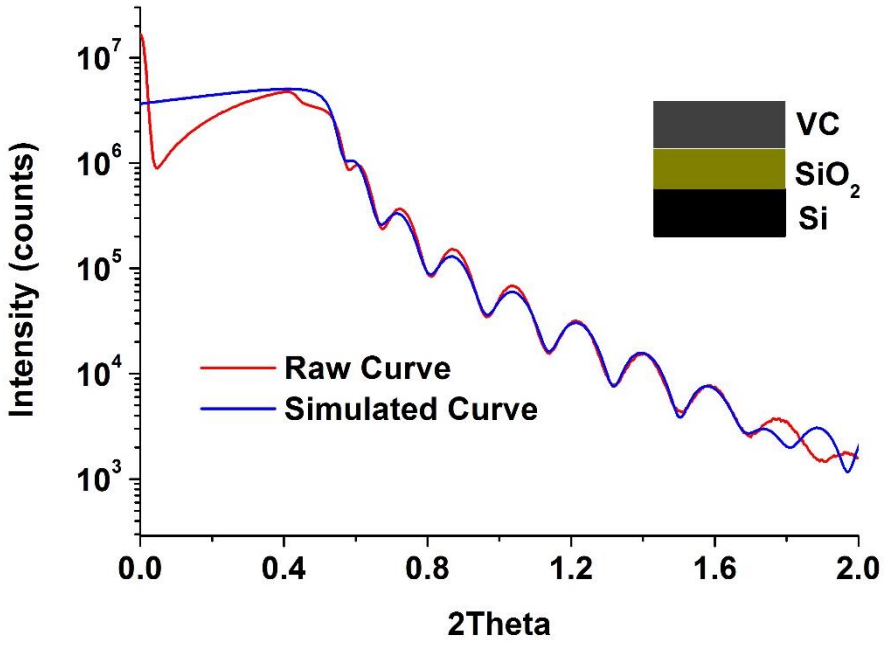

Figure 4.5 XRR pattern comprising of the simulated (blue) and measured curve (red) for VC thin film deposited for 5 minutes on a Si substrate.

Deposition Time (minutes)	Film Thickness (nm)	Roughness (nm)	Density (g cm^{-3})
2.5	21.8	1.3	3.6
5.0	43.3	2.1	3.6
7.5	64.2	1.6	3.1

Table 4.1. Parameters obtained from X-ray reflectometry measurements and simulations performed using LEPTOS on VC/Si deposited at 100 W using RF sputtering.

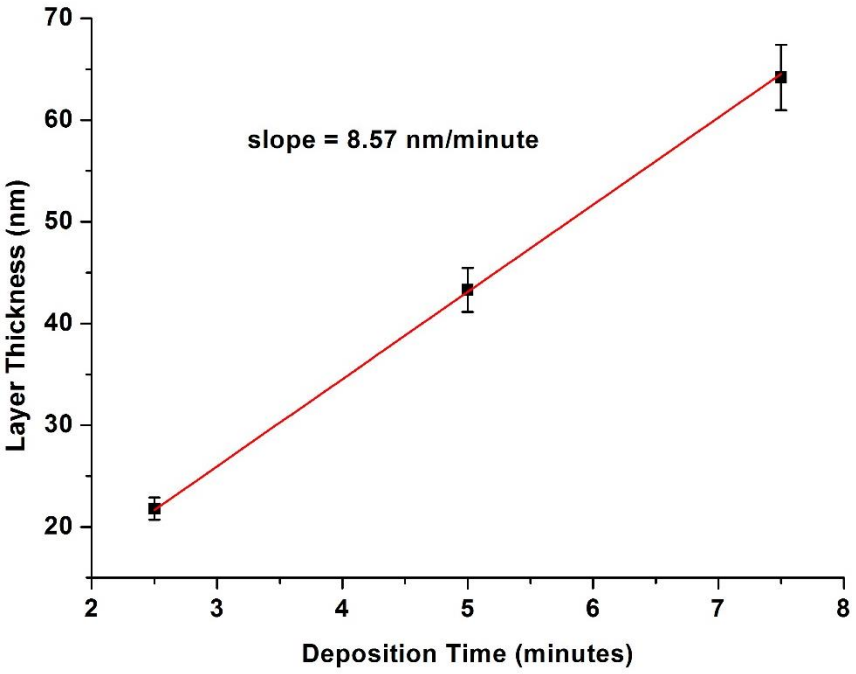

Figure 4.6 Plot of film thickness obtained from XRR against deposition time for VC thin films grown for 2.5, 5 and 7.5 minutes on a Si substrate. The linearity of the curve permits the extrapolation of film thickness produced at longer deposition times.

A plot of the film thicknesses against deposition time, figure 4.6, gives a linear fit with a slope of 8.57 nm/minute. From this result, the thicknesses of the films deposited for longer periods can be determined as shown in table 4.2 below.

Deposition Time (minutes)	Film Thickness (nm)
10	86
20	171
30	257
40	343
50	429
60	514
90	771

Table 4.2. Film thicknesses and deposition times of VC/Si determined from XRR measurements.

4.3 Structure determination by X-ray diffraction

Depending on the deposition conditions diverse forms of structural phases in thin film can be observed. These structural phases are critical to the dynamics of the surface acoustic waves. Thus it is imperative to establish whether the deposited films were either textured or amorphous, or polycrystalline or even epitaxially grown on the substrate. This information is useful since the determination of the elastic stiffnesses of the film is dependent on the nature of isotropy or anisotropy in the crystallographic directions in the films. The explicit elaboration of this point is presented in the results of the surface Brillouin scattering in chapter 5. Grazing incidence X-ray diffraction (GIXRD) measurements were carried out on VC/SiC in order to determine the phase of VC thin films under the deposition conditions. This was done in Seemann Bohlin geometry and the resulting spectra in figure 4.7 shows that indeed the deposited films are amorphous (isotropic) from the absence of distinct Bragg reflexions. For a crystalline VC thin film the expected peaks are at 2θ values of around 37°, 43°, 63°, 75°, 79°, 95°, 107°, 111°, 129°, and 149° for cubic vanadium carbide (Berndt et al., 1993).

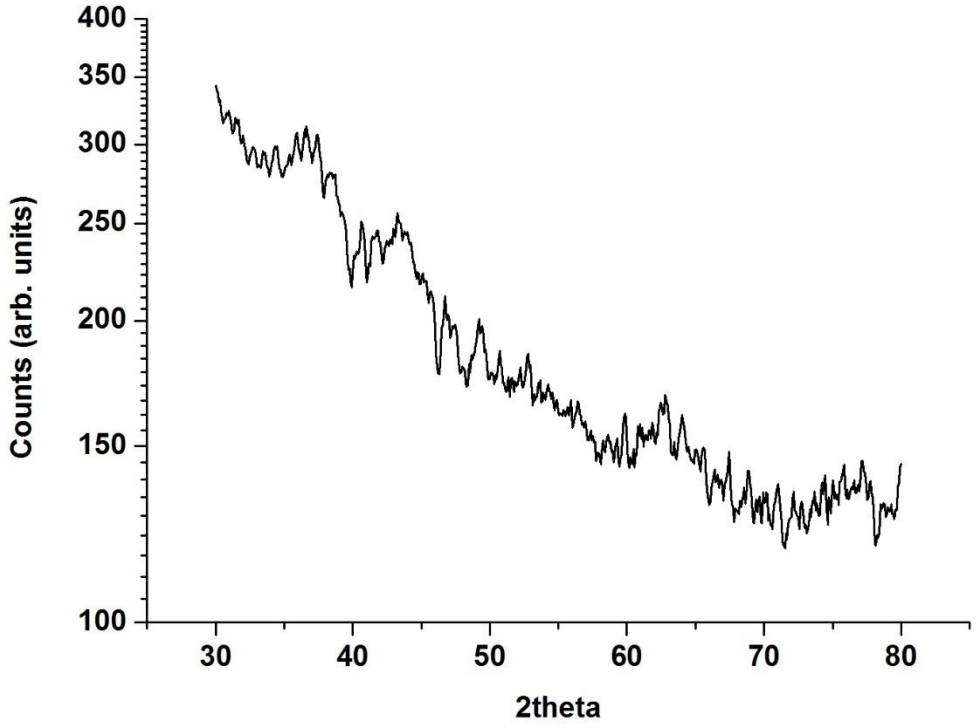

Figure 4.7 Plot of X-ray diffraction spectra obtained from the 171.4 nm thin film of VC deposited on Si.

4.4 Rutherford backscattering measurements

Rutherford backscattering spectroscopy (RBS) was carried out in order to determine the stoichiometry of the deposited films. The experiments were carried out at the University of Pretoria using a model AN-2000 Van de Graff accelerator, and at iThemba LABS, Gauteng using an HVEC Tandem van der Graff accelerator. This was performed on the films deposited on Si but because the deposition conditions of argon pressure, RF power of 100 W and ambient substrate temperature on the SiC substrate were exactly the same, the results should also hold. Thin films of VC on Si were bombarded with ${}_2^4\mathrm{He}^{2+}$ particles at an incident energy of 1.6 MeV and the energy of the backscattered helium ions measured with the geometry $\theta = 9.0, \phi = 15.0, \text{and } \varphi = 0.0$. If the energy of the incident ${}_2^4\mathrm{He}^{2+}$ particle is E_0, while that of the backscattered particle is E_1, then the kinematic factor k is defined as,

$$k = \frac{E_1}{E_0} = \left[\frac{\left[M_2^2 - M_1^2 \sin^2\theta\right]^{1/2} + M_1 \cos\theta}{M_2 + M_1}\right]^2 \qquad 4.3$$

where M_1 and M_2 are the masses of the incident ion and target atom respectively. θ is the scattering angle and in this case, the measurements were collected using the IBM geometry, see figure 4.8, where for an incident angle α, exit beam β,

$$\alpha + \beta + \theta = 180^o. \qquad 4.4$$

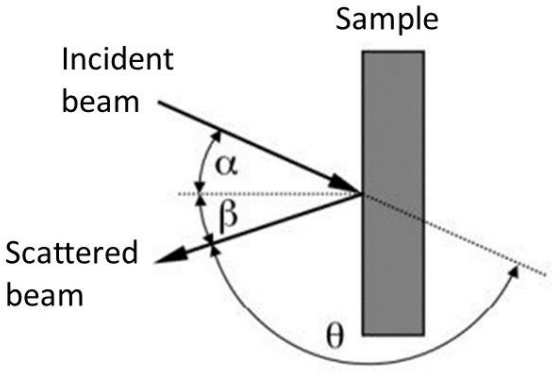

Figure 4.8. IBM geometry with incident angle α, exit angle β and scattering angle θ (After Mayer, 2003).

In the present case, there are two target elements and so for alpha particles scattered from a vanadium and carbon atom,

$$\Delta E_1 = E_0 \frac{dK}{dM_2} \Delta M_2 \qquad 4.5$$

with ΔE_1 as the energy difference when an alpha particle is scattered from both V and C and ΔM_2 is the mass difference (Wang and Nastasi, 2010).

The energy lost by the backscattered alpha particles gives an indication of the depth scale and is dependent on whether the scattering occurs at the surface or below the surface of the film. Following Leavitt et al. in Wang and Nastasi, 2010, the energy of a particle backscattered from the surface will be given by,

$$E_1 = k.E_0. \qquad 4.6$$

For a particle scattered at a depth x in the film, it loses energy ΔE_{in} before and ΔE_{out} after collision. It can be shown that the energy detected is then given by the expression,

$$E_1 \approx kE_0 - \left[\left(\frac{dE}{dx}\right)_{in}.k + \left(\frac{dE}{dx}\right)_{out}.\frac{1}{\cos\theta}\right].x. \qquad 4.7$$

The mean differential cross section, $\sigma(\theta, E)$, for scattering of beam particles of incident energy E_0 by target particles in a thin film is defined by,

$$\sigma(\theta, E) = \left(\frac{1}{Nt}\right)\frac{dQ(E)}{Q}\frac{1}{\Omega(\theta)} \qquad 4.8$$

where Nt is the number of target atoms per unit area perpendicular to the beam and $dQ(E)/Q$ is the fraction of the incident particles scattered into the small solid angle $\Omega(\theta)$ centred at deflection angle θ (Wang and Nastasi, 2010).

An approximation for the Rutherford cross section for large backscattering angles and $(M_1/M_2 \ll 1)$ is given by,

$$\sigma_R(E, \theta) \approx 0.02073\left(\frac{Z_1 Z_2}{4E}\right)^2\left[sin^{-4}\left(\frac{\theta}{2}\right)\right] - 2\left(\frac{M_1}{M_2}\right)^2, \qquad 4.8$$

where E in in MeV and σ_R is in $10^{-24}\ cm^2$ (Chu et al., 1978).

Figure 4.9 shows the RBS spectrum obtained from a measurement on a VC thin film deposited on etched Si at 100 W for 5 minutes. The RBS spectrum is an energy spectrum which is a convolution of the stoichiometry and film thickness in a complex function. The energy position in the spectrum represent the energy of helium ions that have been backscattered from an element in the outermost layer (VC). The red fitted curve was obtained using Rutherford universal manipulation program (RUMP) and gives a thickness of 45 nm which is in good agreement with the measurement of 43.3 nm obtained using XRR in section 4.2. The composition obtained for the fitting is 0.18 for vanadium, 0.82 of carbon with 0.02 of Fe.

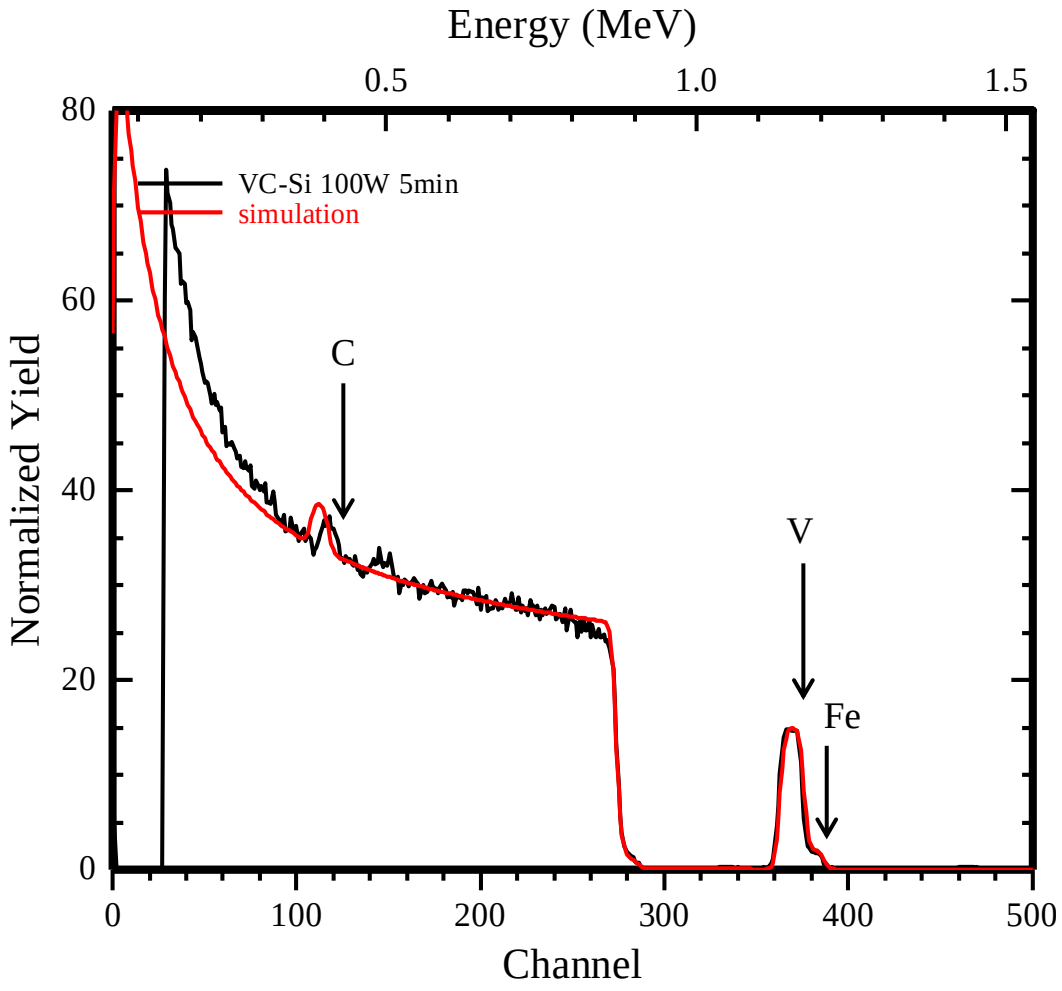

Figure 4.9 Plot of RBS spectrum obtained from VC thin film deposited on Si at 100 W for 5 minutes and the fitted curve (red).

The RBS spectra obtained from the VC thin film deposited on Si at 100 W for 15 minutes shown in figure 4.10 gives a thickness of 115 nm which is not in very good agreement with the expected value of 125.6 nm from XRR. The composition obtained for the fitting is 0.22 for vanadium, 0.75 of carbon with 0.025 of Fe.

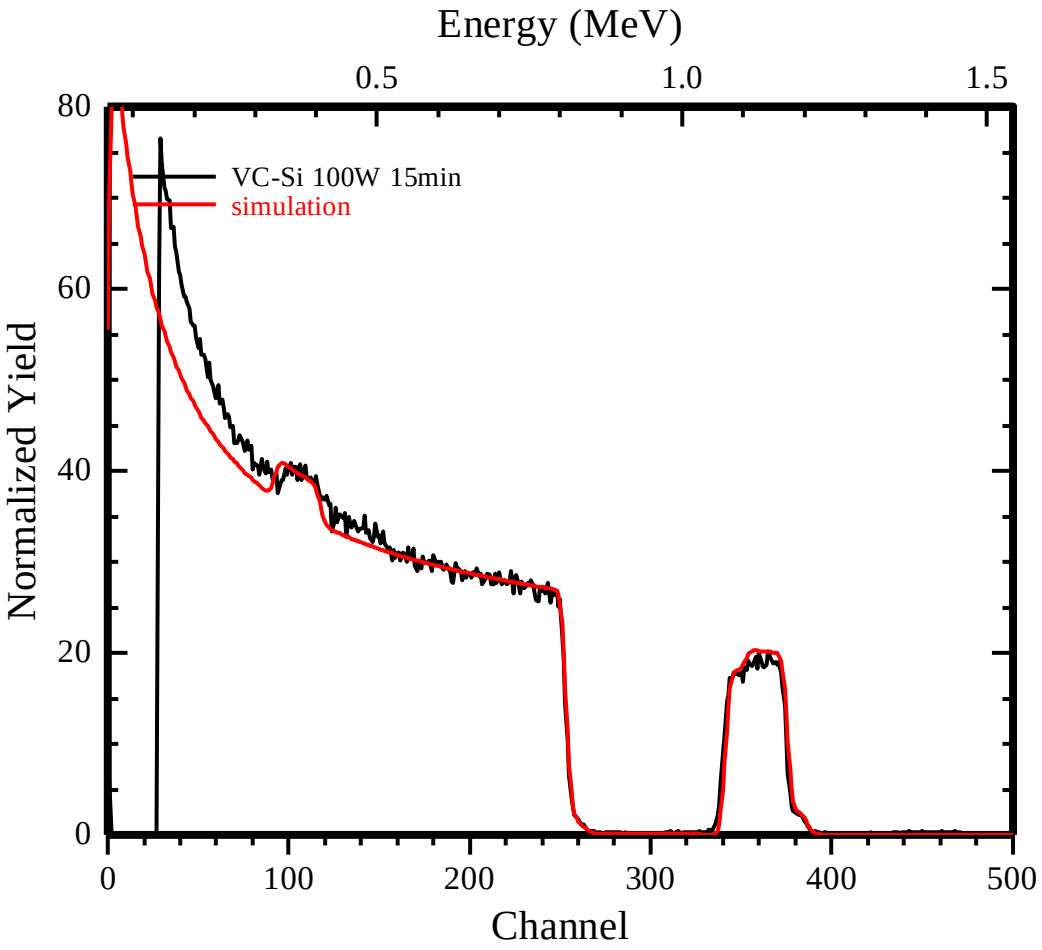

Figure 4.10 Plot of RBS spectra obtained from VC thin film deposited on Si at 100 W for 15 minutes and the fitted curve (red).

The RBS spectra obtained from the VC thin film deposited on Si at 100 W for 25 minutes shown in figure 4.11 gives a thickness of 190 nm which is not in very good agreement with the expected value of about 214.3 nm from XRR. The composition obtained for the fitting is 0.22 for vanadium, 0.75 of carbon with 0.025 of Fe. The disparity in the measurement of film thickness in this technique arises from the non-linearity arising in changes in the beam energy for thicker samples. Therefore the spectrometer gain which assumes linearity for scattering at the sample surface cannot be ignored.

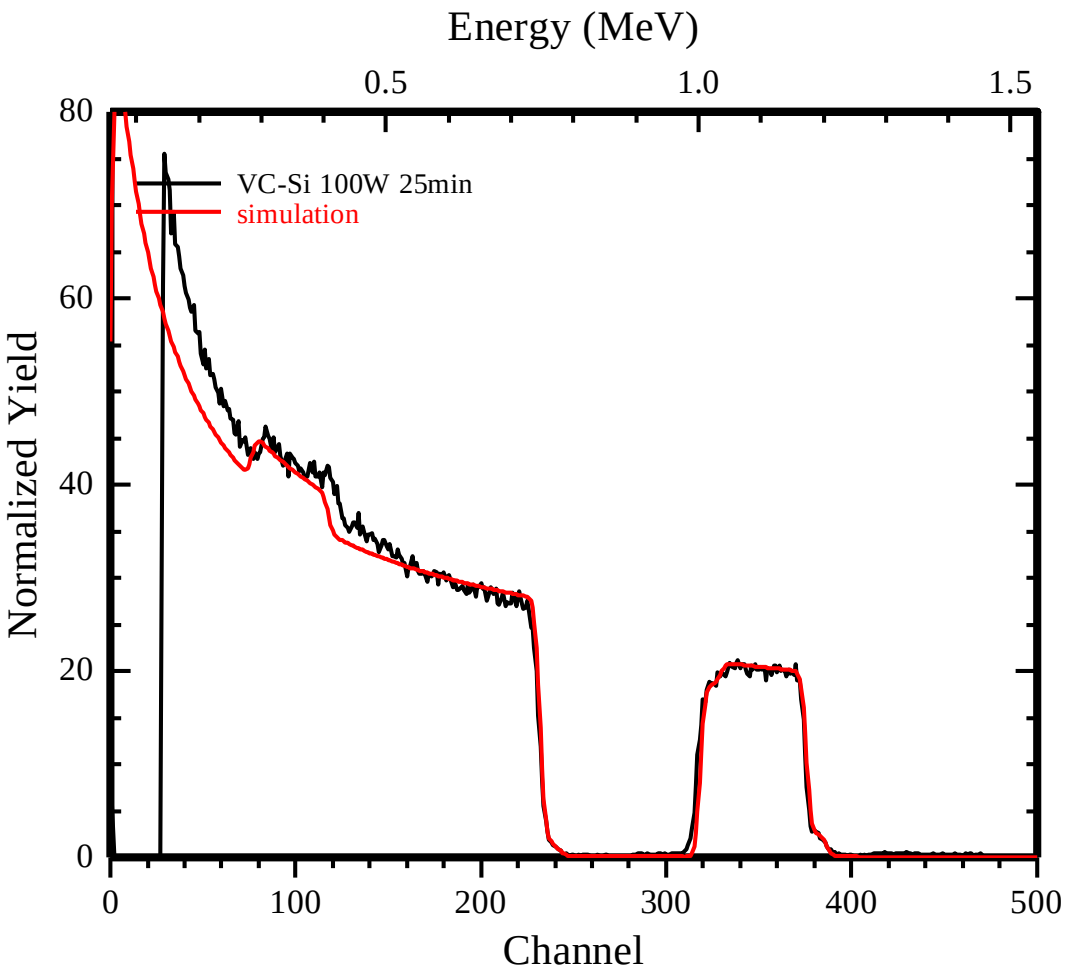

Figure 4.11 Plot of RBS spectra obtained from VC thin film deposited on Si at 100 W for 25 minutes and the fitted curve (red).

It is seen from Figs 4.9 - 4.11 that the signal for vanadium and carbon broadens with increasing film thickness in agreement with the change in detected energy with dependence of the depth of scattering as shown in equation 4.7. From the RBS results in figures 4.9 – 4.11, we

approximately have the stoichiometry VC_4. The high carbon content can be attributed to the deposition power of 100 W which causes the heavier atoms of vanadium to have less kinetic energy required to be deposited on the substrate.

4.5 Atomic force microscopy measurements

Atomic force microscopy (AFM) was used to measure the surface roughness of the deposited films. It was necessary to do this because the surface Brillouin scattering technique which was performed after the depositions requires the roughness to be low to reduce the attenuation of the signal by film or surface roughness. AFM can be carried out in either contact mode, non-contact mode or in tapping mode. In the present case, the measurements were performed in tapping mode. In this mode, a tip is scanned on the sample whilst attached to the end of an oscillating cantilever. The vertical position of the tip at each scan point is measured using a photodiode and stored so as to form a profile of the sample surface. The measurements were carried out at room temperature and the topographic images obtained for the VC films deposited at 100 W for 20 minutes and 60 minutes are shown in figures 4.12 and 4.13 respectively.

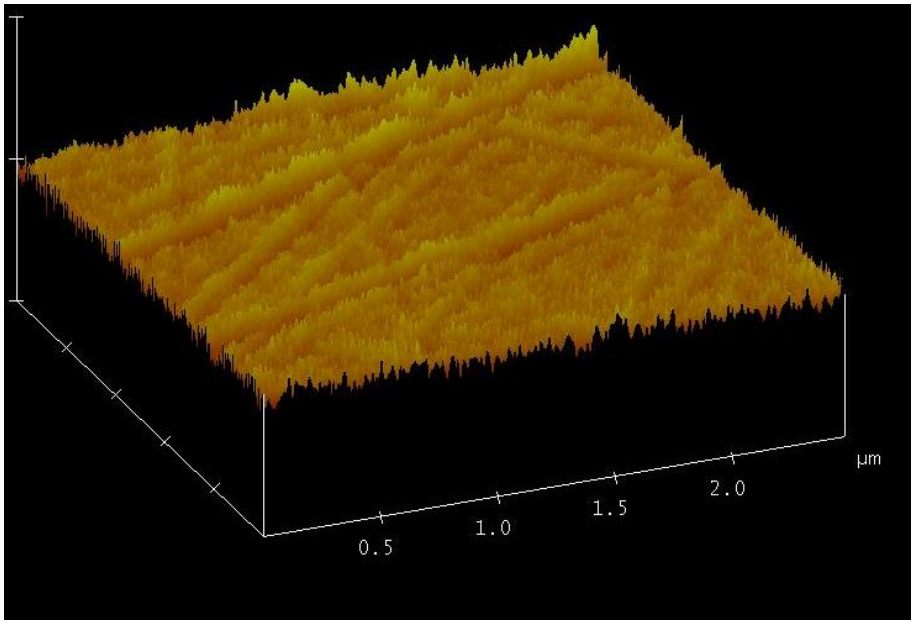

Figure 4.12 AFM measurement on VC deposited on SiC at 100 W for 20 minutes with a root mean square roughness of 1.6 nm.

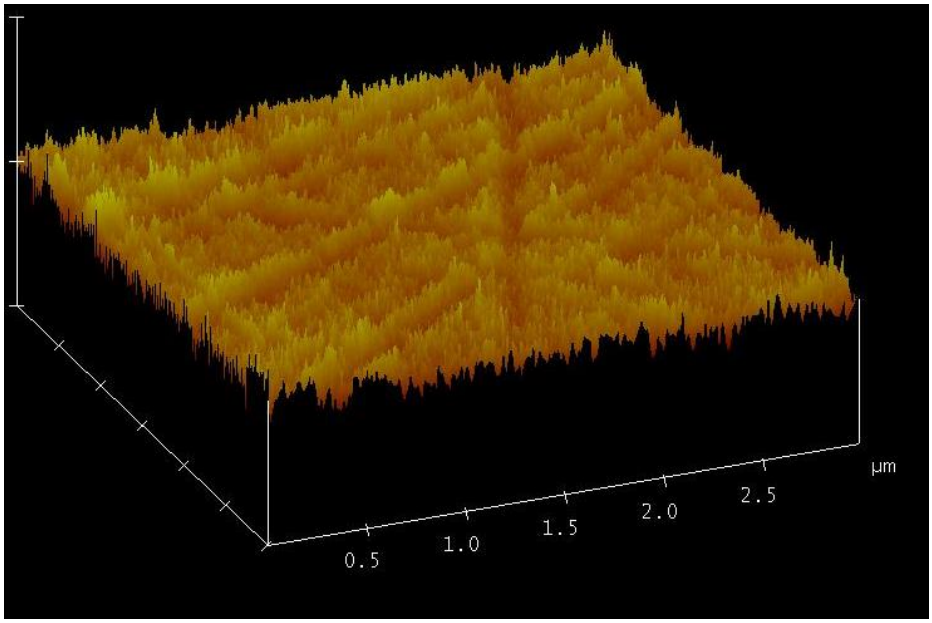

Figure 4.13 AFM measurement on VC deposited on SiC at 100 W for 60 minutes with a root mean square roughness of 1.9 nm.

Table 4.3 shows the degrees of roughness obtained from the sample measured using tapping mode AFM. The lowest value of roughness obtained is for the film deposited for 80 minutes resulting in a film thickness of 685.6 nm and a roughness of 1.3 nm. The highest is 2.5 nm for the film deposited for 40 minutes resulting in a thickness of 342.8 nm. There is no obvious trend in the values of roughness but the values are comparable to the ones obtained from XRR measurements in section 4.2 for films grown with much shorter deposition times. This seems to suggest that surface roughness does not increase with longer deposition time or for films deposited with larger thicknesses. It is also important to note that all the measured roughness values are much less than the laser wavelength used for the Brillouin scattering measurements of 514.5 nm.

Deposition Time (minutes)	**Film Thickness (nm)**	**Surface Roughness (nm)**
20	171	1.6
30	257	1.8
40	343	2.5
60	514	1.9
90	771	1.3

Table 4.3. Surface roughnesses for VC films deposited on SiC using tapping mode AFM. measurements.

4.7 Summary

Thin films of VC were deposited on Si and SiC substrates using RF magnetron sputtering. The deposition times were varied from 10 minutes to 80 minutes to obtain films with different thicknesses. Techniques including X-ray reflectivity (XRR), X-ray diffraction, Rutherford backscattering spectrometry (RBS) and atomic force microscopy (AFM) were used to characterise the films. With XRR, the thicknesses of 3 films were determined for extraction of a deposition rate of 8.57 nm. This value was used to determine the film thicknesses of all the films deposited for SBS measurements. RBS showed that the composition of the films was 0.2 vanadium and 0.8 carbon. The values of the film thicknesses obtained from RBS measurements have a large uncertainty and so they differ from those determined from XRR measurements except for the film deposited for 10 minutes because of the non-linearity arising in changes in the beam energy for thicker samples.

XRD experiments showed that the deposited films are amorphous and not polycrystalline or textured. A measure of the roughness of the surface of the deposited films was obtained from AFM measurements and it was noted that the highest values obtained were around 2.5 nm. This is much less than the 514.5 nm laser wavelength which was used to obtain the surface Brillouin scattering spectra presented in the next chapter. Thus it was not expected that substantial noise would be experienced in these spectra. We also found that there is no difference in the parameters obtained for depositions on Si and on SiC substrates with the characterization techniques we used.

Chapter 5: Surface Brillouin scattering on thin films of VC/Si and VC/SiC

Vanadium carbide is a refractory material with properties such as a high melting point, high hardness, corrosion and wear resistance (Hollox 1968; Chong et al., 2014). It has been reported that the phase diagrams of vanadium-carbon, tantalum-carbon and niobium-carbon systems are similar (Hollox, 1968). In bulk VC, the vanadium atoms are in a cubic structure where the spacing between the vanadium atoms is about 9% larger than that in pure vanadium (Hollox, 1968).

Bulk vanadium carbide has been studied using surface Brillouin scattering by Zhang et al., 1998 where it was shown that the stiffness constants vary depending on the stoichiometry of the material. Zhang et al., used VC crystals prepared using the floating zone technique and the SBS measurements collected from the cubic (100) and (110) planes of different carbon compositions, VC_x, with x varying from 0.75 to 0.88. It was also shown in the report by Zhang et al. that there is a variation of the elastic stiffness's from different reports with values obtained for C_{11} ranged from 366 to 527 GPa, C_{12} from 84 to 292 GPa and C_{44} ranging from 136 to 192 GPa (Kumashiro et al. 1977; Toth 1971; Rowcliffe and Hollox 1971).

Theoretical studies by Chong et al. 2014 using density functional theory and the Debye quasi-harmonic approximation have been carried out on VC, α-V_2C (orthorhombic), β-V_2C (hexagonal), V_4C_3 , V_6C_5 and V_8C_7 and give a discussion of the mechanical properties, electronic structure and the elastic anisotropy of the vanadium carbides. They obtained elastic constants of vanadium carbides of different stoichiometry by using the generalized Hooke's law (Han et al. 2012). Chong at al. 2014, also calculated the hardness based on the number of bonds per unit area and the strength of bonding following the expressions developed by (Gao, 2004). In this study, they found a highest hardness of 36.37 GPa for V_8C_7 and a lowest hardness of 13.76 GPa for α-V_2C.

In the present chapter the results of the studies of the elastic stiffnesses of various thin films of vanadium carbides deposited using RF magnetron sputtering on silicon and silicon carbide

substrates are presented. As in Chapter 4, for simplicity in the subsequent sections and chapters the sub-stoichiometric vanadium carbide films ($V_{0.2}C_{0.8}$) produced for the present work will be referred as VC thin films.

These studies have been carried out using the surface Brillouin scattering technique. The film preparation and characterisation methods used to determine parameters such as film thickness, structure and density have been outlined in chapter 4.

5.1 Voigt, Reuss and Hill methods for determining elastic stiffnesses

Effective elastic constants can be obtained from the Voigt-Reuss-Hill averaging methods for polycrystalline materials. However, in the present case, this has been used to obtain an estimate of the elastic stiffnesses of the VC thin films in order to obtain starting values for the fitting procedures carried out after surface Brillouin scattering spectra have been acquired.

The Voigt approximation assumes the strains to be equal in all the grains whereas the Reuss approximation makes the assumption that the stress is uniform in all the grains (Hirsekorn, 1990). The Hill approximation takes the Voigt and Reuss approximations as the upper and lower bounds and therefore uses the average values from the two methods (Hirsekorn 1990; Salas et al. 2011). Stress and strain are related by Hooke's Law in the Voigt contracted form as follows,

$$\sigma_I = C_{IJ}\varepsilon_J, \quad (I, J = 1, 2, \ldots 6), \tag{5.1}$$

where σ_I is the stress tensor and ε_J is the strain tensor. A 6 × 6 matrix can be used to transform the stress or strain (Crowhurst, 2001; Pang, 1997) and thus,

$$\sigma'_I = M_{IJ}\sigma_J, \quad (I, J = 1, 2, \ldots 6), \tag{5.2}$$

where M_{IJ} is the transformation matrix $[M]$ for the stress. Similarly for the strain,

$$\varepsilon'_I = N_{IJ}\varepsilon_J, \quad (I, J = 1, 2, \ldots 6). \tag{5.3}$$

An application of the stress transformation to Hooke's law (equation 5.1), gives,

$$[\sigma'] = [M][C][\varepsilon]. \tag{5.4}$$

The matrix $[\varepsilon]$ is given by, $[\varepsilon] = [\varepsilon'][N]^{-1}$, so substitution into 5.4 gives the equation,

$$[\sigma'] = [C'][\varepsilon'], \tag{5.5}$$

where $[C'] = [M][C][N]^{-1}$ is the transformed stiffness matrix. Following the same procedure, the transformed compliance matrix is given by $[S'] = [N][S][M]^{-1}$. If $[N]^{-1} = [M]^{\dagger}$ and $[M]^{-1} = [N]^{\dagger}$ then following Pang 1997,

$$[C'] = [M][C][M]^{\dagger}, \tag{5.6}$$

and,

$$[S'] = [N][S][N]^{\dagger}. \tag{5.7}$$

Transformation of $[C']$ and $[S']$ to cylindrical coordinates can be carried out in a similar way to obtain $[C'']$ and $[S'']$ as follows,

$$[C''] = [M_c][C''][M_c]^{\dagger}, \tag{5.8}$$

and,

$$[S''] = [N_c][S''][N_c]^{\dagger}. \tag{5.9}$$

This leads to,

$$\bar{C}_{\alpha\beta} = \frac{\int_0^{2\pi} C''_{\alpha\beta} d\phi}{2\pi}, \tag{5.10}$$

and,

$$\bar{S}_{\alpha\beta} = \frac{\int_0^{2\pi} S''_{\alpha\beta} d\phi}{2\pi}, \tag{5.11}$$

where $C''_{\alpha\beta}$ and $S''_{\alpha\beta}$ are elements of the matrices $[C'']$ and $[S'']$ respectively (Crowhurst, 2001; Pang, 1997). X-ray diffraction measurements on the vanadium carbide thin films in chapter 4 showed that the films are amorphous so only two independent elastic stiffnesses are obtained.

5.2 Surface Brillouin scattering measurements on VC/Si

Surface Brillouin scattering measurements were carried out on samples of VC deposited on silicon substrates with a (100) orientation in the backscattering geometry. Seven films were grown with varying deposition times and therefore film thicknesses. These films were deposited at an RF power of 100 W with the substrate at a distance of 6 cm from the target. The target was pre-sputtered for at least 15 minutes for each film deposition in order to remove the surface layer which may have had contaminations from being in air. The substrates were also plasma-etched to remove the oxide layer. Removal of the oxide layer enhances adhesions of the deposited film. The film thicknesses were measured using the X-ray reflectometry technique which has been discussed in chapter 4.

An overview of the surface Brillouin scattering (SBS) technique has been given in chapter 2. After deposition, the SBS spectra were collected using a single mode Coherent argon ion laser operated with a wavelength of 514.5 nm with less than 100 mW of laser power falling on the sample. These were carried out using a 71° angle of incidence at ambient temperature and the spectra were collected over at least 24 hours in order to obtain sharp peaks and to maximise the signal-to-noise ratio. Spectra were collected for all the seven films providing a variation in the film thicknesses.

The values of the dimensionless product of the surface phonon wave-vector and the film thickness for each film, namely $k_{||}d$ were now calculated. As discussed in chapter 2, the surface phonon wave-vector is given by the expression,

$$k_{||} = 2k_i \sin\theta,$$

where k_i is the wave-vector of the incident laser light, and θ is the angle of incidence which was 71° in the present case. These values for the VC films are presented in Table 5.1 below with a range from 1.0 to 7.9. These results permitted the plotting of the dispersion curves of the surface acoustic wave velocity versus $k_{||}d$. The velocity was calculated from the peak positions of the Rayleigh and Sezawa modes obtained from the SBS spectra for each of the films using the equation also discussed in chapter 2,

$$v = \Delta\omega/k_{||}.$$

Deposition time (minutes)	**Film thickness (nm)**	$k_{\|\|}d$
5	43	1.0
10	86	2.0
15	131	3.0
20	171	4.0
25	215	5.0
30	257	5.9
40	343	7.9

Table 5.1 Calculated values of the product of film thickness and the surface phonon wave-vector $k_{||}d$ for VC/Si for each layer thickness and deposition time.

The spectra collected from the VC/Si films are shown in figure 5.1. It can be seen that a sharp Rayleigh peak just below 16 GHz is observed for all films and an additional Sezawa mode is observed for $k_{||}d = 5.0$, 5.9 and 7.9. The velocity dispersion curves for the thin films of vanadium carbide deposited on silicon substrates were plotted using the data obtained from the SBS spectra and is shown in figure 5.2. It can be seen that the Rayleigh mode velocity is around 4 365 m/s for $k_{||}d = 1.0$ which represents the film with the lowest thickness of 43.8 nm. It reduces to values of around 4 200 m/s for the remainder of the films showing that the Rayleigh is no longer influenced by the substrate for the thicker vanadium carbide films.

Two cases can arise when thin films are deposited on a substrate. In the first case, the film can be elastically harder when compared to the substrate. In this situation the acoustic waves propagating in the film will have higher velocities compared to the velocities in the substrate. This case is described as a hard on soft system or a fast on slow system. In the second case the reverse situation exists where the substrate is elastically harder than the deposited film and is referred to as a soft on hard system or a slow on fast system (Farnell and Adler 1972; Zinin et al. 1999).

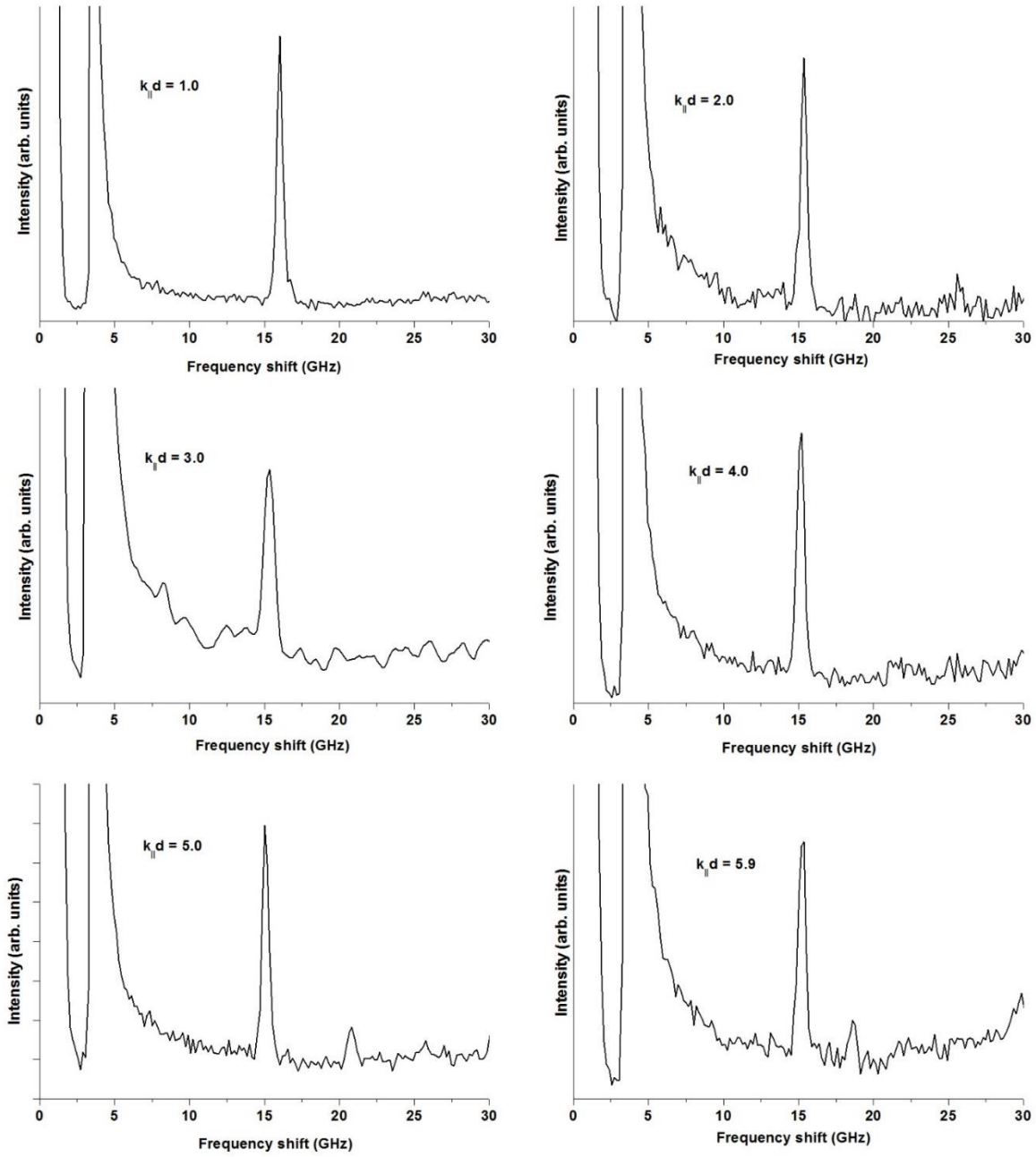

Figure 5.1 Anti-Stokes SBS spectra of VC/Si thin films of varying thickness deposited on Si substrates obtained using a 514.5 nm wavelength laser at a 71° angle of incidence. The spectra show an intense Rayleigh peak and a limited number of Sezawa waves. Peaks in the range of 0 to 5 GHz arise from the elastically scattered light and the instrumental shutter system.

.

Rayleigh surface acoustic wave velocities obtained for single crystalline cubic VC with (100) orientation using SBS decrease as the carbon to metal ratio decreases from 5 000 m/s for $VC_{0.88}$ to 4 550 m/s for $VC_{0.75}$ (Zhang et al., 1998). However, the vanadium carbide films deposited in the present thesis ($V_{0.2}C_{0.8}$) have a higher carbon content compared to the metal content as

observed from the RBS measurements in chapter 4. This means that lower Rayleigh-SAW velocities are expected which is consistent with the observations in figure 5.2 were they start at 4 400 m/s for $k_{||}d = 1$ and reduce to about 4 200 m/s for films of larger thicknesses. The Rayleigh surface acoustic wave velocity for the (100) silicon substrates ranges from 4 800 m/s to 4 980 m/s (Sandercock, 1978; Stoddart et al., 1995). Therefore, comparing the velocities obtained in the present films to the ones from the substrate, it is concluded that there is an elastically soft film on an elastically harder substrate. However the presence of a few Sezawa waves limits the ability to achieve the elastic stiffnesses using the fitting procedure as shown below.

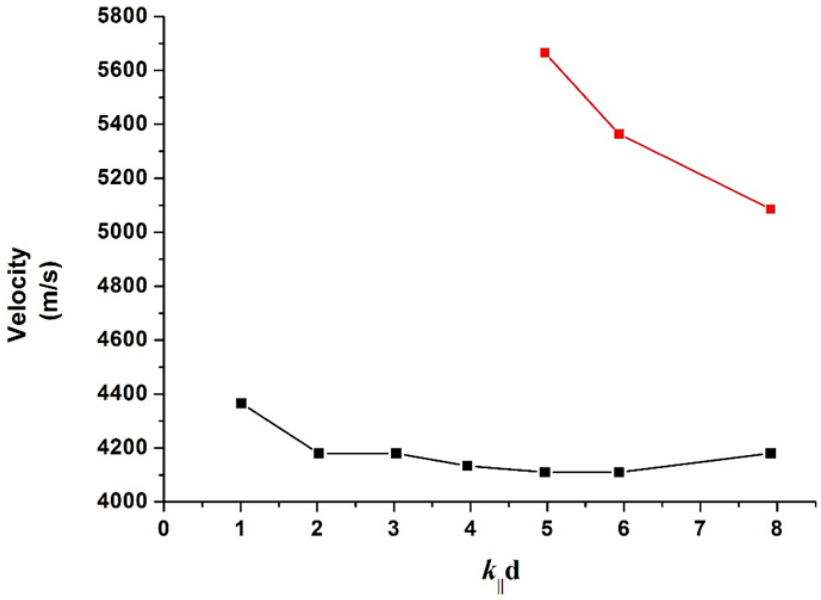

Figure 5.2 Dispersion curves from the SBS spectra shown in Figure 5.1 of VC/Si thin films of varying thickness on Si substrates obtained at a 71° angle of incidence.

In order to extract the elastic stiffnessess of the VC films, a computation using a weighted least-squares fit between the experimental data and calculations was performed (Wittkowski et al., 2000; Wittkowski et al., 2004). This was done by a chi-square minimization computation of the form,

$$\chi^2 = \sum\sum w_{ij}\left(v_{ij}^{meas} - v_{ij}^{cal}\right)^2,$$

where v_{ij}^{meas} is the measured phase velocity, v_{ij}^{calc} is the calculated phase velocity, and w_{ij} are the weighting factors determined from the measurement errors. This was done using a FORTRAN program written by Hillebrands and Walter (University of Kaiserslautern,

Germany). The elastic stiffnesses used for the Si substrate are C_{11} = 165 GPa C_{12} = 63 GPa and C_{44} = 79.1 GPa (Jakata and Every, 2008). For an isotropic film, it has been shown that the elastic stiffness tensor reduces to the form,

$$\begin{pmatrix} C_{11} & C_{12} & C_{12} & 0 & 0 & 0 \\ C_{12} & C_{11} & C_{12} & 0 & 0 & 0 \\ C_{12} & C_{12} & C_{11} & 0 & 0 & 0 \\ 0 & 0 & 0 & C' & 0 & 0 \\ 0 & 0 & 0 & 0 & C' & 0 \\ 0 & 0 & 0 & 0 & 0 & C' \end{pmatrix}$$

where $C' = \frac{1}{2}(C_{11} - C_{12})$ is the Cauchy relation for an isotropic system (Levy et al., 2001).

The least squares fitting procedure did not converge to a unique set of elastic stiffnesses for the films deposited on the Si substrate because only 3 experimental data points for the Sezawa modes were obtained. For this reason 6H-SiC was subsequently used as the substrate.

5.3 Surface Brillouin scattering measurements on VC/6H-SiC

The VC/6H-SiC films were prepared at 100 W by RF magnetron sputtering in a similar manner to those discussed in Chapter 4 and section 5.2. As discussed previously, an overview of the surface Brillouin scattering technique is given in chapter 2. Values of $k_{||}d$ for each thin film as done for those deposited on silicon are shown in table 5.2 below.

Film thickness (nm)	86	171	257	343	429	514	771
$k_{\|\|}d$	1.98	3.96	5.94	7.92	9.90	11.88	17.81

Table 5.2 Calculated values of the product of film thickness and the surface phonon wave-vector $k_{||}d$ for VC/SiC.

The spectra in figures 5.4 show intense Rayleigh peaks in each case with an increased number of Sezawa waves as compared to the results of VC/Si shown in section 5.2. The observation of the Sezawa modes shows that the acoustic wave speed in the vanadium carbide layer is lower than that in the silicon carbide substrate or that the elastic stiffnesses in the layer are lower than those in the substrate. Some of the Sezawa modes in the spectra corresponding to $k_{||}d$ = 7.92

and $k_{||}d$ = 9.90 are unusually broad which may be a result of a superposition of peaks which are close to each other.

The lower frequency features in the spectra are associated with the elastically scattered light and an instrumental peak due to the shutter (sections 2,2).

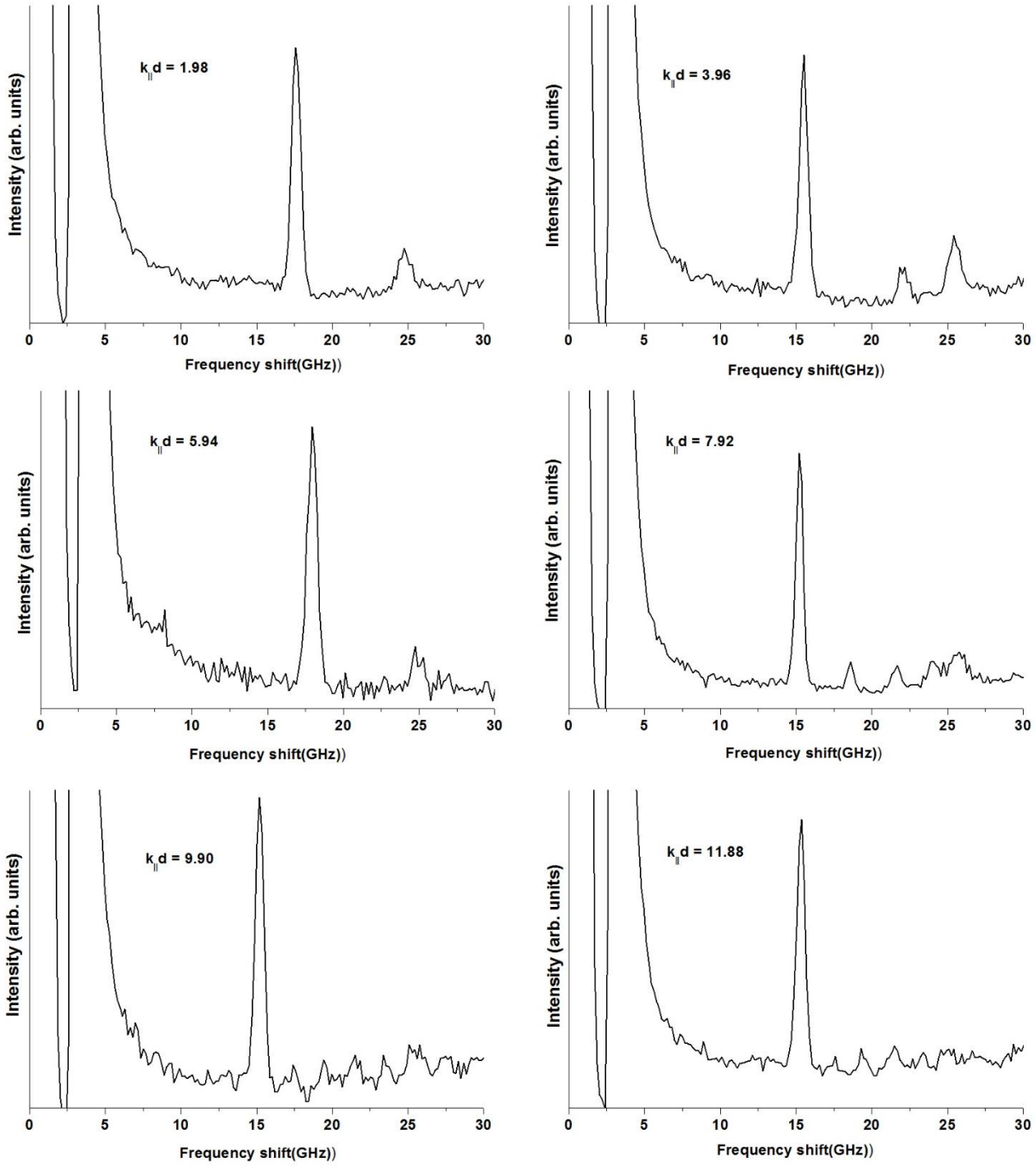

Figure 5.3 Anti-Stokes SBS spectra of VC thin films deposited on 6H-SiC substrates of varying thickness obtained using a 514.5 nm wavelength laser at a 71° angle of incidence. The spectra

show an intense Rayleigh peak and an increasing number of Sezawa waves. Peaks in the range of 0 to 5 GHz arise from the elastically scattered light and the instrumental shutter system.

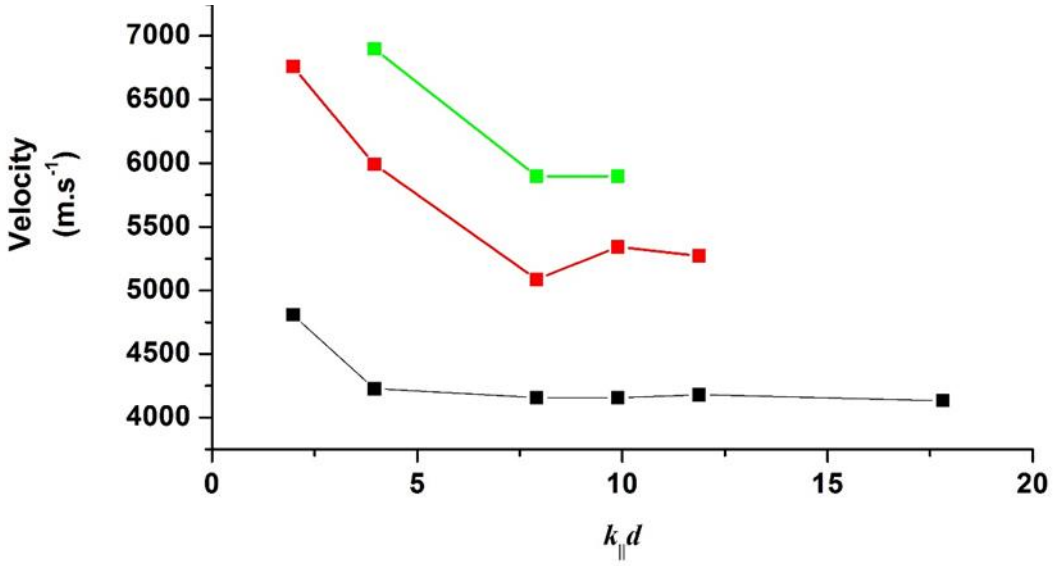

Figure 5.4 Dispersion curves from the SBS spectra shown in Figure 5.4 of VC thin films of varying thickness on 6H-SiC substrates obtained at a 71° angle of incidence.

A plot of the dispersion curves obtained from the SBS measurements is shown in figure 5.5 with the Rayleigh mode velocities (black curve) having the lowest values and flattens out at about 4250 m/s for $k_{||}d$ above 5. In order to increase the number of data points for the computation used to obtain the elastic stiffnesses of the VC films, additional experiments were performed were the angles of incidence were varied for some of the films. A sample of some of these measurements is shown in figure 5.6 below. This has the effect of adding a few more data points around the ones obtained at 71° angle of incidence since $k_{||}$ is a directly proportional to $\sin\theta$. It also has the added advantage of showing that the film deposition conditions were similar for all films (Wittkowski et al. 2000; Wittkowski et al. 2004).

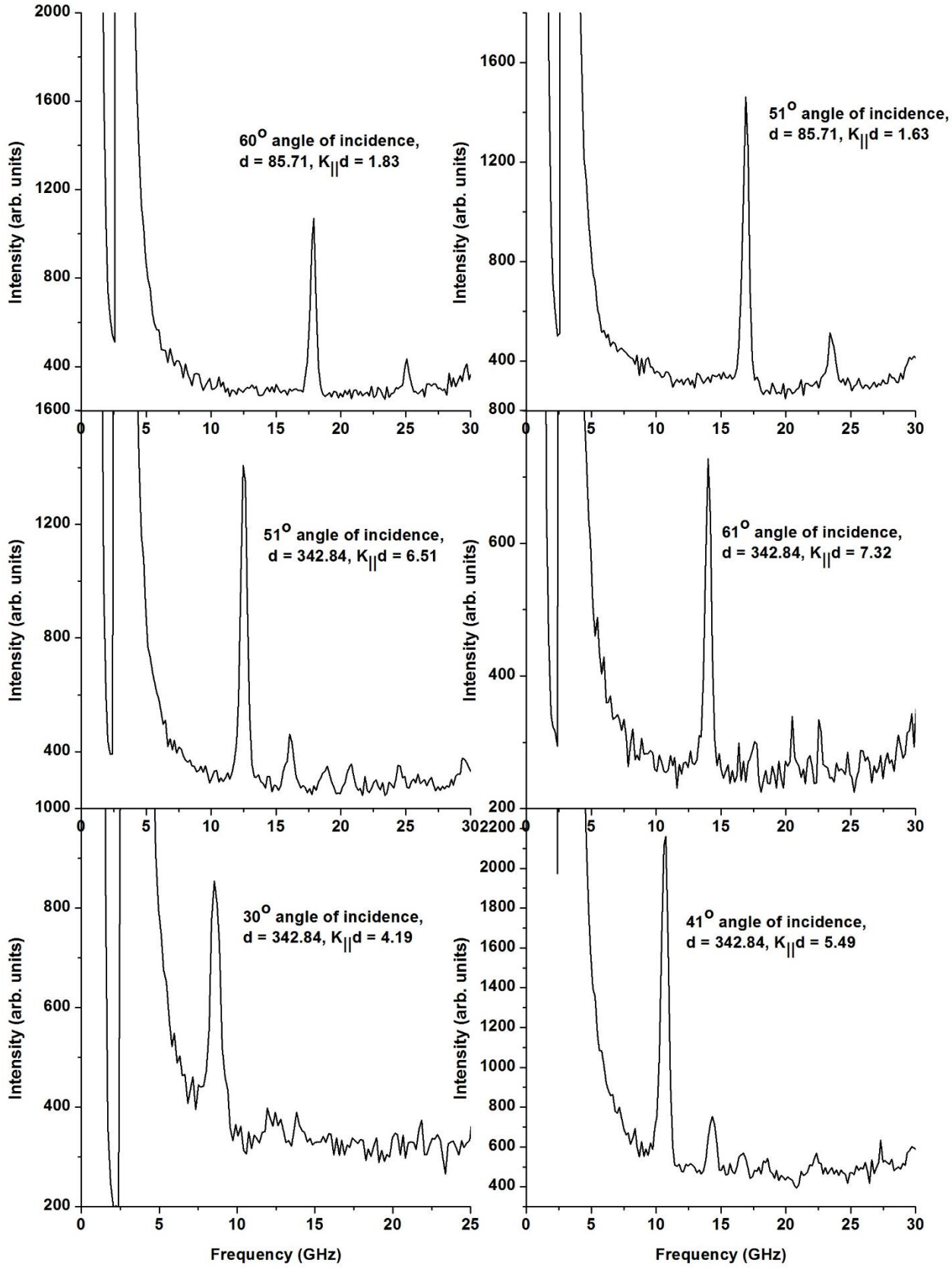

Figure 5.5 Anti-Stokes SBS spectra of VC thin films deposited on 6H-SiC substrates of varying thickness obtained using a 514.5 nm wavelength laser at varying angles of incidence. The results show a substantial number of Sezawa waves. Peaks in the range of 0 to 5 GHz arise from the elastically scattered light and the instrumental shutter system.

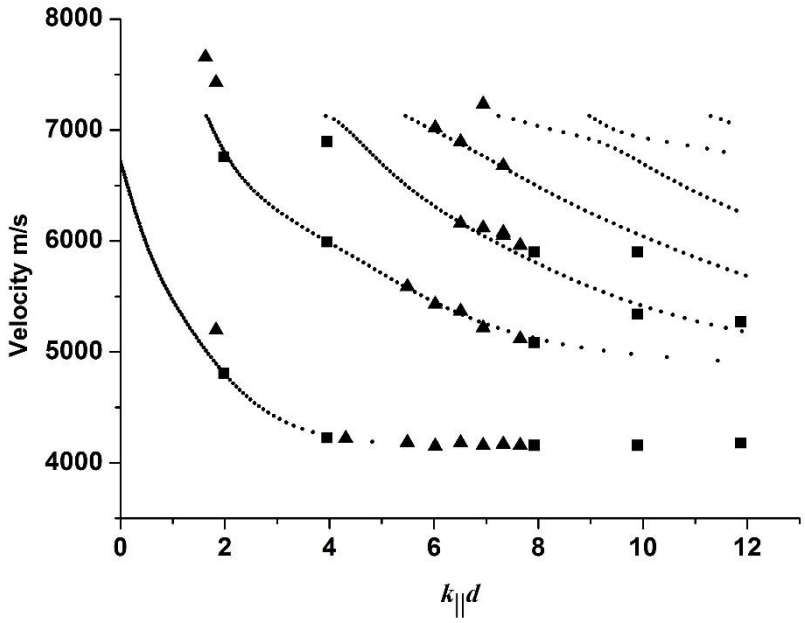

Figure 5.6 Dispersion curves from the SBS spectra of VC thin films deposited on 6H-SiC substrates for data points of films measured at 71° angle of incidence (squares) and those films in which the angle of incidence was varied (triangles). The dotted lines represent the dispersion curves obtained using the elastic stiffnesses after the fitting procedure.

The above dispersion curves obtained for the VC/6H-SiC measurements indicate that the VC layer is elastically softer than the 6H-SiC substrate since the Rayleigh mode velocity initially decreases from 4 806 ms^{-1} with increasing $k_{||}d$ to a value of 4 157.0 ms^{-1} and then becomes relatively unchanged. From $k_{||}d$ of 4.0, the Rayleigh surface acoustic wave velocity of the vanadium carbide layer is essentially constant, showing little influence from the silicon carbide substrate.

As discussed previously in section 5.2 , in order to extract the elastic stiffnessess of the VC films, a computation using a weighted least-squares fit between the experimental data and calculations was performed (Wittkowski et al., 2004, 2000). These same procedures were used to determine the elastic stiffnessess of the VC/6H-SiC films. The fitting was performed using the elastic stiffness of 6H-SiC obtained from Kamitani et al., (1997) namely $\mathrm{C}_{11} = 501\ \mathrm{GPa}, \mathrm{C}_{33} = 553\ \mathrm{GPa}, \mathrm{C}_{44} = 163\ \mathrm{GPa}, \mathrm{C}_{13} = 52\ \mathrm{GPa}$ and $\mathrm{C}_{12} = 111\ \mathrm{GPa}$. The best fit to the experimental data was obtained for the values $C_{11} = 238.6\ GPa,$ and $C_{12} = 54.9\ GPa.$ There is good agreement between the experimental data and the computations as shown by the comparison between the dotted lines representing the dispersion curves from the fitting procedure and those of the experimental data.

There is good agreement between the experimental data and the computations as shown by the comparison between the black dotted lines shown in figure 5.7 and representing the dispersion curves from the fitting procedure and those of the experimental data.

5.4 Summary

Brillouin scattering spectra from thin films of vanadium carbide ($V_{0.2}C_{0.8}$) on silicon and 6H-silicon carbide substrates were produced. A least-squares fitting procedure using a FORTRAN program as discussed in section 5.2 was carried out in order to determine the elastic stiffnesses of the films. For films deposited on the 6H-SiC substrate, the best fit to the experimental data was obtained for the elastic stiffness values $C_{11} = 238.6\ GPa$, and $C_{12} = 54.9\ GPa$.

Chapter 6: Discussion and Conclusions

Two research projects have been reported in this thesis:

1) The recrystallization of argon-ion bombarded GaAs studied using surface Brillouin scattering and Raman spectroscopy.
2) Determination of the elastic constants of thin films of vanadium carbide deposited on Si and 6H-SiC substrates using RF magnetron sputtering.

6.1 Ion implanted GaAs

The recrystallization of GaAs after ion bombardment with Ar-ions at 100 keV has been studied using surface Brillouin scattering and Raman spectroscopy. To the best of the author's knowledge, this is the first time that this type of investigation has been carried out using both of these techniques.

The damage caused by ion implantation into (100) crystalline gallium arsenide resulted in the formation of an amorphous layer of GaAs above a crystalline substrate. These experiments were carried out on three samples with the first one, sample A, implanted at liquid nitrogen temperature and a fluence of 2×10^{14} ions/cm^2. Sample B was implanted at liquid nitrogen temperatures and a higher fluence of 1×10^{15} ions/cm^2 and sample C was implanted at an elevated temperature of ~50 ^{o}C and the highest fluence of 5×10^{16} ions/cm^2.

In sample A, which was bombarded at the lowest ion fluence of 2×10^{14} ions/cm^2 at 77 K, the Raman spectra showed the presence of a broad feature substantially replacing that of the original sharp peak of the crystalline phase. This showed the formation of an amorphous layer. However, the broad feature had a shoulder which suggested that there was incomplete damage in the sample due to the low ion fluence used for bombardment. On annealing, sharp LO and TO peaks were obtained at 280 ^{o}C which shows that amorphous GaAs recrystallizes into a polycrystalline material. From the surface Brillouin scattering experiments, the frequency shift of the Rayleigh mode obtained after ion implantation was 8.6 GHz and this increases due to

recrystallization on annealing starting from 80 ^{o}C reaching a maximum at 280 ^{o}C which is in good agreement with the Raman scattering results.

Sample B, which was bombarded at a higher ion fluence of 1×10^{15} ions/cm^2 and at liquid nitrogen temperature also showed the attainment of an amorphous layer with a broad feature obtained from Raman spectroscopy and a shift in the Rayleigh wave to a lower frequency. Raman spectra collected after each anneal step show that peaks start appearing superimposed on the broad amorphous feature at 180 ^{o}C. The TO peak had a higher intensity compared to the LO peak for anneals up to 260 ^{o}C which seems to suggest that a higher fraction of the recrystallized material does not have (100) orientation. After the anneal step at 260 ^{o}C, two sharp peaks were obtained with the LO peak having the higher intensity showing that a higher fraction of the recrystallized material now has (100) orientation. SBS results also showed that the Rayleigh peak frequency starts shifting for anneal steps above 80 ^{o}C and attains a maximum at 240 ^{0}C which is lower than the observation from Raman measurements. Sezawa modes were not observed in the SBS spectra for samples A and B implanted at low fluence and low temperature resulting from the limited thickness of the respective damaged layers.

For sample C, implanted at an elevated temperature of ~50 ^{o}C and the highest fluence of 5×10^{16} ions/cm^2 , the Raman spectra showed no changes for anneal temperatures below 500 ^{o}C. Two peaks with a weak intensity appeared after the anneal at 525 ^{o}C showing the commencement of the recrystallization process. At 625 ^{o}C, two sharp peaks appeared showing full recrystallization in contrast to the single peak obtained before ion implantation. This is because the amorphous layer had recrystallized into polycrystalline GaAs and an LO peak at 283.7 cm^{-1} and a transverse optical (TO) peak at 258.3 cm^{-1} were obtained. The LO peak had shifted from 292 cm^{-1} before implantation to 283.7 cm^{-1} after recrystallization which is attributed to thermal stresses that were caused by the heating and cooling cycles during the isochronal annealing process.

Surface Brillouin scattering spectra were also collected before ion bombardment of sample C with a Rayleigh surface acoustic wave and a Lamb shoulder as expected from a single crystal material. The spectra obtained after ion implantation had in addition to the Rayleigh SAW, a peak due to Sezawa waves. This also served to confirm the formation of a layered material, a-GaAs/c-GaAs, where the layer is elastically softer when compared to the substrate.

It was also noted that the Rayleigh mode frequency was shifted to 7.8 GHz compared to the values of around 10 GHz obtained for the un-implanted sample. This shift is attributed to the softening of the implanted layer of the sample. SBS measurements carried out after each anneal step showed that the Rayleigh frequency was increasing to higher frequencies starting from the anneal step at 100 ^{o}C and increased gradually until it attained a maximum value of 8.8 GHz at 450 ^{o}C. This is in contrast to the Raman measurements were the changes due to recrystallization start being observed after anneal temperatures above 500 ^{o}C. This difference in SBS and Raman measurements can be explained by the fact that SBS is sensitive to changes in the elastic stiffnesses whilst Raman spectroscopy is more sensitive to changes in the structure.

6.2 Thin films of VC/Si and VC/SiC

The second part of the thesis involved work on the deposition and characterization of vanadium carbide thin films on silicon and silicon carbide substrates followed by an investigation of the elastic stiffnesses of the thin films using surface Brillouin scattering. To the author's best knowledge, this is also the first time that the elasticity of $V_{0.2}C_{0.8}$ have been determined using surface Brillouin scattering.

$V_{0.2}C_{0.8}$ films were grown using RF magnetron sputtering at an RF power of 100 W whilst varying the deposition time in order to obtain films with different thicknesses. X-ray reflectometry (XRR) was used to determine the thickness of the films, the density and the roughness. The roughness values obtained were compared with atomic force microscopy measurements and were found to be in good agreement. X-ray diffraction measurements revealed that the deposited films were amorphous whilst Rutherford backscattering (RBS) results provided values of thin film thickness and stoichiometry. It was found that the films had a much higher carbon composition compared to that of vanadium. The film thicknesses obtained from RBS were not in good agreement with XRR results for the thicker films. This is expected since RBS does not give accurate results for thick films because the backscattered particles lose more energy from multiple collisions when entering the sample and then emerging from the sample.

SBS spectra were then collected from each sample. The spectra obtained from films deposited on a silicon substrate did not result in many Sezawa modes and as a result, the elastic stiffnesses could not be determined unambiguously for the VC/Si system. However, for the films deposited on 6H-SiC, more Sezawa waves were obtained and a least squares fitting program

could be used to extract the elastic stiffnesses of these film. The best fit to the experimental data was obtained for the values $C_{11} = 238.6\ GPa$, and $C_{12} = 54.9\ GPa$. These values are lower than those of bulk vanadium carbides with higher vanadium compositions that have been carried out as expected. The dispersion curves of both VC/6H-SiC and VC/Si showed that in both cases, a soft on hard system was obtained or that the Rayleigh surface acoustic waves in the deposited layer have a lower velocity compared to that in the substrate.

6.3 Future work

Future research may be carried out in the following areas:

1) High resolution transmission electron microscopy (TEM) can be used in conjunction with SBS and Raman spectroscopy to determine the structural changes that result in the differences in the annealing temperatures where recrystallization starts being observed with the Raman and SBS techniques.
2) Implanting GaAs using argon-ions with varying energies at the same fluence and temperature to obtain amorphous layers with varying thicknesses. These can be used to investigate the elastic stiffnesses of amorphous GaAs layers following SBS measurements.
3) Deposition of thin films from vanadium carbide grown at different RF powers, pressure, and substrate temperature in order to obtain different metal to carbon compositions and observe how the elastic stiffnesses vary with stoichiometry.
4) Investigate the elastic stiffnesses of other transition metal carbide thin films such as niobium carbide.

References

Aghaie-Khafri, M., and Fazlalipour, F. (2008). Vanadium carbide coatings on die steel deposited by the thermo-reactive diffusion technique. *Journal of Physics and Chemistry of Solids*, *69*(10), 2465–2470.

Bauer, G., and Richter, W. (1996). *Optical characterization of epitaxial semiconductor layers*. Springer-Verlag.

Beghi, M. G., Every, A. G., Prakapenka, V. B., and Zinin, P. V. (2012). Measurement of the Elastic Properties of Solids by Brillouin Spectroscopy. T. Kundu (Ed.), *Ultrasonic and Electromagnetic NDE for Structure and Material Characterization*, CRC Press, Boca Raton, Chapter 10, pp. 539-610;

Bench, M. W., Robertson, I. M., and Kirk, M. A. (1991). Transmission electron microscopy investigation of the damage produced in individual displacement cascades in GaAs and GaP. *Nuclear Instruments and Methods in Physics Research Section B: Beam Interactions with Materials and Atoms*, *59*, 372–376.

Berndt, H., Zeng, A.-Q., Stock, H.-R., and Mayr, P. (1993). Vanadium carbide films produced by plasma-assisted metal-organic chemical vapour deposition. *J. Phys. IV France*, *3*, C3-313-C3-320.

Billingham, J., Bell, P. S., and Lewis, M. H. (1972). A superlattice with monoclinic symmetry based on the compound V6C5. *Philosophical Magazine*, *25*(3), 661–671.

Bortolani, V., Marvin, A. M., Nizzoli, F., and Santoro, G. (1983). Theory of Brillouin scattering from surface acoustic phonons in supported films. *Journal of Physics C: Solid State Physics*, *16*(9), 1757.

Chalmers, J. M., and Griffiths, P. R. (2002). *Handbook of vibrational spectroscopy*. J. Wiley.

Chason, E., and Mayer, T. M. (1997). Thin Film and Surface Characterization by Specular X-Ray Reflectivity, Critical Reviews in Solid State and Materials Sciences, (September 2013), 1–67.

Chen, J. G., DeVries, B. D., Frühberger, B., Kim, C. M., and Liu, Z. -M. (1995). Spectroscopic characterization of thin vanadium carbide films on a vanadium (110) surface: Formation, stability, and reactivities. *Journal of Vacuum Science & Technology*

A: Vacuum, Surfaces, and Films, *13*(3), 1600–1605.

Chong, X., Jiang, Y., Zhou, R., and Feng, J. (2014a). Electonic structures mechanical and thermal properties of V-C binary compounds. *Royal Society of Chemistry*, *4*, 44959–44971.

Chu, W. K., Mayer, J. W., and Nicolet, M. A. (1978). *Backscattering spectrometry*. Academic Press.

Colombi, P., Agnihotri, D. K., Asadchikov, V. E., Bontempi, E., Bowen, D. K., Chang, C. H., Wiemer, C. (2008). Reproducibility in X-ray reflectometry: Results from the first world-wide round-robin experiment. *Journal of Applied Crystallography*, *41*(1), 143–152.

Comins, J. D., (2001). Chapter 15 in *Handbook of elastic properties of solids, liquids and gases,* edited by Levy, Bass and Stern. Vol 1: Dynamic methods for measuring the elastic properties of solids (Academic Press).

Crowhurst, J. C. (2001). *Surface Brillouin scattering studies of high-pressure elasticity and nickel-vanadium multilayers.* PhD Thesis, University of the Witwatersrand, Johannesburg.

Cuthrell, R. E., Mattox, D. M., Peeples, C. R., Dreike, P. L., and Lamppa, K. P. (1988). Residual stress anisotropy, stress control, and resistivity in post cathode magnetron sputter deposited molybdenum films. *Journal of Vacuum Science and Technology A: Vacuum, Surfaces, and Films*, *6*(5), 2914–2920.

Desnica-Frankovic, I. D. (1999). Different recrystallization patterns of Si+ implanted GaAs. *Journal of Applied Physics*, *85*(11), 7587–7596.

Desnica, U. V., Desnica-Frankovic, I. D. I., Ivanda, M., Furic, K., and Haynes, T. E. (1997). Morphology of the implantation-induced disorder in GaAs studied by Raman spectroscopyand ion channeling. *Physical Review B*, *55*(24), 205–216.

Emmons, G. H., and Williams, W. S. (1983). Thermodynamics of order-disorder transformations in vanadium carbide. *Journal of Materials Science*, *18*(9), 2589–2602.

Farnell, G. W., and Adler, E. L. (1972). Elastic Wave Propagation in Thin Layers. *Physical Acoustics*, *9*, 35–127.

Feranchuk, I. D., Feranchuk, S. I., Minkevich, A. A., and Ulyanenkov, A. (2003). Description

of x-ray reflection and diffraction from periodical multilayers and superlattices by the eigenwave method, *Physical Review B, 68*, *235307-235317*.

Gamo, K., Inada, T., Mayer, J. W., Eisen, F. H., and Rhodes, C. G. (1977). Reordering of implanted amorphous layers in GaAs. *Radiation Effects*, *33*(2), 85–89.

Gao, F. (2004). Hardness estimation of complex oxide materials. *Physical Review B*, *69*(9), 94113.

Gibaud, A, and Hazra, S. (2000). X-ray reflectivity and diffuse scattering. *Current Science*, *78*, 1467–1477.

Hayes, W. (1975). Scattering of light by solids. *Contemporary Physics*, *16*(1), 69–91.

Haynes, T.E, and Holland, O.W. (1991). Dose rate effects on damage accumulation in Si^+ implanted gallium arsenide. *Applied Physics Letters*. 58, 62-64.

Hirsekorn, S. (1990). Elastic properties of polycrystals: a review. *Texture, Stress, and Microstructure*, *12*(1–3), 1–14.

Hollox, G. E. (1968). Microstructure and mechanical behavior of carbides. *Materials Science and Engineering*, *3*(3), 121–137.

Holtz, M., Zallen, R., Brafman, O., and Matteson, S. (1988). Raman-scattering depth profile of the structure of ion-implanted GaAs. *Physical Review B*, *37*(9), 4609–4617.

Irvine, A., and Palmer, D. (1994, February 15). Demonstration of gallium-defect annealing at 280 K in irradiated GaAs and AlxGa1-xAs. *Physical Review. B, Condensed Matter*. 49(8), 5695 - 5698.

Ivanda, M., Desnica, U. V., and Haynes, T. E. (1994). Raman Study of "Boson Peak" in Ion-Implanted GaAs: Dependence on Ion Dose and Dose Rate. *Materials Science Forum*, *143–147*, 1387–1390.

Ivanda, M., Hartmann, I., and Kiefer, W. (1995). Boson peak in the Raman spectra of amorphous gallium arsenide: Generalization to amorphous tetrahedral semiconductors. *Phys. Rev. B*, *51*(3), 1567–1574.

Jakata, K., and Every, A. G. (2008). Determination of the dispersive elastic constants of the cubic crystals Ge, Si, GaAs, and InSb. *Physical Review B*, *77*(17), 174301.

Kamitani, K., Grimsditch, M., Nipko, J. C., Loong, C.-K., Okada, M., and Kimura, I. (1997).

The elastic constants of silicon carbide: A Brillouin-scattering study of 4H and 6H SiC single crystals. *Journal of Applied Physics*, *82*(6), 3152–3154.

Krumrey, M., Hoffmann, M., Ulm, G., and Hasche, K. (2004). Thickness determination for SiO 2 films on Si by X-ray reflectometry at the Si K edge, *459*, 241–244.

Kumashiro, Y., Tokumoto, H., Sakuma, E., and Itoh, A. (1977). The elastic constants of TiC, VC and NbC single crystals. *Internal Friction and Ultrasonic Attenuation in Solids*, 395–399.

Kuzmany, H. (2010). *Solid-State Spectroscopy: An Introduction*. Springer Berlin Heidelberg.

Levy, M., Bass, H. E., Stern, R. R., and Keppens, V. (2001). *Handbook of Elastic Properties of Solids,liquids, and Gasses Vol.1:dynamic Methods for Measuring the Elastic Properties of Solids*. Academic Press.

Liao, M. Y., Gotoh, Y., Tsuji, H., and Ishikawa, J. (2005). Deposition of vanadium carbide thin films using compound target sputtering and their field emission Deposition of vanadium carbide thin films using compound target. *Journal of Vacuum Science and Technology A*, *23*(2005), 1379.

Lipatnikov, V. N., Lengauer, W., Ettmayer, P., Keil, E., Groboth, G., and Kny, E. (1997). Effects of vacancy ordering on structure and properties of vanadium carbide. *Journal of Alloys and Compounds*, *261*(1), 192–197.

Marvin, A. M., Bortolani, V., and Nizzolil, F. (1980). Surface Brillouin scattering from acoustic phonons : I . General theory, *13*, 299–317.

Mattox, D. M. (1989). Particle bombardment effects on thin-film deposition: A review. *Journal of Vacuum Science & Technology A: Vacuum, Surfaces, and Films*, *7*(3), 1105–1114.

Mittal, K. L. (1978). *Adhesion Measurement of Thin Films, Thick Films and Bulk Coatings*. Astm International.

Mayer, M. (2003). Rutherford Backscattering Spectrometry (RBS). *Lectures given at the*

Workshop on Nuclear Data for Science and Technology, Materials Analysis, Trieste. Max-Planck-Institut for Plasma Physics, Germany.

Mock, R., Hillebrands, B., and Sandercock, R. (1987). Construction and performance of a

Brillouin scattering set-up using a triple-pass tandem Fabry-Perot interferometer. *Journal of Physics E: Scientific Instruments*, *20*(6), 656.

Nakamura, T., and Katoda, T. (1982). Raman spectra from Si and Sn implanted GaAs. *Journal of Applied Physics*, *53*(8), 5870–5872.

Ohring, M. (1992). *The Materials Science of Thin Films - Milton Ohring.pdf*. San Diego: Academic Press.

Pang, W. (1997). *Measurement of elastic properties of hard films using Brillouin scattering.* PhD Thesis, University of the Witwatersrand, Johannesburg.

Robinson, H.G., Haynes, T.E., Allen, E.L., Lee, C.C., Deal, M.D., Jones, K. S. (1994). Effect of implant temperature on dopant diffusion and the defect morphology for Si implanted GaAs. Journal of Applied Physics. 76(8), 4571 - 4575.

Rowcliffe, D. J., and Hollox, G. E. (1971). Hardness anisotropy, deformation mechanisms and brittle-to-ductile transition in carbide. *Journal of Materials Science*, *6*(10), 1270–1276.

Salas, E., Riobóo, R. J. J., Prieto, C., and Every, A. G. (2011). Surface acoustic wave velocity of gold films deposited on silicon substrates at different temperatures. *Journal of Applied Physics*, *110*(2), 23503.

Sandercock, J. R. (1978). Light scattering from surface acoustic phonons in metals and semiconductors. *Solid State Communications*, *26*(8), 547–551.

Sharma, R. P., Bhadra, R., Rehn, L. E., Baldo, P. M., and Grimsditch, M. (1989). Crystalline to amorphous transformation in GaAs during Kr ion bombardment: A study of elastic behavior. *Journal of Applied Physics*, *66*(1), 152–155.

Smith, E., and Dent, G. (2013). *Modern Raman Spectroscopy: A Practical Approach*. Wiley.

Stoddart, P. R., Comins, J. D., and Every, A. G. (1995). Brillouin-scattering measurements of surface-acoustic-wave velocities in silicon at high temperatures. *Phys. Rev. B*, *51*(24), 17574–17578.

Teghil, R., Bonis, A. De, Galasso, A., Villani, P., and Santagata, A. (2007). Femtosecond pulsed laser ablation deposition of tantalum carbide. *Applied Surface Science*, *254*(4), 1220–1223.

Teghil, R., Bonis, A. De, Galasso, A., Villani, P., Santagata, A., Ferro, D., and Barinov, S. M. (2009). Nanostructured thin films obtained by ultra-short pulse laser deposition of vanadium carbide. *Applied Surface Science*, *255*(10), 5220–5223.

Teghil, R., D'Alessio, L., Bonis, A. De, Galasso, A., Villani, P., and Santagata, A. (2006). Femtosecond pulsed laser ablation and deposition of titanium carbide. *Thin Solid Films*, *515*(4), 1411–1418.

Thornton, J. A., Tabock, J., and Hoffman, D. W. (1979). Internal stresses in metallic films deposited by cylindrical magnetron sputtering. *Thin Solid Films*, *64*(1), 111–119.

Tiong, K. K., Amirtharaj, P. M., Pollak, F. H., and Aspnes, D. E. (1984). Effects of As+ ion implantation on the Raman spectra of GaAs: "'Spatial correlation'" interpretation. *Applied Physics Letters*, *44*(1), 122.

Toth, L. E. (1971). *Transition metal carbides and nitrides*. Academic Press.

Venables, J. D., Kahn, D., and Lye, R. G. (1968). Structure of the ordered compound V6C5. *Philosophical Magazine*, *18*(151), 177–192.

Wagner, J., and Fritzsche, C. R. (1988). Raman study of Si+-implanted GaAs. *Journal of Applied Physics*, *64*(2), 808–814.

Wang, Y., and Nastasi, M. (2010). *Handbook of Modern Ion Beam Materials Analysis*. Materials Research Society.

Wendler, E., and Wesch, W. (1993). Defect nucleation in weakly damaged ion implanted GaAs. *Nuclear Instruments and Methods in Physics Research Section B: Beam Interactions with Materials and Atoms*, *73*(4), 489–495.

Wesch, W., Wendler, E., Götz, G., & Kekelidse, N. P. (1989). Defect production during ion implantation of various AIIIBV semiconductors. *Journal of Applied Physics*, *65*(2), 519–526.

Williams, J. S. (1986). Materials modification with ion beams. *Reports on Progress in Physics*, *49*, 491–587.

Williams, J. S., and Austin, M. W. (1980a). Ion-beam-induced annealing effects in GaAs. *Nuclear Instruments and Methods*, *168*(1–3), 307–312.

Williams, J. S., and Austin, M. W. (1980b). Low-temperature epitaxial regrowth of ion-

implanted amorphous GaAs. *Applied Physics Letters*, *36*(12), 994.

Wittkowski, T., Distler, G., Jung, K., Hillebrands, B., and Comins, J. D. (2004). General methods for the determination of the stiffness tensor and mass density of thin films using brillouin light scattering: Study of tungsten carbide films. *Physical Review B*, *69*, 205401.

Wittkowski, T., Wiehn, V., Jorzick, J., Jung, K., and Hillebrands, B. (2000). Characterization of elastic properties of hard carbon and boron nitride films using the Brillouin light scattering technique. *Thin Solid Films*, *368*, 216–221.

Yasaka, M. (2010). X-ray thin-film measurement techniques. *The Rigaku Journal*, *26*(2), 1–9.

Zallen, R. (1992). Optical studies of nanocrystalline GaAs: a review. *Journal of Non-Crystalline Solids*, *141*, 227–232.

Zhang, X., Comins, J. D., Every, A. G., Stoddart, P. R., and Pang, W. (1998). Surface Brillouin scattering study of the surface excitations in amorphous silicon layers produced by ion bombardment, *Physycal Review B*, 58(20), 677–685.

Zhang, X., Comins, J. D., Every, a. G., and Stoddart, P. R. (1998). Surface Brillouin scattering studies on vanadium carbide. *International Journal of Refractory Metals and Hard Materials*, *16*(4–6), 303–308.

Zinin, P., Manghnani, M. H., Tkachev, S., Askarpour, V., Lefeuvre, O., and Every, A. (1999). Brillouin spectroscopy of surface modes in thin-film Si_3N_4 on GaAs. *Phys. Rev. B*, *60*(4), 2844–2850.